Title
STRUCTURE AND MECHANICAL PROPERTIES OF Fe-Ni-Co ALLOYS WITH AND WITHOUT CARBON

Author
Raghavan, Mathur Ramachandran Veera.

Publication Date
1972-03-01

STRUCTURE AND MECHANICAL PROPERTIES OF Fe-Ni-Co ALLOYS WITH AND WITHOUT CARBON

Mathur Ramachandran Veera Raghavan
(D. Eng. Thesis)

March 1972

AEC Contract No. 7405-eng-48

DISCLAIMER

STRUCTURE AND MECHANICAL PROPERTIES OF Fe-Ni-Co ALLOYS
WITH AND WITHOUT CARBON

Contents

STRUCTURE AND MECHANICAL PROPERTIES OF Fe-Ni-Co ALLOYS WITH AND WITHOUT CARBON

Mathur Ramachandran Veera Raghavan

Inorganic Materials Research Division, Lawrence Berkeley Laboratory and Department of Materials Science and Engineering, College of Engineering; University of California, Berkeley, California

ABSTRACT

In an endeavor to evaluate the effect of martensitic substructure and morphology on strength and fracture toughness, Fe-Ni-Co alloys with an without carbon were investigated. Optical and transmission electron microscopy techniques were used to document the structure while tension and fracture toughness testing were conducted to record the mechanical properties. The martensite in the two carbonless Fe-Ni-Co alloys, which differed in 4% Ni, had widely different substructures (lath and twinned) but their mechanical properties were closely alike. This indicated that the mechanical properties are not affected by the martensite morphology. Tempering treatments in Fe-Ni-Co-C steel having twinned martensitic plates caused preferential precipitation of carbides along the twins but the toughness showed no deterioration. The strength, however, increased rapidly on tempering.

Mode of deformation studies indicated that twinned martensite could deform by slipping and hence, transformation twinning is not a sufficient condition to cause the martensite to deform by twinning. It has been suggested that the mode of deformation rather than substructure of martensite is the important parameter governing the toughness of the steels.

I. INTRODUCTION

An important aspect of materials research is the problem of economic enhancement of strength and ductility of commercial structural steels. Many processes have been developed recently[1-3] but most of them involve mechanical treatments besides conventional heat treatment. It would be very attractive to develop high strength and high toughness by heat treatment alone. High strength is obtainable by simply increasing the carbon content of the steel,[4] but this seriously impared the ductility. The cause of the sharp decrease in ductility and toughness with increase in carbon content of the steel has been the topic of considerable debate in the past. This sharp change in mechanical properties had to be accompanied by an attendant change in the microstructure. The low carbon martensite (carbon less than 0.3%) consisted mainly of laths with a very high dislocation density. The striking change in the high carbon (carbon more than 0.4%) martensite was that the structure mainly consisted of plates rather than laths and many of the plates were internally twinned.[5-7] These transformation twins in martensite were due to the lack of slip at the temperatures of formation of the martensite and this topic has been elaborated by G. Thomas.[8,9] It was suggested by various workers that the Ms temperature of the steel could be a controlling factor governing the twinning.[10-12] Suggestions have also been made that the presence of twins seriously affects the fracture toughness.[5,13]

Moreover, on tempering the twinned martensite, the carbides preferentlly nucleated and grew along the twins. So two factors have been thought responsible for the inferior toughness properties of the high carbon steel as opposed to that of the low carbon steel, viz,

(a) twins per se.

(b) preferential precipitation of carbide along the twins.

The alloy systems investigated so far[14,15] were unable to confirm the adverse effects of the above mentioned factors, if any. The investigations conducted thus far have consisted of comparing the mechanical properties of two steels, one with low carbon and the other with higher carbon.

The purpose of the present investigation was to uniquely evaluate the effects of twins per se and twin boundary carbide precipitation on the mechanical properties. Two series of alloys are needed in order to accomplish this:

(a) Two carbonless alloys differing in martensite morphology.

(b) Two steels having the same carbon content but differing in martensite morphology.

Since nickel has been known to induce the martensite morphology change,[16] Fe-Ni system was chosen as the basis. The main problem encountered in this system was the inability to obtain 100% martensite at the high Ni content ($Ni \geq 30\%$). The recent investigations of Davies and McGee[17] showed that the effect of Co in Fe-Ni-Co ternary system was more than to increase the Ms temperature of the alloy. It was demonstrated that Co increased the Curie temperature (θc), and that $\theta c > Ms$ was a necessary condition for the formation of lenticular martensite. Thus, Co caused the morphology change of martensite in a Fe-Ni-Co ternary at a lower Ni content compared to a Fe-Ni binary. It was, thus, possible to obtain 100% lenticular martensite in Fe-Ni-Co alloys since they had relatively higher Ms temperatures.[17]

Four alloys were melted and the compositions are listed in Table 1. The carbonless alloys shall be referred to as T (twinned) and U (untwinned) whereas the carbon steels shall be termed TC (twinned with carbon) and UC (untwinned with carbon). The carbon content is limited to 0.1%C in order to avoid formation of any retained austenite. The alloy systems were chosen to unambigously determine the effect of twins per se (in the carbonless alloys) and the preferential carbide precipitation (in carbon steels) on the twins.

The effect of mode of deformation of martensite on mechanical properties has so far been largely neglected. Recent work by Davis and Magee[18] on mode of deformation showed that lenticular martensite deformed by twinning when the carbon content exceeded 0.3%, whereas the "packet" martensite did not deform by twinning even when the carbon content is as high as 0.55%C. This work, however, failed to correlate the effect of martensitic substructure with its mode of deformation. It was the intention of the present investigation to document the effect of the martensitic substructure on its mode of deformation since it was believed that mode of deformation rather than the martensitic substructure could be the controlling factor governing the mechanical properties.

II. EXPERIMENTAL PROCEDURE

A. Material Preparation and Heat Treatment

The steels used for this investigation were melted in a vacuum induction furnace and poured into copper molds in vacuum. The as-cast ingots were wrapped in stainless steel bags, packed with cast iron chips to prevent decarburization and homogenized at 1150°C for 72 hours. The ingots were then forged at 1200°C into 2 1/8 in. × 1 1/8 in. section bars. This size was close to the size of the fracture toughness specimen and hence minimized by material loss during machining.

Fracture toughness and tensile specimens were machined from the forged bars, homogenized in an argon atmosphere at 1200°C for one hour and then quenched into iced brine. They were immediately transferred to a liquid nitrogen dewar and stored there for about an hour to ensure complete transformation of austenite. The specimens were then tempered in a low temperature salt bath at 100, 200, 300, 400 and 500°C for 1 hour. One Specimen was retained in the as-quenched condition.

B. Optical Metallography

Specimens for optical metallography were cut from the heat treated fracture specimens, mounted in Koldmount, abraded on silicon carbide papers down to 600 grit, and polished on a 1μ diamond abrasive wheel. They were etched with 2% or 5% nital solution.

C. Transmission Electron Microscopy

The starting material were slices (.060 in.) cut from the bulk heat treated specimens. These slices were chemically thinned by a complex chemical agent[21] to about 0.004 in. Disks of the size of a standard Simens specimen holder (2.3 mm dia.) were punched and then polished in a twin-jet polishing apparatus. Electropolishing was done using a

chromic-acetic acid solution (75 gms CrO_3 + 400 ml acetic acid and 20 ml of distilled water). The voltage varied from 20-30 volts and the current varied from 12-18 m amps at 15°C. The thinned disks were eventually examined in a HU625 electron microscope operating at 650 kV. The high voltage microscope was found extremely useful in scanning in dark field since the diffraction pattern was considerably smaller than that at 100 kV. Besides, improved resolution was also obtained.

D. Mechanical Testing

1. Tensile Tests

Figure 1A shows the dimension of the tensile specimens used. Both the room temperature and liquid nitrogen tests were performed in an instron machine with a cross-head speed of 0.0423 in./sec (0.1 cm/min). The specimen surfaces were ground to remove any decarburised layer.

2. Fracture Toughness Tests

Plane strain fracture toughness values were obtained by testing standard compact tension.crackline loaded toughness specimen. Figure 2 illustrates the dimensions of the specimen. Pieces were cut from the forged bar, machined oversize, heat treated and then ground to final dimensions. The K calibration for this specimen geometry has been worked out by Srawley and Gross.[19] They expressed stress intensity as a function of specimen geometry and load and the solution was in the following form.

$$K = \frac{P}{BW^{1/2}} f\left(\frac{a}{w}\right)$$

where K = stress intensity

a = crack length

P = load

B = thickness of the specimen

W = width of the specimen

$F(\frac{a}{w})$ = a function dependent on $(\frac{a}{w})$ of the specimen

Thus, given the critical crack length and load at which the visible crack growth occurs, it should be possible to calculate the critical stress intensity K_{IC}.

Appendix I lists the computed values of $F(\frac{a}{w})$ for various values of $(\frac{a}{w})$, and Fig. 3 is a plot between

$$\frac{KBW^{1/2}}{P} \text{ and } (\frac{a}{w}) \quad .$$

The critical crack length at which instability occurs was obtained by using a Crack Opening Displacement (abbreviated as COD) gage attached to the specimen (Fig. 4). In order to be able to do this a prior calibration between the crack length and COD had to be established. This was done by machining crack length increasing in steps, and correspondingly measuring the COD for a predetermined load of 3000 lbs. The results are plotted in Fig. 5 and show the relation between two dimensionless parameters $\frac{EBv}{P}$ and $(\frac{a}{w})$ where v is the displacement (in inches) recorded by the COD gage.

A MTS machine (of 300 Kip Capacity) was used to fatigue precrack the fracture toughness specimens at a cycling rate of 6 cycles/sec. The cracks were fatigued to a minimum length of 0.050 in. requiring approximately 10,000 cycles for this growth. The fatigue crack growth was

observed through a low power optical microscope at the surface of the specimen. Maximum loads were kept high enough to provide reasonable fatigue crack growth rates and yet not so high that loading exceeded the recommendations in ASTM publications[19] which are:

$$\frac{K_{max}}{E} < \approx 0.0012 \text{ in.}^{1/2}$$

$$\left(\frac{K_{max}}{\sigma y}\right)^2 \leqslant \approx 0.02 \text{ in.}$$

$$K_{max} < \left(\frac{K_Q}{2}\right)$$

where K_{max} = the maximum stress intensity used during fatiguing

E = Young's modulus

σy = yield strength

K_Q = conditional stress intensity determined in the subsequent fracture test.

The precracking was invariably done at room temperature and the fracture toughness tests were conducted at liquid nitrogen temperature. The experimental set-up for liquid nitrogen fracture tests is shown in Fig. 6. During every fracture test, two plots were made. Load vs COD(v) and Load vs short stroke (displacement of the ram of the machine) were independently recorded on two X-Y recorders. The linearity of the COD gage was checked before every test to ensure the validity of the COD gage reading. The critical stress intensity values were calculated in accordance with the procedure outlined by the ASTM.[19]

3. Charpy Impact Tests

Charpy specimens were machined from the fracture toughness specimens after the fracture tests were over. Figure 1B illustrates the dimensions of a standard Charpy specimen. Two specimens were tested for each heat treatment and the average value was reported. A 120 ft-lb capacity impact machine was used to evaluate the impact properties.

E. Fractography

The fracture of every fracture toughness specimen was examined using a JEOLCO JSM-V3 scanning electron microscope (SEM). The fracture surfaces were covered with acetate tape and the fracture area extending from the tip of the machined notch to about 3/8 in. was sliced from the specimen so as to suit the specimen holder dimensions. The acetate tape was then stripped and the surface was repeatedly cleaned with acetone and then dried. The sliced fracture was then examined in the SEM operating at 25 kV.

F. Mode of Deformation Studies

In order to document the mode of deformation of the twinned martensite, a tensile specimen which was previously heat treated was used. The specimen was mechanically ground and chemically polished in a chromic-acetic acid solution at 20 volts and 15°C. The polished tensile specimen was deformed 5% at liquid nitrogen temperature and the structure was observed in an optical microscope under polarized light. This brought out the fine upheavals due to the slip traces in good contrast. The specimen was also observed under a scanning electron microscope at higher magnifications.

G. X-Ray Analysis

In order to ensure that complete transformation of austenite is martensite occurred when cooled to liquid nitrogen temperature, X-ray analyses were conducted on all the heat treated specimens. Specimen slices were cut from the heat treated fracture specimen and then scanned in a G.E. X-ray diffractometer using MoK_{α} radiation. A 3° slit was used to cover a larger area. The scanning was conducted from 30-40° in order to be able to detect the $(220)_{\gamma}$, $(211)_{\alpha}$, and $(311)_{\gamma}$ peak at the 2θ angles of 32.5°, 35.3° and 38.3° respectively, as suggested by Miller.[22] In all the cases the retained austenite content was too low to be detected by X-ray analyses. It was thus confirmed that retained austenite was absent or present in negligibly small amounts.

III. RESULTS AND DISCUSSION

A. Optical Metallography

Optical microscopy preceeded transmission electron microscopy work for all heat treatments. Specimens were cut from tested fracture toughness specimens. Extreme care was exercised in interpreting the optical micrographs because the systems under investigation were not very well documented. During tempering of martensite in carbon alloys the maximum tempering temperature was always limited by the As (start of austenite formation) temperature of the alloy. This demanded a very careful optical study of the tempered steels to ensure that tempering was done below the As temperature.

1. Carbonless Alloys

Figure 7 shows the optical micrographs of steel T and U. Steel T has the typical lenticular martensitic structure and steel U had the typical "massive" structure as described by Owen et al.[23] However, this massive martensite showed fine laths under the electron microscope. It was of interest to note that the twins in lenticular martensite were visible even in the light microscope. Figure 8 shows the enlarged image of the lenticular martensitic-plates which varied widely from 20μ to 1μ in width. Both X-ray and optical techniques showed no retained austenite. Both carbon and carbonless alloys had adequate hardenability to transform to martensite uniformly across the thickness of the fracture specimen during quench. This was expected due to the high Ni content, which increases the hardenability, though cobalt is shown to have the opposite effect.

2. Carbon Alloys

Optical studies of tempered steels TC and UC showed that the martensitic structure was retained to at least 500°C. Tempering was not obvious until 300°C in the optical micrographs. Carbide precipitation at the twin boundaries was not resolvable even at high magnifications. Figures 9-12 show the optical micrographs of steel TC and UC in tempered conditions. Both the steels retained the martensitic structure even when tempered at 500°C which undoubtedly indicated that A_s temperatures of the steels were above 500°C. Thus no austenite formed during the tempering treatments of the steels. This point was later confirmed by X-ray analyses and electron microscopy. The importance of this point shall be elaborated in a later section in the light of the tempering response of the steels on the mechanical properties. Besides the above mentioned details, any macro inhomogenieties (of composition) in the alloys could be detected due to variation in etching characteristics of optical specimens. The alloys investigated did not show any such characteristics.

B. Transmission Electron Microscopy

In order to correlate the fracture properties with the microstructure, careful transmission electron microscopy was conducted to characterize the microstructure. To avoid any ambiguity in establishing the correlation, thin foils were made directly from the fracture toughness specimens. This precaution was not always observed by earlier workers in this field, who made thin foils from heat treated thin sheets. This could lead to erroneous interpretations since the auto tempering effects present in quenched thick section will be absent in quenched thin sheets. Thus,

in order to be able to interpret the mechanical (especially fracture) properties, the thin foils for microstructure studies have to be made from the thick fracture toughness specimens.

1. Carbonless Alloys

The morphology and substructure of the carbonless alloys were documented and are shown in Fig. 13-15. In order to compare the fracture properties of lath and (twinned) plate martensite it was necessary to obtain representative structures. It is apparent that the alloy T was extensively twinned plates (Fig. 13), though presence of untwinned plates was also observed (Fig. 14). The structure can be best described as a mixture of twinned and untwinned plates, the former being dominant. In general, it was observed that the twins in the adjacent plates could not simultaneously be brought into contrast. This was essentially due to the fact that the plates were separated by either twin boundaries or high angle boundaries as opposed to small orientation changes between the adjacent laths.[6,14] Thus, for a given foil orientation, it may not be possible to image the twins in all the plates. This fact has to be kept in mind before quoting the extent of twinning in the structure. However, by adequate tilting of the thin foil it should be possible to bring the twins in each plate to contrast. Hence, the imaging of the twins was essentially limited by the amount of tilt allowed by the microscope. Figure 13C shows the diffraction pattern corresponding to the bright field image (Fig. 13A) and the indexing is shown in Fig. 13D. The dark field image of the twins is shown in Fig. 13B. In cases when the twinning plane was not normal to the foil surface (in other words, the twinning plane is not in diffraction condition), trace analysis was extremely

useful in evaluating the twinning planes. Trace analysis, though not unique, was a helpful tool in documenting other crystallographic features as indicated later. The alloy U has the typical lath morphology as described by earlier workers.[5,6,14] Figure 15 shows the bright image of lath martensite.

2. Carbon Steels

Transmission electron microscopy was conducted on specimens tempered at five different tempering temperatures besides the as-quenched structure. Slices were cut from the tested fracture specimens, chemically thinned and subsequently electropolished in a twin jet polisher. Since the purpose of investigating these carbon steels was to establish the effects of carbide precipitation at the twin boundaries on the mechanical properties, special attention was directed towards the preferential percipitation of carbides. It has been pointed out by G. Thomas[13,24] that dark field studies rather than bright field are unique in identifying and demonstrating any precipitation. Hence extensive tilting and scanning in the dark field was performed in order to uambiguously image the preferential precipitation of carbides. Carbide spots in general were very weak compared to the matrix spots and hence could not be visually observed on the imaging screen, except at high tempering temperatures. So, scanning in the dark field was done by moving the objective aperture over the entire diffraction pattern and observing the dark field images until the carbides reversed contrast. Once the carbide spot was located, the beam tilting device was used to obtain high resolution dark field. As already mentioned, the Hitachi 625 kV microscope operating at 650 kV was found very suitable for this purpose due to the small diffraction pattern.

The as-quenched structures of steel TC and UC were twinned and untwinned martensites respectively. The as-quenched lath morophology of steel UC as shown in Fig. 16. Besides the morphology and substructure of the as-quenched martensite of steels TC and UC the main point of interest was the absence of any auto-tempering in either structure. Absence of auto-tempering was confirmed by extensive tilting and dark field scanning. This was to be expected since the Ms temperatures of steels TC and UC are very low. No Ms measurements were made on these steels but by extrapolating Davies and McGee's work[17] on Fe-Ni-Co ternary alloys, the estimated Ms temperatures are about 80°C for steel TC and about 220°C for steel UC. The absence of any auto-tempering enabled the comparison of the as-quenched properties of steels TC and UC.

It was, thus, possible to obtain 0.1% carbon steels TC and UC having mostly twinned and mostly dislocated lath martensitic structures respectively. The structures of carbonless alloys T and the carbon steel TC were very similar. Steel UC consisted of a mixture of plates and laths as opposed to fine lath martensite of carbonless alloy U. However, it was convincingly shown that the carbon steels TC and UC had entirely different morphologies, as already mentioned. Steels TC and UC are hence concluded eligible to represent the morphologies of high and low carbon martensites <u>but each having only 0.1% carbon</u>.

Tempering at 100°C for 1 hour did not cause any precipitation in either steels. Previous work on Fe-29% Ni-0.1%C[25] showed that ε-carbide formed

on tempering this steel at 100°C for longer aging times. Tilting both in bright and dark field did not reveal any precipitation. However, the absence of any precipitation does not preclude the possibility of carbon atoms segregating at lattice imperfections such as twin boundaries, dislocations, jogs, lath boundaries, etc. Though there was no way of uniquily proving such segregation of the carbon atoms from microstructural investigations, it could cause an observable change in the tensile properties due to the partial depletion of carbon atoms from the matrix. Hence, any change in tensile properties without an attendant change in the microstructure should not be considered anamolous. This point shall be referred to while discussing the mechanical properties of the steels.

Tempering at 200°C for an hour resulted in extensive precipitation in both the steels. In steel TC the precipitation occurred both in the matrix and at the twin boundaries. Figure 17 is the bright field image showing discontinuous nucleation of carbides at the twin boundaries. The twins are not in contrast but the traces are faintly visible and are indicated by an arrow. Figure 18A is the bright field image showing the twins and precipitation of carbide at the twins. The dark field image of the twins (Fig. 18B) and the carbides (Fig. 18C) along the twins were obtained by imaging the twin and carbide spots respectively. Thus, the precipitation of carbides at the twin boundaries was uniquely demonstrated by dark field imaging. Due to the lack of enough carbide diffraction spots, the carbides could not be uniquely identified. However, by trace analysis the carbides precipitated in the matrix were identified as cementine since it is known that comentite precipitates on the {110} plane of martensite while ε-carbide forms on the {100} cube planes. The

structure of steel UC tempered at 200°C is shown in Fig. 19. The carbides are identified as a mixture of ε-carbide and cementite. The ε-carbides besides forming on the {100} planes are also wavy. The ε-carbides are indicated by arrows in the structure.

Tempering at 300°C caused additional precipitation along the twins. The carbides were long and formed almost continuously along the twins. In the absence of any twinning in the plate or in the untwinned regions of the plate, precipitation was of the typical Widmanstatten type. The carbides formed after 300°C tempering were found larger in dimension compared to those formed at 200°C tempering. The main problem often encountered was to establish the type of carbide precipitation, i.e., whether the carbide had formed on the twin or not. As mentioned earlier, it was not always possible to tilt the foil to bring the twin in contrast. Nevertheless, the carbides could be in contrast. In such cases careful trace analysis was done to show that the carbides did form on one of the {112} variants and not on the {110} planes. In order to accomplish this, the foil was always tilted to such an orientation to minimize any ambiguity (a low index orientation was always preferred to work with). For example, <113> orientation was found advantageous compared to a <133> orientation since in the former case the {110} and {112} poles are widely separated, thus making the trace analysis less ambiguous. Figure 20A shows the bright field image of carbide precipitation on the twins. The twins were not in contrast and hence it seemed uncertain whether the carbide formed on the twin boundaries or in the matrix. Trace analysis uniquely identified the carbide trace to belong to $(21\bar{1})$ plane. Figure 20B

shows another bright field image indicating the changing carbide morphology in the twinned and untwinned regions of the martensitic plate. Careful investigation also revealed that plate boundary carbide precipitation occurred as shown in the dark field image in Fig. 21.

Steel UC essentially consisted of Widmanstatten comentite precipitates, as shown in Fig. 22. There were also indications of lath-boundary carbide precipitation. Figure 23B shows a dark field micrograph showing reversal of contrast of lath-boundary carbides but the bright field image (Fig. 23A) did not reveal the carbide precipitation. The precipitation was less extensive compared to the recent work on Fe-Mo-C steels.[26] Since it was speculated that the lath boundary carbides could be detrmintal to the mechanical properties of the steels,[15,26] extreme care was taken in documenting the structure. Besides, the fracture toughness of the steel UC tempered at 300°C was found to be low.

Tempering at 400°C and 500°C of steel TC showed identical carbide morphologies as shown in Figs. 24 and 27. The carbides formed "quasi-continuously" along the twin boundaries. Moreover, the extent of matrix precipitation was less predominant compared to the lower tempering temperature. Figure 26 shows the bright and dark field image of carbides forming along the twins. Again, trace analysis was used to establish the twin boundary precipitation of carbides. These carbides formed effective barriers to slip resulting in appreciable changes in the mechanical properties of the steel. Figure 26A shows the bright field image of steel TC tempered at 400°C demonstrating extensive precipitation along the twin boundaries while Fig. 26B shows the reversal of contrast of the carbides. Steel UC, when tempered at 400°C, resulted in partially

spherodised carbide precipitates in the plates and laths. Figures 25A and B demonstrate the matrix precipitation in the steel UC while Figs. 26A and B indicate the increasing carbide precipitation along the lath and plate boundaries.

Tempering of steel TC at 500°C showed that carbides preferentially formed along the twin boundaries and the precipitation was almost continuous along the twins. Figures 27A and B represent the bright and dark field images of the carbide precipitation on the twins. Thus, it was shown that with increasing tempering temperatures, the carbides preferentially formed grew along the twins in steel TC, and in steel UC it resulted in increasing lath boundary precipitation and partial spherodisation of the carbides.

C. Tensile Properties

As already mentioned, flat tensile specimens were used to test the tensile properties. The values of yield strength (σ_y), ultimate strength (σ_u), and elongation were measured by conventional methods. The values of strain-hardening coefficient, n, and true strain at fracture, ε_f, were determined from the following equations:

$$\varepsilon_f = \ln (1 + e_f)$$

$$n = \varepsilon_u = \ln (1 + e_u)$$

where ε_u = true ultimate strain

e_u = engineering ultimate strain

Prior to each tensile test, the specimen was scanned in an X-ray diffractometer to ensure absence of retained austenite.

1. Carbonless Alloys

The tensile properties of steels T and U are listed in Tables II and III. It was apparent that the strength of twinned martensite was comparable to that of the untwinned martensite. Earlier work on Fe-Ni binary alloys by Speich and Swann[27] indicated that the morphology of martensite did not significantly affect its strength. Based on a dislocation model Kelly and Pollard[28] suggested that the slip dislocation had to assume a "zig-zag" configuration due to the presence of the internal twins and that the most favorable conditions for slip occurred when the two dislocation components shared the same slip plane. Their results predicted that the internally twinned martensite should be stronger than untwinned lath martensite by a factor in the region of 1.05 to 1.20. However, the experimental results showed that the factor varies between 1.08 and 1.30. Though the theory predicted that the twinned martensite be stronger than untwinned martensite, in practice it was impossible to isolate the effect of substructure alone. Besides the martensitic substructure, the austenitic grain size,[29] the lath or plate size and the lath or plate size distribution contribute to the strength of the steel. It was found difficult to evaluate these effects individually. In spite of the fact that both the steels T and U were identically processed prior to testing, the austenitic grain sizes were found to be slightly different. Thus, the difference in strength of about 5 Ksi between the alloys T and U could be due to a cumulative effect of above mentioned factors. It was, hence, concluded that the strengths of twinned and untwinned martensite did not differ appreciably.

It was observed that the strain hardening coefficient of twinned

martensite was higher than that of untwinned martensite. Sleeswyk and Verbraak[30] proposed a dislocation mechanism for the passage of dislocation through the twins. The mechanism involved the dissociation of $\frac{a}{2}[\bar{1}\bar{1}1]_M$ matrix dislocation into a $\frac{a}{6}[11\bar{5}]_T$ dislocation in the twin. The $\frac{a}{6}[11\bar{5}]_T$ dislocation then dissociated into a $\frac{a}{2}[11\bar{1}]_T$ slip dislocation in the twins. Thus the passage of dislocations through the martensitic twins resulted in a series of dislocation interactions which ultimately caused the steel to work harden more. This part, however, has not yet been pointed out by earlier workers.

2. Carbon Steels

The variation of yield and tensile strengths of steels TC and UC are indicated in Figs. 28-31. Figure 28 shows the variation of the tensile properties of steel TC with the tempering temperature. The yield strength showed an initial dip, followed by a gradual increase up to 500°C tempering. The tensile strength showed a similar variation. The strengths reached a minimum when tempered at 100-200°C and then increased at higher tempering temperature. The % elongation dropped on tempering at 100°C and then remained fairly constant. This behavior, at the outset, seemed anamolous compared to the conventional tempering response of steels where the strength progressively decreased with increasing tempering temperature. The response of low carbon steels to tempering was investigated by Winchell and Cohen[4] and Chilton and Kelly.[16] The authors pointed out that carbon could be, in certain cases, a more effective strengthener as precipitates (carbides) than as solute in solution.

The initial decrease in strength could be due to segregation of carbon atoms at the twin boundaries prior to carbide precipitation, which

caused partial depletion of carbon from the matrix. With increasing tempering temperatures, the carbides formed more continuously along the twin boundaries. Thus, the dislocations encountered sheets of carbides as they moved across the martensitic plate. The dislocation cannot pass through the carbides as they did through the twins by a dissociation mechanism. Thus, there was a definite strengthening effect due to the carbide precipitation. The room temperature tensile properties of steel TC plotted in Fig. 28 showed a similar variation as the -196°C tests. However, the increase in strength due to tempering is rapid at -196PC compared to the 25°C tests.

An earlier study by Mihilasin[31] on Fe-Ni-Co alloys pointed out that a positive strengthening was observed when those alloys were aged at 450°C for 72 hours. The increase in strength was due to fine precipitation of austenite during aging. In order to ensure that the observed increase in strength in the present investigation was not due to any austenite precipitation but due to the carbide precipitation, specimens after the tempering treatments were subjected to X-ray analysis. No austenite was detected in any of the tempered specimens.

The tensile properties of steel UC are plotted in Fig. 29. The strength at -196°C showed a small decrease on tempering at 100°C followed by an increase up to 400°C tempering. From the tensile properties at -196°C and 25°C, it was apparent that steel UC also showed a strong dependence of flow stress with temperature as steel TC. Thus, in both the steels, the flow stress increased rapidly at -196°C compared to

the increase at the room temperature. It can hence be inferred that this flow stress dependence was not due to the substructural differences since it was observed both in steels TC and UC. The tensile properties of steels TC and UC are compiled in Figs. 30 and 31. These plots indicated that the trend of the strength properties of steels TC and UC were identical, and hence the tempering response of the steel was independent of its martensitic substructure. In these low carbon steels, carbon was an effective strengthener as carbides rather than as solute in solution. In the high carbon steels, the initial strength of the martensite is very high and overrides the "precipitation hardening" effect due to carbides on tempering.

D. Fracture Properties

Tests were conducted to evaluate the plane strain fracture toughness value, K_{IC}, for each heat treatment. A few Charpy tests were conducted at the room temperature, though the results have been interpreted on the basis of the fracture toughness measurements. The primary advantage of measuring fracture toughness over Charpy impact behavior is that the plane strain fracture toughness, K_{IC}, is a material property while the Charpy impact value gives only a relative indication of toughness under extreme loading conditions. Thus, it should be possible to correlate K_{IC} and the microstructural features.

The strength levels of the low carbon martensites are low and are of the order of 150-180 Ksi at room temperature. Hence, in order to obtain valid plane strain fracture toughness values, it was necessary to resort to thick specimens. The empirical design criterion regarding thickness of the fracture toughness specimen is:

$$B \geq 2.5 \left(\frac{K_{IC}}{\sigma_y}\right)^2$$

where B = thickness of the specimen in inches

K_{IC} = fracture toughness, (Ksi $\sqrt{in}$)

and σ_y = yield strength (Ksi).

Due to limitation of material and other accessories, 1 in. thick ASTM standard[19] fracture toughness was chosen and tests were conducted at -196°C to ensure plane strain conditions. At the liquid nitrogen temperature the yield strength of the steel increases while the fracture toughness value decreases. Thus the fore-mentioned thickness criteria was more readily satisfied. Before experimental tests were begun, this specimen size was checked for through-thickness hardenability to martensite by using optical metallography, microhardness measurements and X-ray analysis (to detect any retained austenite).

During heat treatment, the initial quench was done in iced brine and then after about 15 secs, the specimen was transferred to liquid nitrogen. The specimen was checked for any cracks which could have resulted due to thermal stresses during the rapid quench of 1 in. thick section. Presence of cracks rendered the specimen invalid for fracture toughness testing.

1. Carbonless Alloys

Table II lists the mechanical properties of alloys T and U. Four fracture toughness tests were conducted at -196°C of alloys T and U, but no valid plane strain conditions were obtained. The P vs v curve is shown in Fig. 32A. The curve showed extensive slow crack growth and no

instability. The critical value of stress intensity calculated by constructing the secant line was found to be an apparent value and not plane strain fracture toughness value. The values did not satisfy either the thickness criterion or the deviation from linearity criterion. These criteria are enumerated in a later section. The apparent values (K_Q) were not indicative of the fracture toughness because they do not represent the stress intensity at which instability occurs. They simply indicate the stress intensity at which plastic flow initiates at the crack tip. Thus, the apparent value, K_Q, was not useful in interpreting toughness. The apparent values obtained for alloys T and U indicated that both the alloys were very tough and that specimens of larger dimensions had to be used to evaluate the plane strain values. Since the K_Q values do not indicate the absolute fracture toughness of the alloys Charpy tests were conducted at -196°C in order to evaluate the resistance of the alloy to impact. An 11 ft-lb difference was observed between alloys T and U. This difference of 11 ft-lbs could not be attributed only to the substructural variation since it could be due to other differences between the alloys as grain size, and the difference in Nickel contents.

Fractographic analyses, which shall be described later, indicated no embrittlement in the alloys T and U. On the contrary, the fractographs showed complete dimpled rupture. This called for the conclusion that the twins in the martensitic structure were not detrimental to the toughness of the steels.

2. Carbon Steels

The fracture toughness values of specimens of steels TC and UC are given in Tables V and VII. Line drawings showing the variation of K_{IC} vs tempering temperature are shown in Figs. 33. Valid plane strain fracture toughness values were obtained for all tempering treatments. These values obtained are apparent toughness values (K_Q) and are quoted as valid K_{IC} values because of two reasons: 1) The specimen thickness for each specimen was greater than $2.5\left(\frac{K_{IC}}{\sigma_y}\right)^2$ and 2) the deviation from linearity of the load (P) vs crack-opening displacement (v) curve was greater than that recommended in ASTM publications.[19]

The typical load (P), crack opening displacement (v) curve is shown in Fig. 32B. A definite slow crack growth was observed in almost all cases followed by a "pop-in". The secant line had to be drawn due to the slow crack and its intersection with the P vs v curve taken as the critical load.

A glance at the variation of K_{IC} of steel TC revealed two important features: a) The K_{IC} increased gradually with tempering temperature until 200°C. b) A drop in K_{IC} at 300°C followed by an increase on subsequent tempering. Steel UC, on the contrary, showed an increase in K_{IC} on tempering at 100°C followed by a decrease when tempered at 200°C and 300°C and then an increase when tempered at 400°C. The interpretation of these results shall be discussed in the light of the microstructural features in a later chapter.

Figure 34 shows the yield strength vs fracture toughness values for steels TC and UC and are marked "twinned" and "untwinned" regions respectively. It is apparent that for a given yield strength steel TC had

better toughness than steel UC. Though this increased toughness of steel TC over steel UC was not very appreciable, it definitely proved the steel TC was not embrittled by the preferential twin-boundary carbide precipitation. Thus, the twin-boundary carbide precipitation was shown to have no detrimental effect on the toughness of steel TC.

Figures 35 and 36 show the variation of fracture toughness and % Elongation with tempering. These plots shall be referred to in a later chapter in order to establish that fracture toughness was a more structure sensitive parameter compared to % elongation and that the later was not indicative of the toughness of the steel. It shall be shown that the tensile properties cannot predict the fracture toughness value which was obtained only from a fracture test. The classical notion that the % Elongation represented the toughness of the steel shall be rebutted and the importance of fracture toughness value as a true toughness parameter shall be emphasised.

E. Fractography

The fracture morphology of each fracture toughness specimen was thoroughly documented by means of optical macrophotography and scanning fractography. The optical macrophotographs were useful in evaluating the type of fracture (plane strain or plain stress) and the fatigue crack length of the fractured toughness specimens. They also clearly indicated the presence of quench cracks formed during the quench of the fracture specimens. Every specimen had to be checked for the presence of quench cracks since the subsequently formed fatigue cracks should be longer than the quench cracks. The specimens for optical macrofractography were marked for rapid identification.

1. Carbonless Alloys

The fracture surfaces of alloys T and U are shown in Fig. 37. The mode of failure was not plane strain as seen from the large shear lips. The scanning fractographs of (the fracture toughness specimens of steel T and U are shown in Fig. 38 and they indicated clearly that ductile crack propagation was the only mode of failure. No indications of cleavage were observed. The dimple sizes also appeared similar though no stereo pictures were taken to obtain the exact dimple size.

Since the fracture toughness specimens did not yield valid plane strain tests, Charpy impact tests were conducted at liquid nitrogen temperature. The fractographs of the Charpy specimens are shown in Fig. 39. The fracture morphology of the Charpy specimens was identical to that of the fracture toughness specimens. No trace of embrittlement was detected in alloy T or U. Thus the substructure of martensite did not seem to affect the fracture mode.

2. Carbon Steels

The optical macrographographs of steels TC and UC are shown in Figs. 40 and 41. It was noted that all specimens exhibited small shear lips. The portion of flat fracture was indicative of the extent of plane strain fracture that the specimen underwent. The ASTM standards[19] require that the percentage of shear lip be quoted along with the K_{IC} value. The results are tabulated in Tables V and VII. The quench cracks were distinctly visible as dark (oxidized) areas at the notch tip. They were smaller than the subsequent fatigue cracks and hence caused no problems. No other information regarding the fracture mode was obtained from this optical study and scanning electron

microscopy was resorted to in order to obtain details regarding fracture morphology.

Four modes of fracture were generally observed in all the steels. They are (a) cleavage, (b) ductile (dimpled) rupture, (c) quasi-cleavage, and (d) intergranular failures. These types of failures are enumerated by Beachem and Pelloux[32] and ASTM publications.[33] All the specimens showed a mixture of these modes but their relative proportions varied depending on the heat treatment.

The as-quenched specimen of steel TC shows grain boundary separation, regions of quasi-cleavage and dimpled rupture (Fig. 42). The point of interest was the appearance of quench crack at the notch tip of the specimen. These cracks can be readily detected in the microscope since they can be easily distinguished from the fatigue cracks. The quenched cracks have black, oxidized surface since these cracks form above room temperature as opposed to the fresh surface of the fatigue cracks. Figure 43 shows the scanning electron fractograph of the notch tip and the two types of cracks were easily distinguishable. The quench cracks were usually small and they did not pose any problems since the fatigue cracks were longer than the quench cracks.

Steel TC tempered at 100°C showed a mixture of quasi-cleavage and dimpled rupture as shown in Fig. 44. Tempering at 200°C showed a similar mode of failure and at 300°C the fracture mode showed increasing proportions of quasi-cleavage (Figs. 45 and 46). Thus, a gradual variation of fracture mode occurred during tempering. Tempering at 400°C and 500°C caused the steel to fail predominantly by ductile mode as shown in Figs. 47 and 48. Thus, the variation in fracture topography

followed the K_{IC} variation with tempering.

Steel UC exhibited a mixture of cleavage and dimpled rupture in the as-quenched condition (Fig. 49). The proportion of dimpled rupture was less than that of steel TC. On tempering the steel at 100°C, no significant difference in fracture morphology was observed. The structure consisted of a mixture of cleavage facets, grain boundary separation and a small proportion of dimpled rupture as indicated in Fig. 50. The specimen tempered at 200°C showed a mixture of quasi-cleavage and fine dimpled rupture (Fig. 51). Isolated examples of cleavage was also observed. At 300°C tempering the steel showed the same fracture modes. Quasi-cleavage and cleavage were again the predominant modes as shown in Fig. 52. Very little dimpled rupture was observed in specimens tempered at 200°C and 300°C. The toughness increases when the steel was tempered at 400°C and a corresponding change in fracture mode was observed. Quasi-cleavage and dimpled rupture predominated the fracture morphology as indicated in Fig. 53. Thus, it was apparent that both steels TC and UC showed a one-to-one correspondence between the fracture toughness and fracture mode.

F. Mode of Deformation

The mode of deformation of twinned martensite was observed both under optical and scanning electron microscopes. For optical metallography, polarized light was used in order to image the fine upheavals. The polarizer was fixed and polarized the beam of light incident on the specimen. The reflected beam from the specimen was again polarized by the analyzer which was adjustable about the optic axis. The analyzer was adjusted so as to

obtain a good contrast of the details. Figures 54-56 show a series of optical micrographs showing the structures of steel TC in the undeformed state, after 5% tensile deformation at -196°C and after subsequent polishing. The micrographs were of the same area in the tensile specimen. Figure 54 shows the martensitic plates in steel TC quenched to liquid nitrogen temperature. The martensitic plate boundaries and mid-ribs could be clearly seen in the micrograph. The twins in these plates were, however, not revealed. Figure 55 shows the structure of the same area after 5% deformation at liquid nitrogen temperature. Wavy slip traces were visible inside the plates and were observable in all the martensitic plates. When the deformed specimen was electropolished for about one minute, the same area showed no slip traces as shown in Fig. 56 The deformed specimen was also observed under the scanning electron microscope. Figures 57 and 58 show the scanning electron micrographs of the deformed specimen.

The results obtained during this investigation unambiguously correlated the martensite substructure and its mode of deformation. The martensite of TC was shown to consist of twinned plates (refer to Fig. 8) and some laths. As already suggested by Thomas,[9] the twinned plates formed at lower temperatures where the critical resolved shear stress (CRSS) for twinning was less than that required for slipping. Since the martensitic plates of steel TC were extensively twinned on quenching to liquid nitrogen temperature, the CRSS for twinning was lower than that for slipping at the liquid nitrogen temperature. In order to evaluate the deformation mode of twinned martensite, deformation was performed at the liquid nitrogen temperature. This assured that the martensite

was deformed at a temperature at which it formed by twinning, thus eliminating any ambiguity in the correlation.

The optical metallography results showed presence of wavy traces in each martensite plate. The traces, however, disappeared on subsequent polishing, thus confirming that they were slip traces and not deformation twins. This is due to the fact that the surface relief caused by slip steps are removed during polishing whereas the deformation twins, that caused an orientation change, persists even after polishing. The results, hence, indicated that the deformation mode of martensite was independent of its substructure. Thus a twinned martensite need not necessarily deform by twinning. Davies and Mcgee[18] have shown that the deformation mode of lenticular martensite changes from slipping to twinning when the carbon content exceeds 0.3%. On the contrary, even 0.5%C did not induce the transformation in lath martensite. The authors, however, did not indicate how martensite could retain its lath morpology when the carbon content is as high as 0.5%. They also did not draw any correspondence between the substructure and deformation mode of martensite. The present investigation firmly indicated that twinned substructure was not a sufficient condition to induce deformation twins in martensite. It was pointed out by Davies and Mcgee[18] that deformation twinning could be more easily induced in the tetragonal lenticular martensites than in the cubic packet martensites. They contend that the preferential occupancy of the carbon atoms in certain octahedral sites in the tetragonal martensite promoted deformation by twinning. However, as already mentioned, the authors observed that a threshold carbon content of 0.3% was required to induce deformation twinning in the lenticular

martensites. From Richman's work,[34] carbon seems to have a direct effect on the mode of deformation of martensite. It, hence, seemed that substructure of martensite did not play a decisive role in governing its deformation mode. Based on the earlier work[18,33] it could only be suggested that the alloying elements (carbon in particular) control the mode of deformation of martensite, and that the substructure plays only a secondary role.

IV. CORRELATION OF FRACTURE TOUGHNESS AND TENSILE PROPERTIES

Prior to the development of fracture mechanics, it was believed that high toughness can be identified by either good elongation or reduction in area. With the advent of fracture mechanics and availability of K_{IC} data for various commercial steels the recent trend is to try to correlate the parameters of a tensile test (yield strength, ultimate strength, strain hardening coefficient, etc.) with the fracture toughness value, K_{IC}. It would be very attractive if it were possible to compute the K_{IC} from the data obtained in a tension test. This is desirable because of the large size of the fracture toughness specimen and the tedious testing procedure involved in conducting a fracture test. Besides, it would also enable evaluation of fracture toughness values of low strength materials where valid plane strain conditions are attained only in very thick specimens.

Hahn and Rosenfield[48] developed a ductile fracture model which tries to correlate quantitatively the fracture toughness and the tensile properties. They arrived at a relationship involving the uniaxial yield strength σ_y, true strain at fracture ε_f, Young's modulus E and the strain hardening coefficient n,

$$K_{IC} = \left[\frac{2}{3} E \varepsilon_f n^2 \sigma_y\right]^{1/2}$$

where K_{IC} is the plane strain fracture toughness. The authors obtained reasonable agreement between the calculated K_{IC} values based on some commercial titanium alloys, steel and aluminum alloys. Tables III and V list the calculated values of K_{IC} based on the tensile parameters for steels TC and UC. A glance at Tables III, V, and VI clearly indicates

neither the Hahn-Rosenfield model nor the % Elongation to fracture are good measures of the fracture toughness of these steels. Ductility is also not readily related to fracture toughness. Jones and Brown[49] and Brown and Srawley[19] made similar observations and it was concluded that K_{IC} is not proportional to ductility. Thus ductility cannot be regarded as a direct measure of toughness. Though some workers have tried to explain the discrepancy between the calculated and measured K_{IC} values on the basis of the micromechanisms of fracture, no such trend was observed. This is to be expected because the tensile properties are less sensitive to microstructure than the toughness. Hence, fracture toughness seems to be a unique material property and is in no apparent way related to the uniaxial tensile properties. At present it can be evaluated only by a fracture toughness test.

V. MICROSTRUCTURE-FRACTURE TOUGHNESS CORRELATION

The concepts of fracture mechanics have been widely accepted only during the past few years and since the plane strain fracture toughness value has been shown to be indicative to the toughness of a steel, a one-to-one correspondence between the fracture toughness values and the microstructure should be possible. In order to be able to accomplish this, extreme care was observed both in fracture toughness testing and transmission electron microscopy. Extensive tilting and dark field technqiues were used to unambiguously document the morphology and substructure of quenched and tempered martensites.

A. Carbonless Alloys

Valid plane strain fracture toughness tests were not obtained for alloys T and U. Both of these alloys exhibited ductile failure and no embrittlement was observed. The only qualitative conclusion that could be arrived at from these tests is that the substructural differences between alloys T and U do not affect their failure mode.

B. Carbon Steels

Fracture toughness tests results on steels UC and TC showed that the toughness increased with tempering temperature. Though the absolute K_{IC} values of these steels were different, the trends of K_{IC} values with tempering temperature were similar. The curves showed an initial increase, a dip when the tempered at 200-300°C, followed by increasing K_{IC} values when tempered above 300°C. The embrittlement occurred in the 200-300°C range for steel UC whereas it occurred only at 300°C for steel TC. Many investigations have been conducted on this embrittlement phenomenon especially in high strength steels.[35-44] Though no consensus has

been reached, some factors have been found to be responsible for this embrittlement. Banerjee[45,46] has indicated that the change of carbide precipitation from ε-carbide to cementite could result in inferior toughness. Some workers speculated that the impurity elements could play a decisive role in the embrittlement while others pointed out that the precipitation at the martensite lath boundaries could be important in causing the embrittlement. It was not possible to isolate the effects of the factors mentioned above (especially when the factors coexist). For instance, in steel UC the embrittlement in the 200°C tempering range could be due to the precipitation of ε-carbide (Fig. 19) as suggested by Banerjee and at 300°C the precipitation of carbides at the lath boundaries (Fig. 23) could be deleterious. Tempering steel UC at 100°C caused no observable precipitation and the toughness increased. The first drop in toughness occurred at 200°C tempering as the structure consists of a mixture of ε-carbide and cementite followed by lath boundary carbide precipitation at 300°C. Thus, it was speculated that the low toughness of steel UC when tempered at 200-300°C is due to the presence of ε-carbide and lath boundary precipitation of carbides. Tempering at 400°C resulted in partially spherodized carbides and these were apparently not detrimental to the toughness which increased to a K_{IC} value of 71 Ksi $\sqrt{in}$.

The tempering behavior of steel TC differed from that of steel UC in that the toughness drop occurred only at 300°C tempering. Careful microstructural investigation revealed presence of plate boundary precipitation at 300°C tempering. Precipitation of carbides along twin boundaries was first observed after 200°C tempering but plate boundary

precipitation was detected only at 300°C (Fig. 23B). Thus, it seemed that the initiation of precipitation of carbides at the martensite plate or lath boundaries caused a drop in toughness. However, spherodization of the carbides at these boundaries was harmless. The substructural and morphological differences between steels TC and UC did not seem to contribute to the toughness of the steels as expected. On the contrary, precipitation of carbides along the twin boundaries acted as barriers to slip and enhanced the strength of steel TC when tempered above 400°C. The toughness of the steel showed an attendant increase.

Having shown that the substructure of martensite did not cause adverse effects on the toughness of the steel, the reason for the low toughness of the high carbon steels still remains to be seen. Though positive proof was not available, the following factors could be deleterious to the toughness: a) micro-cracking in acicular martensites as observed by Marder and Benscoter[47] and b) mode of deformation of martensite. Microcracking across the martensitic plates have been observed in carbon steels where carbon content exceeds 0.6%. No microcracking has so far been observed in 0.4%C martensities. However, previous investigations have shown that even 0.4%C steels exhibit poor toughness.[14,15] Thus, it seemed unlikely that microcracking causes the inferior toughness of the high carbon steels. It is believed that the mode of deformation of martensite is the prime factor in deciding the toughness of the steel. Richman[34] pointed out that 0.4%C martensite deforms by twinning. Nevertheless, deformation mode of tempered martensites has not been investigated and no correlation has yet been drawn between the mode of deformation and fracture toughness. Huang and

Thomas[15] observed that manganese increased the extent of twinning in the martensites and also impared the toughness of the high manganese steels. It could be pointed out that manganese, besides increasing the propensity to twinning of martensite, could also change the deformation mode of the martensite. It is needless to reiterate that no relationship exists between the formation of transformation and deformation twins, though a twinned substructure was shown[18] to be a necessary (but not sufficient) condition to induce deformation twins in martensite. It thus seems that the correlation among substructure, mode of deformation and fracture toughness is very important and should be paid more attention in order to unambiguously interpret the mechanical behavior of the steels.

VI. CONCLUSIONS

1. Twins per se did not have any effect on the toughness of the steels.
2. The twins in the martensite increased the work hardening rate.
3. The precipitation of carbides in the twin boundaries during tempering in steels TC did not cause any detrimental effect on the toughness. On the contrary, a positive strengthening with an attendent increase in the toughness was observed as the carbides formed along the twins.
4. Initiation of precipitation at the martensitic lath and plate boundaries during tempering caused an observable decrease in the toughness values of the steels. A mixed precipitation mode in the matrix (cementite and ε-carbide) was also found detrimental to the toughness.
5. The precipitation of carbides in the twinned martensite occurred discontinuously along the twins and in the matrix at low tempering temperatures (below 200°C). At higher tempering temperatures the precipitation was predominantly on the twin-matrix interfaces. In the untwinned martensite, precipitation occurred in the matrix below 200°C and on tempering above 300°C both lath boundary and matrix precipitation were observed.
6. In the low carbon Fe-Ni-Co-C steels investigated, carbon was a more effective strengthener as carbides than as solute in solution.
7. The strong temperature dependence of flow stress in the carbon steels was found to be independent of the substructure of martensite.

8. The mechanical properties of twinned martensitic steel were found somewhat superior to those of the lath martensitic steel.
9. The mode of deformation was independent of the martensitic substructure. Thus, a twinned martensite need not necessarily deform by twinning. Twinned substructure is a necessary but not sufficient condition to cause the steel to deform by twinning. Based on the results obtained in this investigation, it was speculated that the mode of deformation, rather than the substructure, of martensite controlled the toughness of the steels.
10. The fracture toughness, K_{IC}, is a very structure sensitive material property. Even small changes in microstructure caused noticable changes in K_{IC} values.
11. K_{IC} is an unique engineering parameter and can be obtained only by fracture tests. Correlations of tensile properties and fracture toughness have thus far proved unsuccessful. No correlation between the fracture toughness values and the ductilities obtained in tension tests was observed.
12. Charpy impact values were useful in obtaining an indication regarding the failure of the steel under extreme loading conditions. They are not very sensitive to microstructure changes though they follow the same trend as the K_{IC} values.
13. An excellent correspondence between fracture toughness and fractographic morphology was observed.

ACKNOWLEDGEMENTS

The author wishes to express his grateful appreciation to Professor Gareth Thomas for his encouragement and support throughout the course of the work. Appreciation is also extended to Professor Earl Parker and Professor Frank Hauser for their review and critical comments of this manuscript and Dr. Roger Goolsby and Dr. W. W. Gerberich for many helpful discussions.

The author takes this opportunity to thank the technical staff of the Inorganic Materials Research Division of the Lawrence Berkeley Laboratory. Special thanks are extended to Don Krieger (mechanical testing), J. A. Patenaude, Edwin Edwards (machine shop), Lee Johnson (metallography), John Holthius (alloy preparation), and Phila Witherell (photography) for their extensive help. The author expresses deep appreciation to Jean Wolslegel and Carol ZumBrunnen for their patience and endurance in typing this manuscript.

This work was performed under the auspices of the United States Atomic Energy Commission, through the Inorganic Materials Research Division of the Lawrence Berkeley Laboratory.

APPENDIX I.

Computer output of variation of Y parameter $\left(= \frac{KBW^{1/2}}{P}\right)$ with $(\frac{a}{w})$ values for a WOL specimen for the K calibration:

$$Y = \frac{KBW^{1/2}}{P} =$$

$$\left[29.6\ (\tfrac{a}{w})^{1/2} - 185.5\ (\tfrac{a}{w})^{3/2} + 655.7\ (\tfrac{a}{w})^{5/2} - 1017.0\ (\tfrac{a}{w})^{7/2} + 638.9\ (\tfrac{a}{w})^{9/2}\right]$$

$(\frac{a}{w})$	Y	$(\frac{a}{w})$	Y
.45000	8.33764	.47500	8.93225
.45100	8.36015	.47600	8.95751
.45200	8.38277	.47700	8.98289
.45300	8.40548	.47800	9.00840
.45400	8.42830	.47900	9.03403
.45500	8.45122	.48000	9.05979
.45600	8.47424	.48100	9.08568
.45700	8.49736	.48200	9.11170
.45800	8.52059	.48300	9.13784
.45900	8.45392	.48400	0.16412
.46000	8.56735	.48500	9.19053
.46100	8.59090	.48600	9.21707
.46200	8.61455	.48700	9.24374
.46300	8.63831	.48800	9.27056
.46400	8.66218	.48900	9.29751
.46500	8.68616	.49000	9.32460
.46600	8.71025	.49100	9.35182
.46700	8.73445	.49200	9.37919
.46800	8.75877	.49300	9.49671
.46900	8.78320	.49400	9.43436
.47000	8.80775	.49500	9.46216
.47100	8.83241	.49600	9.49011
.47200	8.85719	.49700	9.51821
.47300	8.88209	.49800	9.54645
.47400	8.90711	.49900	9.67485

$(\frac{a}{w})$	Y	$(\frac{a}{w})$	Y
.50000	9.60339	.53400	10.67580
.50100	9.63210	.53500	10.71070
.50200	9.68997	.53600	10.74581
.50300	9.71914	.53700	10.78113
.50500	9.74847	.53800	10.81667
.50600	9.77796	.53900	10.85243
.50700	9.80762	.54000	10.88842
.50800	9.83743	.54100	10.92462
.50900	9.86742	.54200	10.96106
.51000	9.89757	.54300	10.99772
.51100	9.92789	.54400	11.03461
.51200	9.95838	.54500	11.07173
.51300	9.98905	.54600	11.10909
.51400	10.01989	.54700	11.14669
.51500	10.05090	.54800	11.18452
.51600	10.08209	.54900	11.22260
.51700	10.11346	.55000	11.26092
.51800	10.14501	.55100	11.29948
.51900	10.17674	.55200	11.33829
.52000	10.20866	.55300	11.37736
.52100	10.24076	.55400	11.41667
.52200	10.27305	.55500	11.45624
.52300	10.30553	.55600	11.49607
.52400	10.33819	.55700	11.53615
.52500	10.37106	.55800	11.57650
.52600	10.40411	.55900	11.61711
.52700	10.43737	.56000	11.65799
.52800	10.47082	.56100	11.69914
.52900	10.50447	.56200	11.74055
.53000	10.53833	.56300	11.78224
.53100	10.57238	.56400	11.82421
.53200	10.60665	.56500	11.86646
.53300	10.64112	.56600	11.90898

$(\frac{a}{w})$	Y	$(\frac{a}{w})$	Y
.56700	11.95180	.59900	13.48738
.56800	11.99489	.60000	13.54107
.56900	12.03828	.60100	13.59513
.57000	12.08195	.60200	13.64959
.57100	12.12592	.60300	13.70442
.57200	12.17019	.60400	13.75965
.57300	12.21476	.60500	13.81527
.57400	12.25962	.60700	13.92769
.57500	12.30480	.60800	13.98451
.57600	12.35027	.60900	14.04173
.57700	12.39606	.61000	14.09935
.57800	12.44216	.61100	14.15739
.57900	12.48858	.61200	14.21584
.58000	12.53531	.61300	14.27472
.58100	12.58236	.61400	14.33401
.58200	12.62974	.61500	14.39373
.58300	12.67744	.61600	14.45388
.58400	12.72547	.61700	14.51445
.58500	12.77384	.61800	14.57047
.58600	12.82254	.61900	14.63692
.58700	12.87157	.62000	14.69882
.58800	12.92095	.62100	14.76116
.58900	12.97067	.62200	14.82395
.59000	13.02073	.62300	14.88719
.59100	13.07114	.62400	14.95089
.59200	13.12191	.62500	15.91505
.59300	13.17303	.62600	15.07967
.59400	13.22451	.62700	15.14476
.59500	13.27635	.62800	15.21032
.59600	13.32855	.62900	15.27636
.59700	13.38112	.63000	15.34287
.59800	13.43406	.63100	15.40986

$(\frac{a}{w})$	Y	$(\frac{a}{w})$	Y
.63200	15.47735	.66500	18.00213
.63300	15.54532	.66600	18.08847
.63400	15.61378	.66700	18.17545
.63500	15.68274	.66800	18.26305
.63600	15.65220	.66900	18.35130
.63700	15.82216	.67000	18.44018
.63800	15.89264	.67100	18.52972
.63900	15.96362	.67200	18.61990
.64000	16.03512	.67300	18.71074
.64100	16.10715	.67400	18.80224
.64200	16.17969	.67500	18.89440
.64300	16.25276	.67600	18.98724
.64400	16.32637	.67700	19.08075
.64500	16.40051	.67800	19.17493
.64600	16.47519	.67900	19.26980
.64700	16.55041	.68000	19.36536
.64800	16.62618	.68100	19.46161
.64900	16.70251	.68200	19.55856
.65000	16.77939	.68300	19.65621
.65100	16.85683	.68400	19.75456
.65200	16.93483	.68500	19.85363
.65300	17.01340	.68600	19.95342
.65400	17.09255	.68700	20.05393
.65500	17.17227	.68800	20.15516
.65600	17.25257	.68900	20.25731
.65700	17.33346	.69000	20.35983
.65800	17.41493	.69100	20.46327
.65900	17.49700	.69200	20.56746
.66000	17.57967	.69300	20.67240
.66100	17.66294	.69400	20.77810
.66200	17.74681	.69500	20.88456
.66300	17.83130	.69600	20.99178
.66400	17.91640	.69700	21.09978

$(\frac{a}{w})$	Y	$(\frac{a}{w})$	Y
.69800	21.20855	.72900	24.99454
.69900	21.31810	.73000	25.13099
.70000	21.42844	.73100	25.26840
.70100	21.53958	.73200	25.40677
.70200	21.65151	.73300	25.54611
.70300	21.76424	.63400	25.68643
.70400	21.87778	.73500	25.82773
.70500	21.99213	.73600	25.97001
.70600	21.10730	.73700	26.11329
.70700	22.10730	.73800	26.25756
.70700	22.22330	.73900	26.40285
.70800	22.34012	.74000	26.54914
.70900	22.45778	.74100	26.69645
.71000	22.57628	.74200	26.84478
.71100	22.69562	.74300	26.99414
.71200	22.81581	.74400	27.14454
.71300	22.93686	.74500	27.29598
.71400	23.05877	.74600	27.44847
.71500	23.18155	.74700	27.60202
.71600	23.30520	.74800	27.75662
.71700	23.42972	.47900	27.91229
.71800	23.55513	.75000	28.06903
.71900	23.68143	.75100	28.22686
.72000	23.80862		
.72100	23.93671		
.72200	24.06571		
.72300	24.19562		
.72400	24.32645		
.72500	24.45820		
.72600	24.59088		
.72700	24.72449		
.72800	24.85904		

REFERENCES

1. G. Thomas, D. Schmatz and W. Gerberich, High Strength Materials, V. F. Zackay, Ed., (John Wiley and Sons, Inc., New York, N. Y., 1965) p. 324.
2. E. W. Page, P. Manganon, Jr., G. Thomas, and V. F. Zackay, Trans. ASM 62, 45 (1969).
3. V. F. Zackay, E. R. Parker, D. Fahr and R. Busch, Trans. ASM 60, 252 (1967).
4. P. G. Winchell and M. Cohen, Trans. ASM. 55, 347 (1962).
5. P. M. Kelly and J. Nutting, Proc. Royal Soc. A259, 45 (1960).
6. P. M. Kelly and J. Nutting, J. Iron Steel Inst. 197, 199 (1961).
7. A. R. Marder and G. Krauss, Trans. Amer. Soc. Metals 60, 651 (1967).
8. M. Raghavan and G. Thomas, Met. Trans 2, 3433 (1971).
9. G. Thomas, Met. Trans. 2, 2373 (1971).
10. R. L. Patterson and C. M. Wayman, Acta Met. 12, 1306 (1964).
11. O. Johari and G. Thomas, Acta Met. 13, 1211 (1965).
12. K. W. Andrews, J. Iron Steel Inst., 721 (1965).
13. O. Johari and G. Thomas, Trans. ASM 58, 563 (1965).
14. S. K. Das and G. Thomas, Trans. Amer. Soc. Metals 62, 659 (1969).
15. D. H. Huang and G. Thomas, Met. Trans. 2, 1587 (1971).
16. Chilton and Kelly, Acta Met. 16, 637 (1968).
17. C. L. Magee and R. G. Davies, Met. Trans. 1, 2927 (1970).
18. C. L. Magee and R. G. Davies, Acta Met. 19, 345 (1971).
19. W. F. Brown, Jr., and J. E. Srawley, Plane Strain Crack Toughness Testing of High Strength Metallic Materials, ASTM STP 410, (American Society for Testing and Materials, Philadelphia, 1967).

20. Annual Book of ASTM Standards, Part 31, (American Society for Testing and Materials, Philadelphia, 1967).

21. S. R. Keown and F. B. Pickering, J. Iron Steel Inst. 199, 757 (1962).

22. R. L. Miller, Trans. ASM 57, 892 (1964).

23. W. S. Owen, E. A. Wilson and T. Bell, High Strength Materials, V. F. Zackay, Ed. (John Wiley & Sons, Inc., New York, N. Y., 1965) p. 167.

24. G. Thomas, Lectures for 2nd Conference on Materials Science, Tremezzo, Italy, September 14-25, (1970), UCRL-19697.

25. C. J. Barton, Acta Met. 17, 1985 (1969).

26. R. D. Goolsby, University of California, (Ph. D. Thesis), LBL 405, Dec. 1971.

27. G. R. Speich and P. R. Swann, J. Iron Steel Inst. 203, 480 (1965).

28. P. M. Kelly and C. Pollard, Acta Met. 17, 1005 (1969).

29. R. A. Grange, Trans. Amer. Soc. Metals 59, 26 (1966).

30. A. W. Sleeswyk and C. A. Verbraak, Acta Metl 9, 917 (1961).

31. J. R. Mihalisin, Trans. Asm 59, 60 (1966).

32. C. D. Beachem and R. M. N. Pelloux, Fracture Toughness Testing and Its Applications , ASTM STP 381, (American Society for Testing and Materials, Philadelphia, 1965) p. 210.

33. W. A. Spitzig, Electron Microfractography, ASTM STP 453, (American Society for Testing and Materials, Philadelphia, 1968) p. 90.

34. R. H. Richman, Trans. Amer. Inst. Min. Engrs 227, 159 (1963).

35. C. H. Shih, B. L. Averbach, and Morris Cohen, Trans. Amer. Soc. Metals 48, 86 (1965).

36. C. J. Altstetter, Morris Cohen, and B. L. Averbach, Trans. Amer. Soc. Metals 55, 287 (1962).

37. J. H. Bucher, Application of Fracture Toughness Parameters to Structural Metals, Herman D. Greenberg, Ed., (Gordon and Breach, New York, 1966) p. 323.

38. E. B. Kula and A. A. Anctil, J. Mater. 4 (4), 817 (1969).

39. J. M. Capus and G. Mayer, Metallurgia 62, 133 (1960).

40. J. M. Capus, J. Iron Steel Inst. 201, 53 (1963).

41. M. A. Grossman, Trans. AIME 167, 39 (1946).

42. R. L. Rickett and J. M. Hodge, Amer, Soc. Testing Mater. Proc. 51, 931 (1951).

43. L. J. Klingler, W. J. Barnett, R. P. Frohmberg, and A. R. Troiano, Trans. Amer. Soc. Metals 46, 1557 (1954).

44. B. S. Lement, B. L. Averbach, and MOrris Cohen, Trans. Amer. Soc. Metals 46, 851 (1954).

45. Bani R. Banerjee, Structure and Properties of Ultrahigh-Strength Steels, ASTM STP 370, (American Society for Testing and Materials, Philadelphia, 1965) p. 94.

46. B. R. Banerjee, J. Iron Steel Inst. 203, 166 (1965).

47. A. R. Marder and A. O. Benscoter, Trans. Amer. Soc. Metals 61, 293 (1968).

48. G. T. Hahn and A. R. Rosenfield, Applications Related Phenomena in Titanium and Its Alloys, ASTM STP 432, (American Society for Testing and Materials, Philadelphia, 1968) p. 5.

49. M. H. Jones and W. F. Brown, Jr., Review of Developments in Plane Strain Fracture Toughness Testing, ASTM STP 463, W. F. Brown, Jr., Ed. (American Society for Testing and Materials, Philadelphia, 1970) p. 216.

Table I

Composition of alloys used in the investigation.

Alloy Designation	Alloy Composition %			
	Fe	Ni	Co	C
T	Bal.	28.5	10	----
U	Bal.	25	10	----
TC	Bal.	27	10	0.10
UC	Bal.	19	10	0.10

Table II. Mechanical properties of steels T and U at 25°C.

Heat No.	Yield Strength, σ_y (Ksi)	Ultimate Strength, σ_u (Ksi)	% Elongation	True Fracture Strain, ε_f	Strain Hardening Index, n	Charpy Impact Value ft. lbs.	K_{IC} (Calc) (Ksi $\sqrt{in.}$)
T	95	100	11.5	0.109	0.037	94	16.4
U	101	121	8.5	0.08	0.016	114	6.30

Table III. Technical properties of steels T and U at -196°C.

Heat No.	Yield Strength, σ_y (Ksi)	Ultimate Strength, σ_u (Ksi)	% Elong.	True Fracture Strain, ε_f	Strain Hardening Index,	Charpy Impact Value (ft. lbs)	K_Q* (meas.) (Ksi $\sqrt{in}$)	K_{IC}** (min) (Ksi $\sqrt{in}$)	K_{IC}† (Calc) (Ksi $\sqrt{in}$)	K_{Crit} (Ksi $\sqrt{in}$)
T	144	170	12.5	0.117	0.065	75	143	82.5	37	400.0
U	147	174	10.5	0.048	0.025	91	175	93.0	9	360.0

*The K_Q values obtained during the test are apparent values and do not qualify as valid K_{IC} values as per the ASTM Standards.[19]

**Maximum value of K_{IC} that could have been obtained at the given conditions of yield strength and specimen thickness based on $B \geq 2.5 \left(\frac{K_{IC}}{\sigma_y}\right)^2$ criterion.[19]

†K_{IC} values calculated based on Hahn and Rosenfield[48] model where $K_{IC} = \left[\frac{2}{3} E \varepsilon_f n^2 \sigma_y\right]^{1/2}$.

Table IV. Mechanical properties of steel UC at 25°C

	As Quenched	Tempering Temperature (°C)			
		100	200	300	400
Yield Strength, σ_y (Ksi)	126	130	130	132	133
Ultimate Strength, σ_u (Ksi)	147	151	151	149	150
% Elongation	3.0	8.0	8.0	7.0	6.0
True Fracture Strain, ε_f	0.03	0.078	0.078	0.067	0.060
Strain Hardening Index, n	0.016	0.023	0.028	0.018	0.023
Charpy Impact Value (ft. lbs)	10.5	10.5	10.5	12.0	40.0

Table V. Mechanical properties of steel UC at -196°C.

	As Quenched	Tempering Temperature (°C)			
		100	200	300	400
Yield Strength σ_y (Ksi)	176	172	180	177	196
Ultimate Strength, σ_u (Ksi)	198	200	180	191	204
% Elongation	9.6	5.3	---	5.8	12.0
True Fracture Strain, ε_f	0.092	0.053	---	0.058	0.114
Strain Hardening Index, n	0.05	0.037	---	0.04	0.0185
K_{IC} (meas) (Ksi $\sqrt{in}$)	60	70.5	57	60	71.0
K_{IC}* (calc) (Ksi $\sqrt{in}$)	27.5	15.2	---	17.5	12.0
K_{Crit} (Ksi $\sqrt{in}$)	92	116	91.5	81.5	90
$2.5\left(\frac{K_{IC}}{\sigma_y}\right)^2$	0.287	0.423	0.25	0.288	0.327

*K_{IC} value calculated from Hahn and Rosenfield model[48] where $K_{IC} = \left[\frac{2}{3} E \varepsilon_f n^2 \sigma_y\right]^{1/2}$.

Table VI. Mechanical properties of steel TC at 25°C.

	As Quenched	Tempering Temperature (°C)				
		100	200	300	400	500
Yield Strength, σ_y (Ksi)	120	115	114	113	130	135
Ultimate Strength, σ_u (Ksi)	142	134	125	129	134	140
% Elongation	12	8.2	10	9.7	11.7	140
True Fracture Strain, ϵ_f	0.114	0.078	0.095	0.092	0.11	0.13
Strain Hardening Index, n	0.069	0.046	0.0415	0.0345	0.0345	0.060
Charpy Impact Value, (ft. lbs)	20	18	18	23.0	42	40

Table VII. Mechanical properties of steel TC at -196°C.

	As Quenched	Tempering Temperature (°C)				
		100	200	300	400	500
Yield Strength, σ_y (Ksi)	165	155	156	170	186	205
Ultimate Strength, σ_u (Ksi)	200	18.6	188	194	205	210
% Elongation	15	10	12	8.0	10	8
True Fracture Strain, ε_f	0.13	0.095	0.114	0.074	0.095	0.074
Strain Hardening Index, n	0.10	0.055	0.048	0.055	0.08	0.018
K_{IC} (meas) (Ksi $\sqrt{in}$)	70	74	80	70	90	90
K_{IC}* (calc) (Ksi $\sqrt{in}$)	61.5	34.0	26	27	46	9.8
K_{Crit} (Ksi $\sqrt{in}$)	129	134	124	105	122	122
$2.5\left(\frac{K_{IC}}{\sigma_y}\right)^2$ (in.)	0.45	0.57	0.665	0.425	0.59	0.485
% Shear Lip	14	12	10	8	16	12

*K_{IC} value calculated from Hahn and Rosenfield model[48] where

$$K_{IC} = \left[\frac{2}{3} E \varepsilon_f n^2 \sigma_y\right]^{1/2}.$$

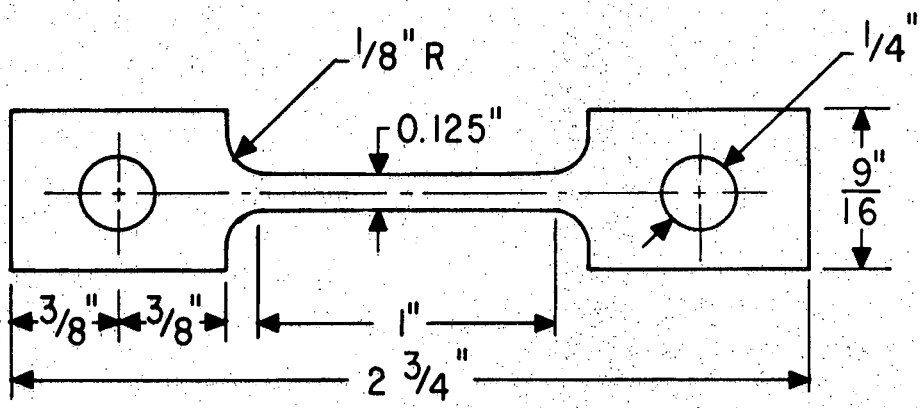

(a) TENSILE SPECIMEN THICKNESS = 0.10"

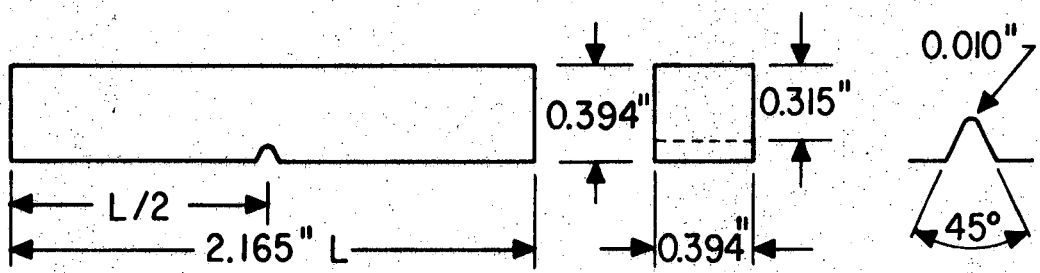

(b) CHARPY V-NOTCH IMPACT SPECIMEN

XBL 722-6018

Fig. 1 Dimensions of (a) a flat tensile specimen and (b) a standard Charpy specimen.

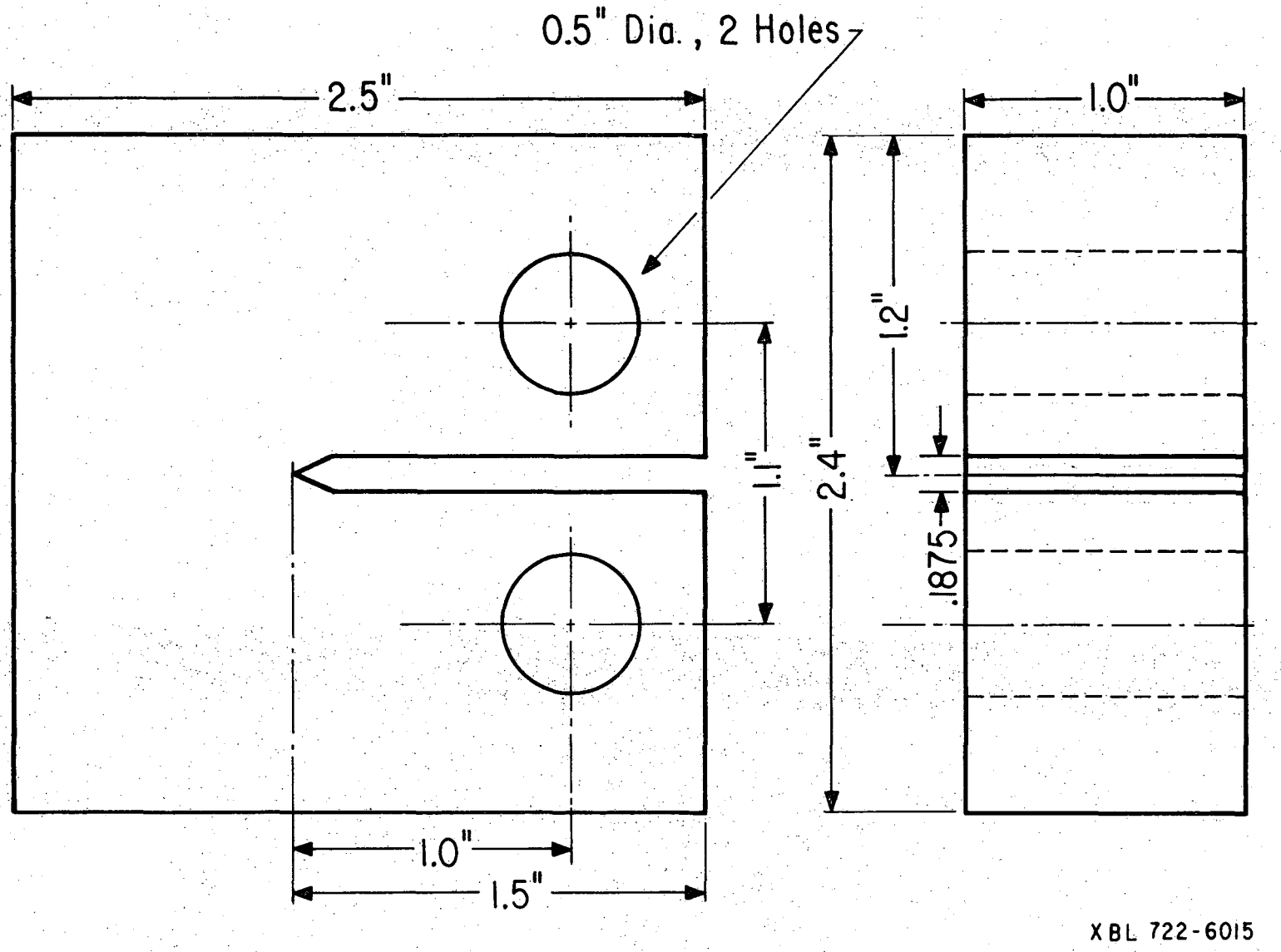

Fig. 2 Dimensions of a standard Compact Fracture Toughness specimen.

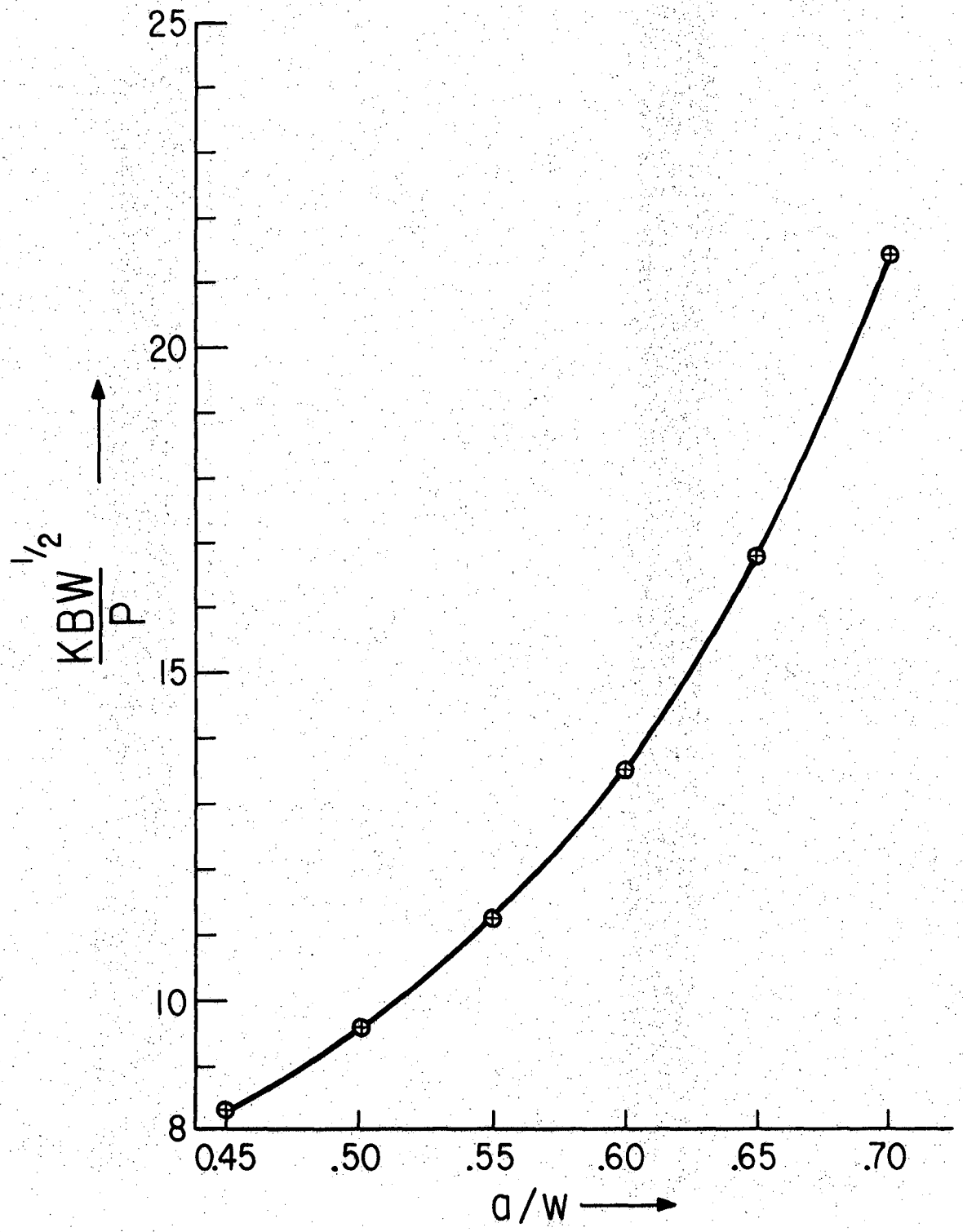

XBL 722-6017

Fig. 3 $\left(\frac{KBW}{P}^{1/2}\right)$ vs. $\left(\frac{a}{W}\right)$ plot for the Standard Fracture Toughness specimen.

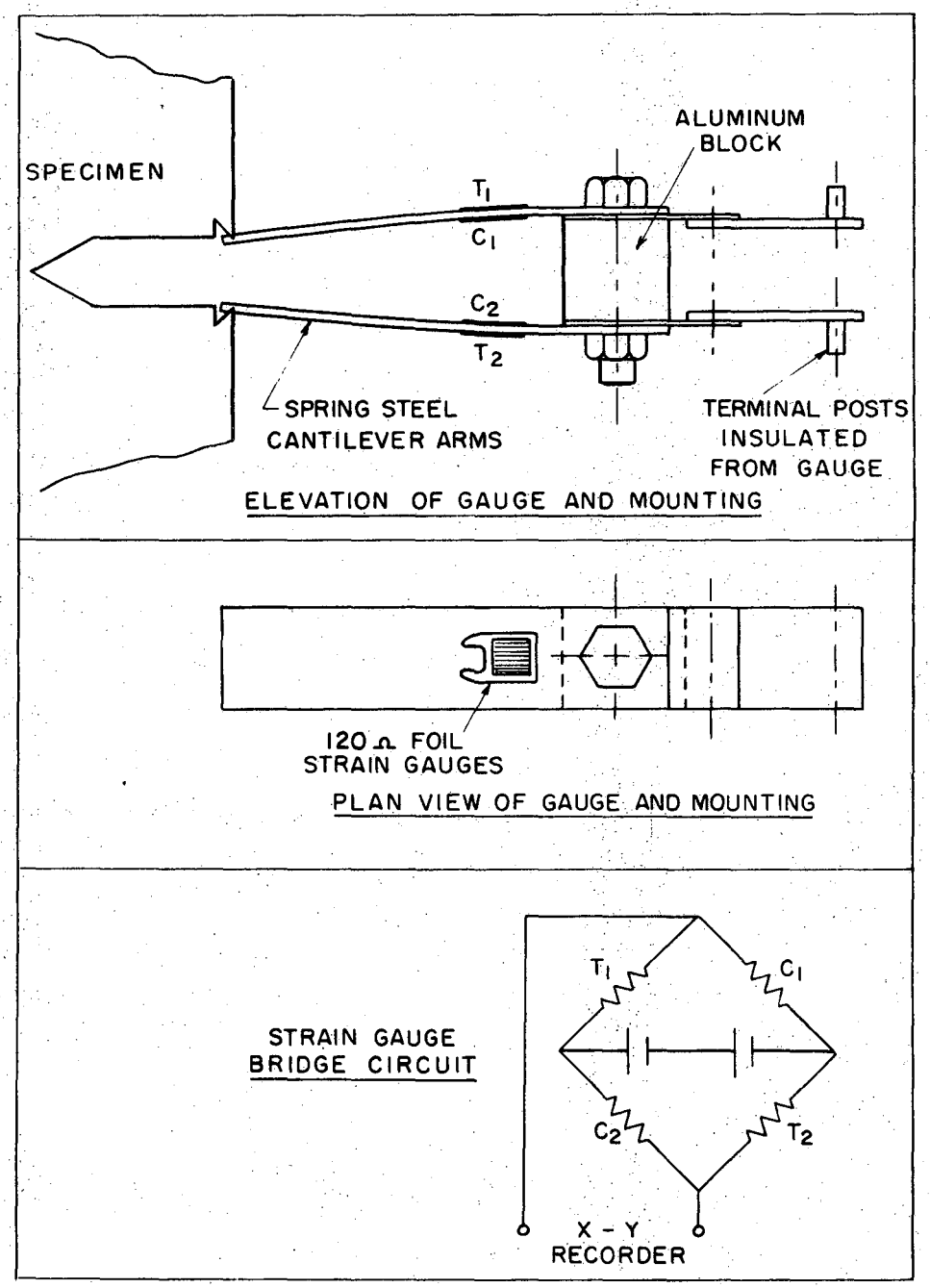

XBL 679-4971

Fig. 4 Double cantilever beam gauge and method of mounting on large single edge notched specimens for displacement measurement.

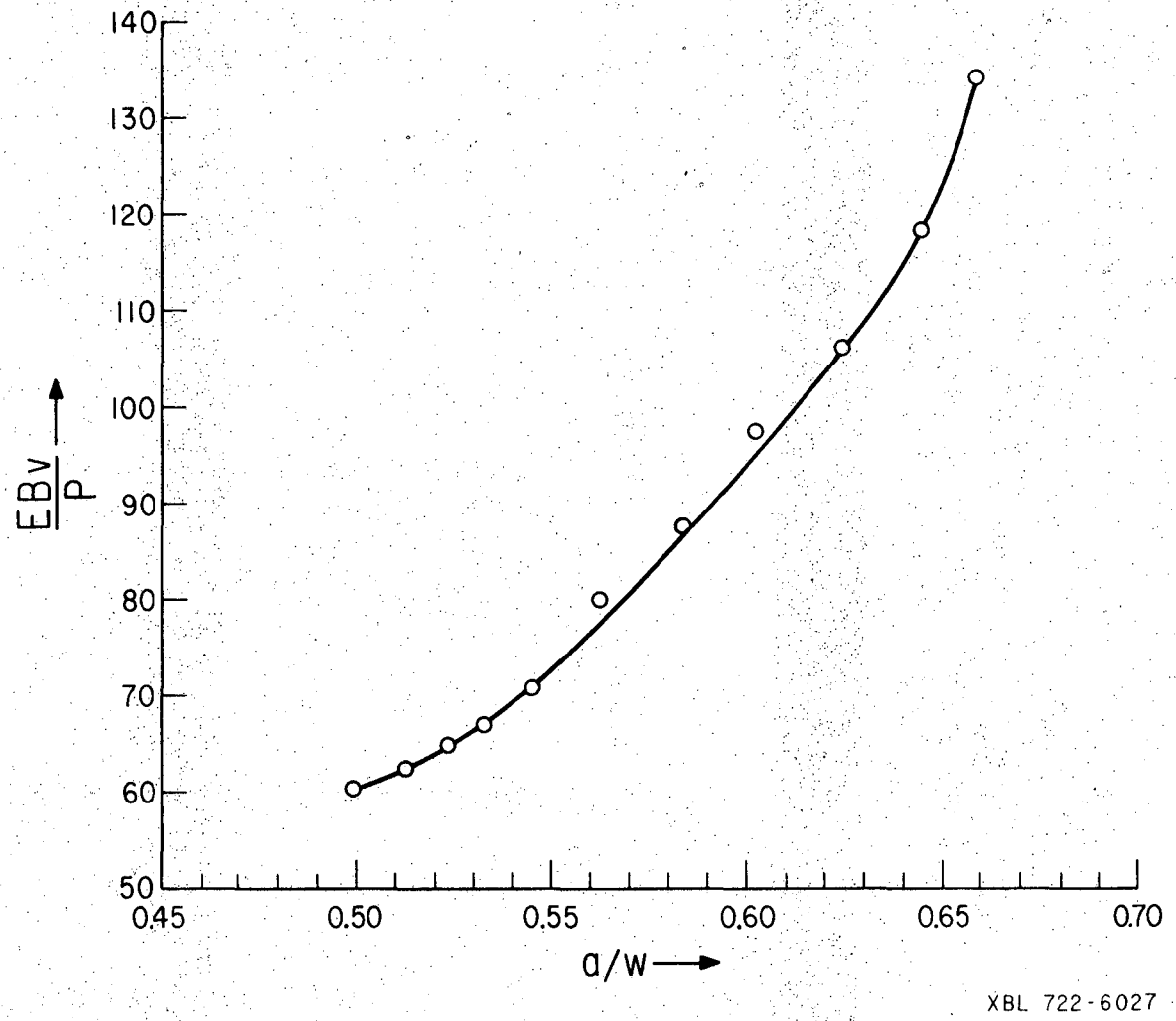

Fig. 5 $\left(\frac{EBv}{P}\right)$ vs. $\left(\frac{a}{w}\right)$ calibration for the Standard Fracture Toughness Specimen.

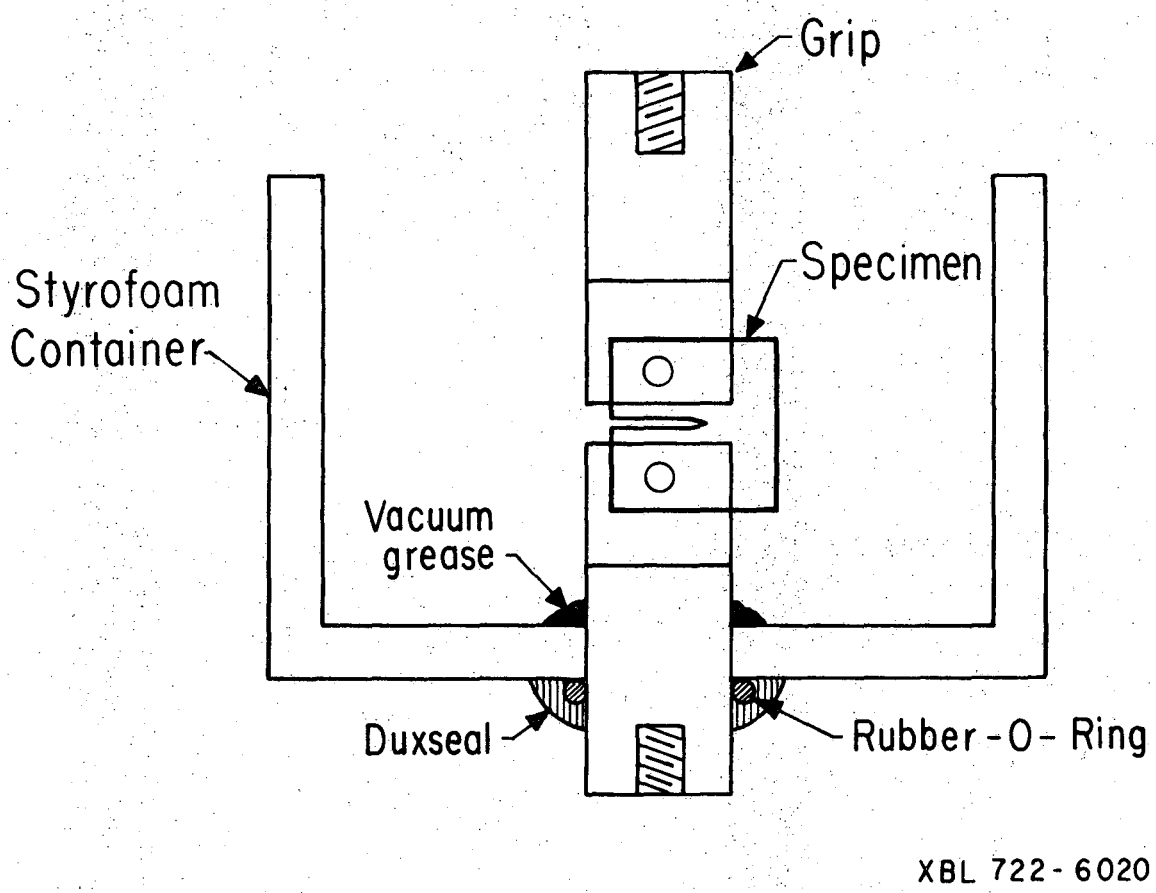

Fig. 6 Experimental set up for Liquid Nitrogen Fracture Toughness test.

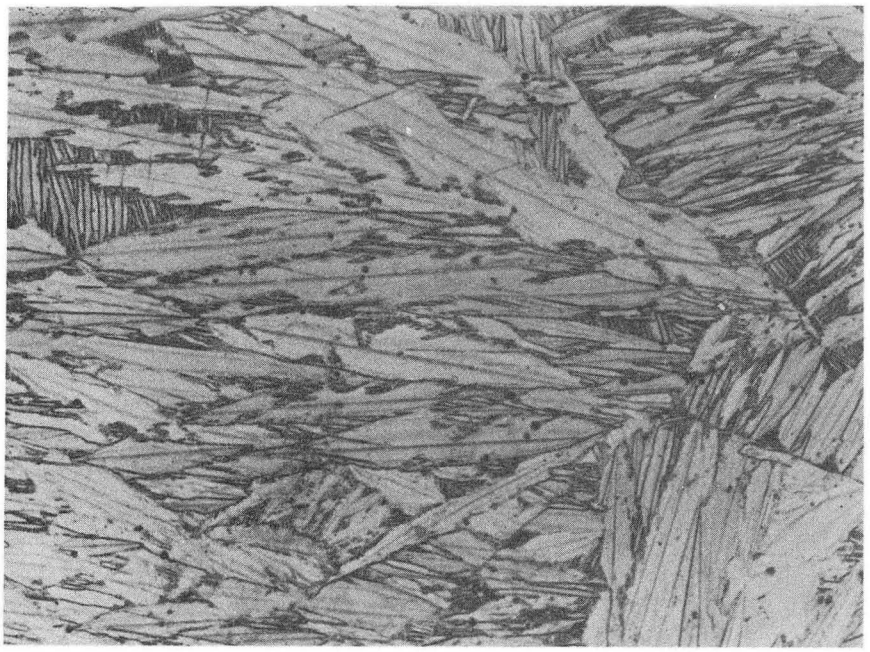

(A)

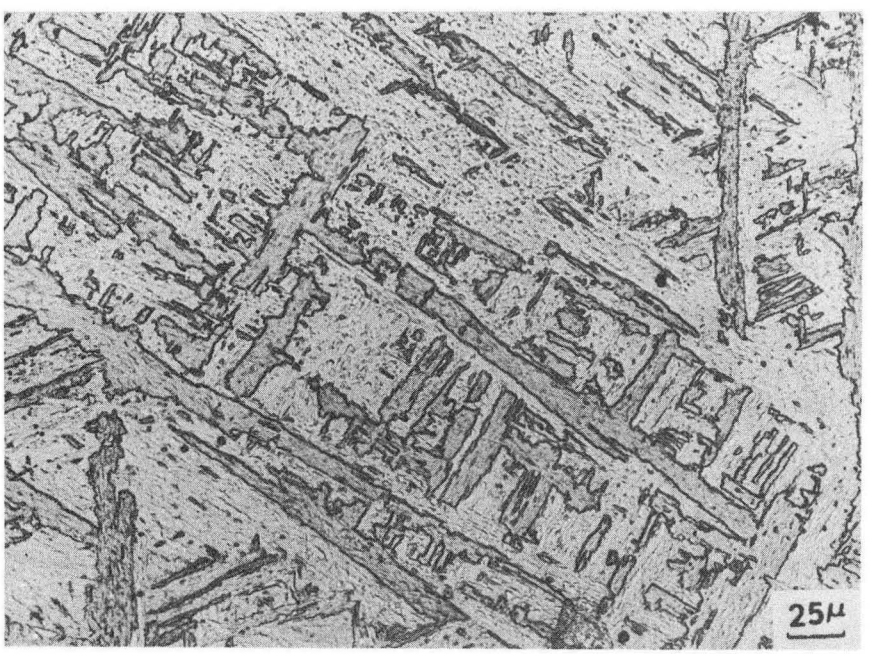

(B) XBB 721-304

Fig. 7 Optical micrographs of the as-quenched structures of alloys T in (A) and U in (B).

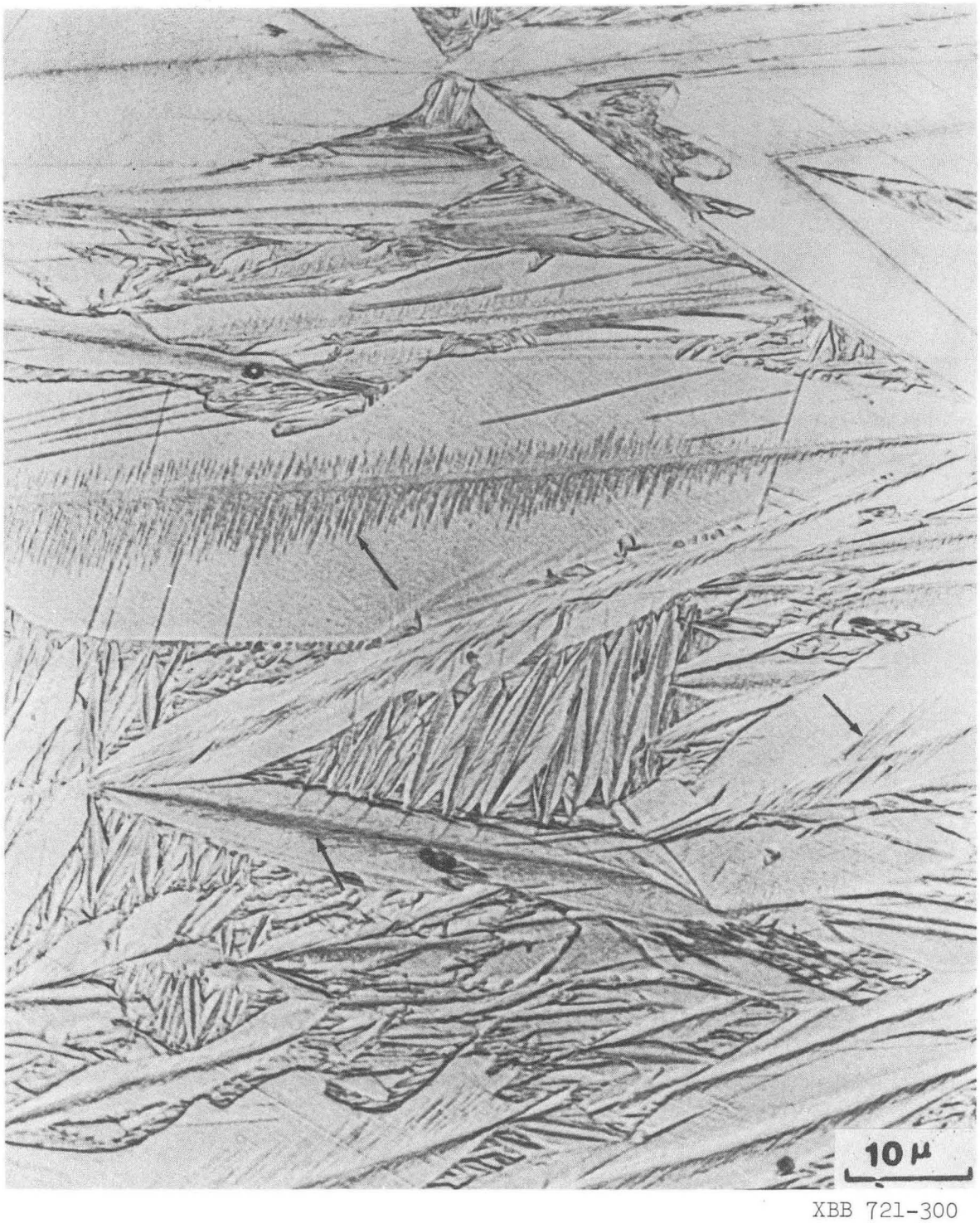

XBB 721-300

Fig. 8 Magnified image of twinned plates of alloy T showing twin markings (indicated by arrows).

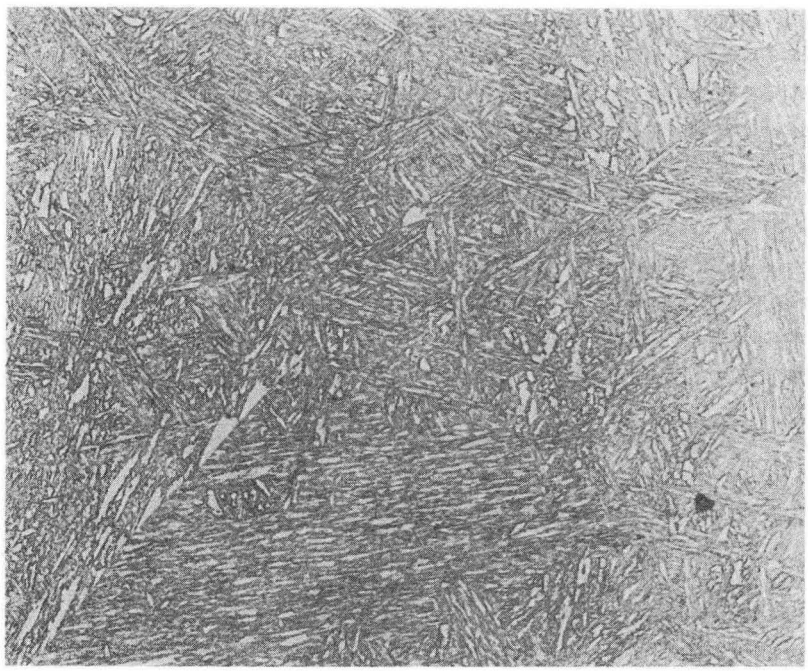

(A)

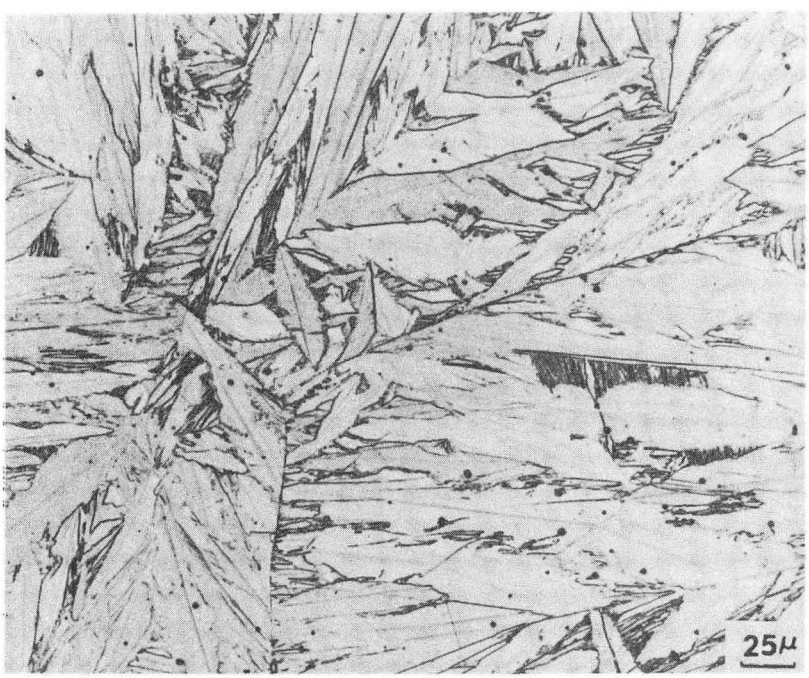

(B) XBB 721-389

Fig. 9 (A) Optical micrograph of steel UC, as-quenched, showing fine plates and laths and plates and (B) shows lenticular martensitic plates of steel TC in as-quenched condition.

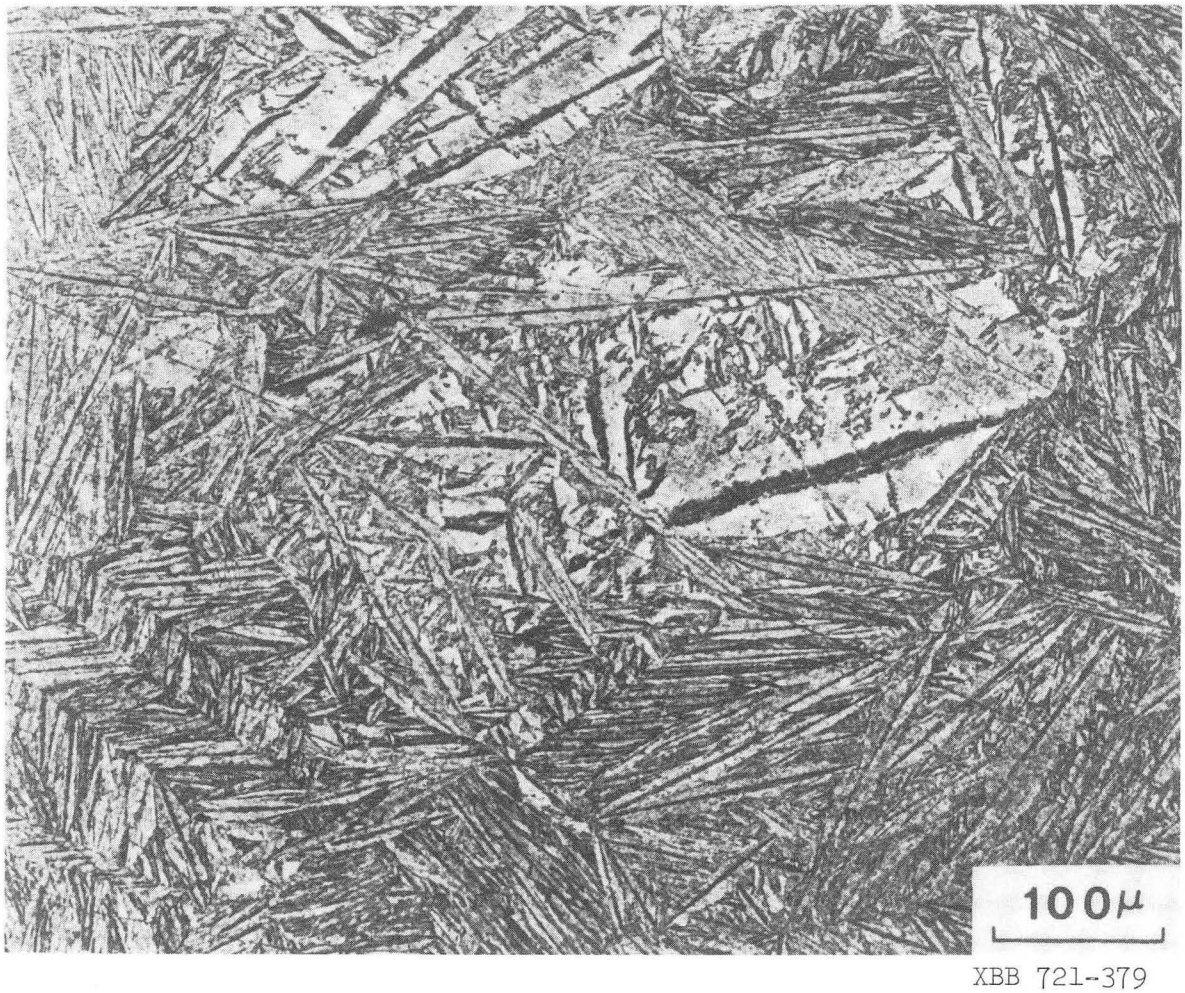

XBB 721-379

Fig. 10A Optical micrograph of steel TC, quenched and tempered at 300°C.

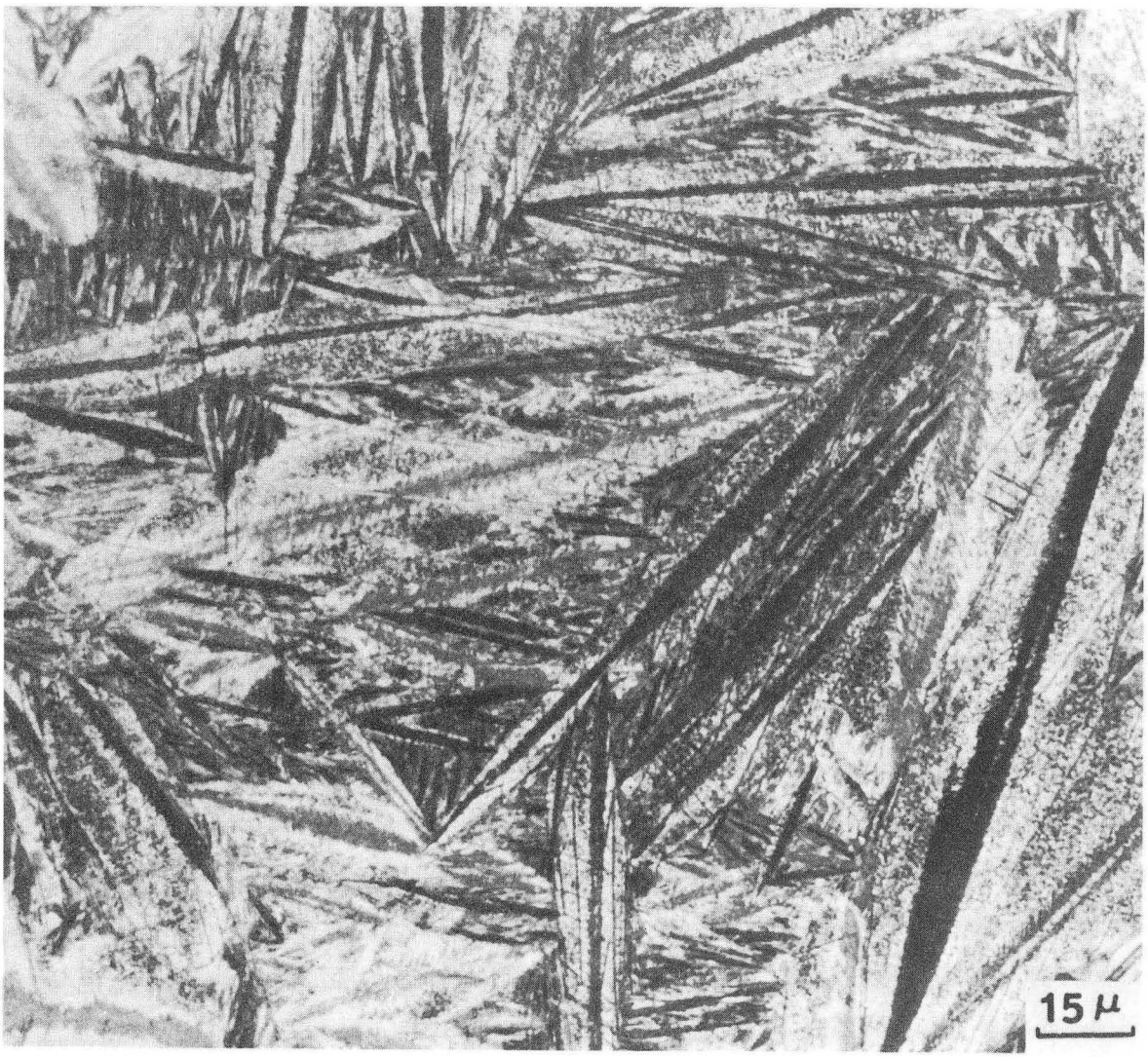

XBB 721-306

Fig. 10B Optical micrograph of steel TC, quenched and tempered at 500°C.

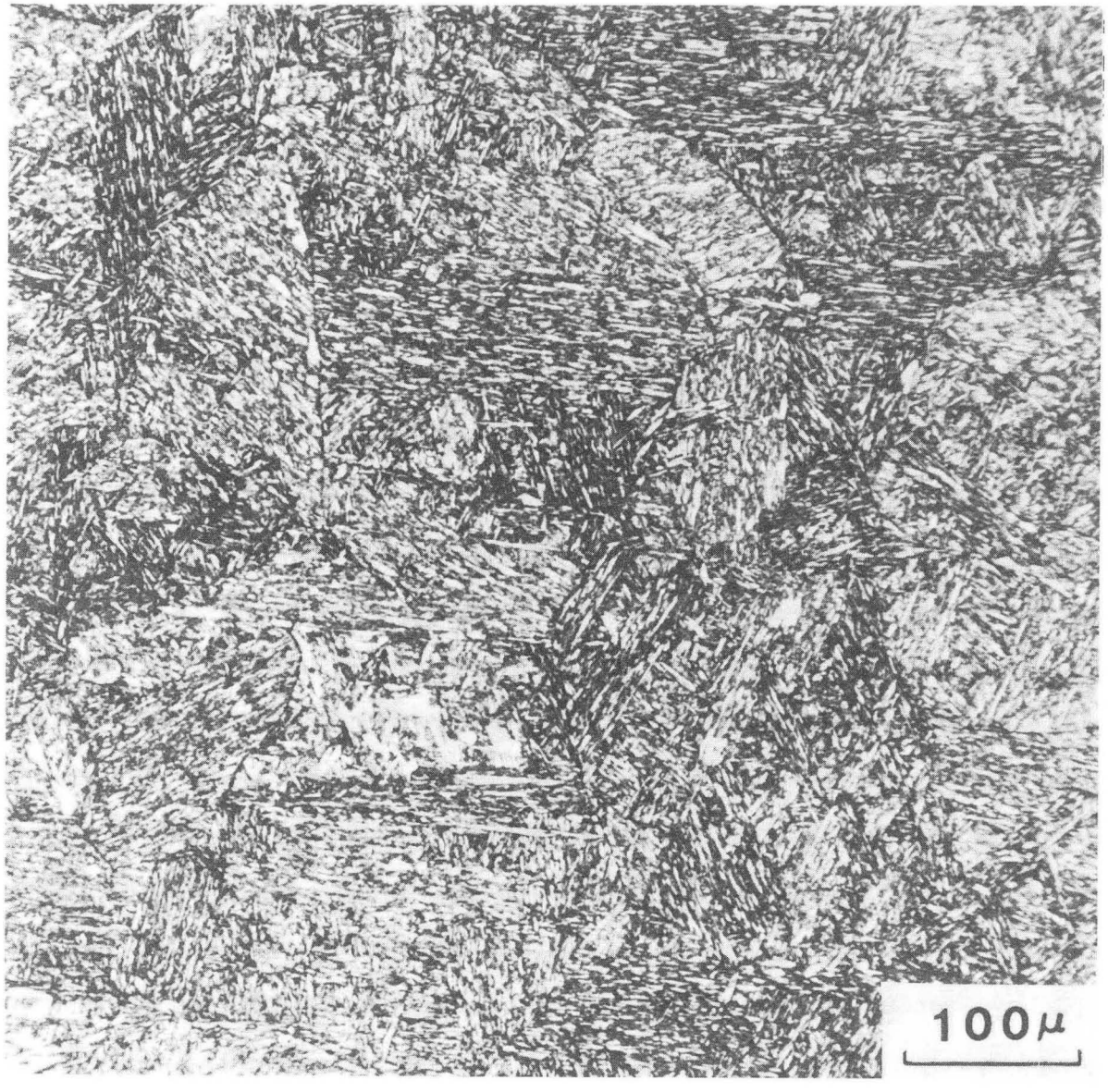

XBB 721-376

Fig. 11 Optical micrograph of steel UC, quenched and tempered at 200°C.

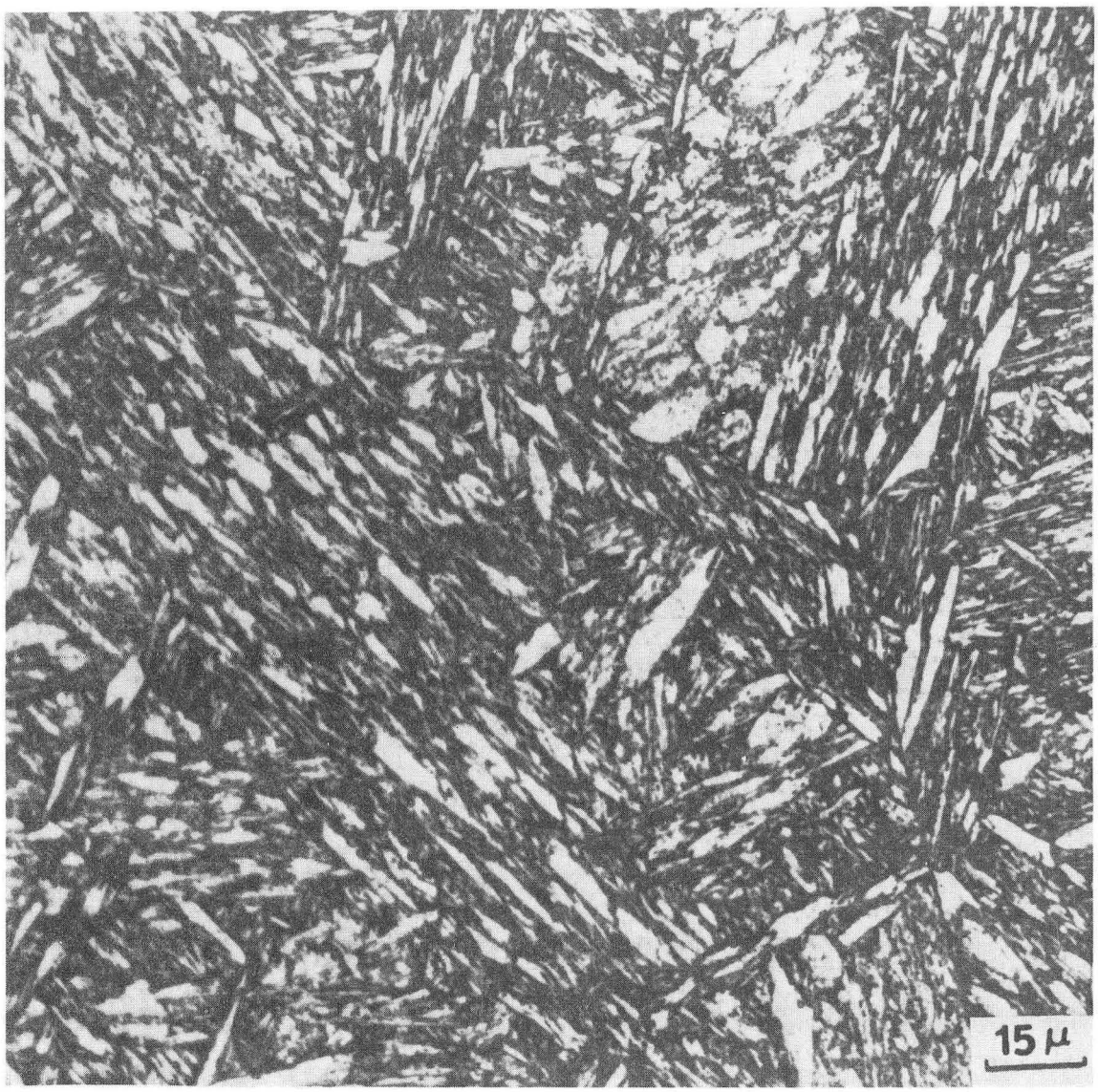

XBB 721-303

Fig. 12 Optical micrograph of steel UC, quenched and tempered at 400°C.

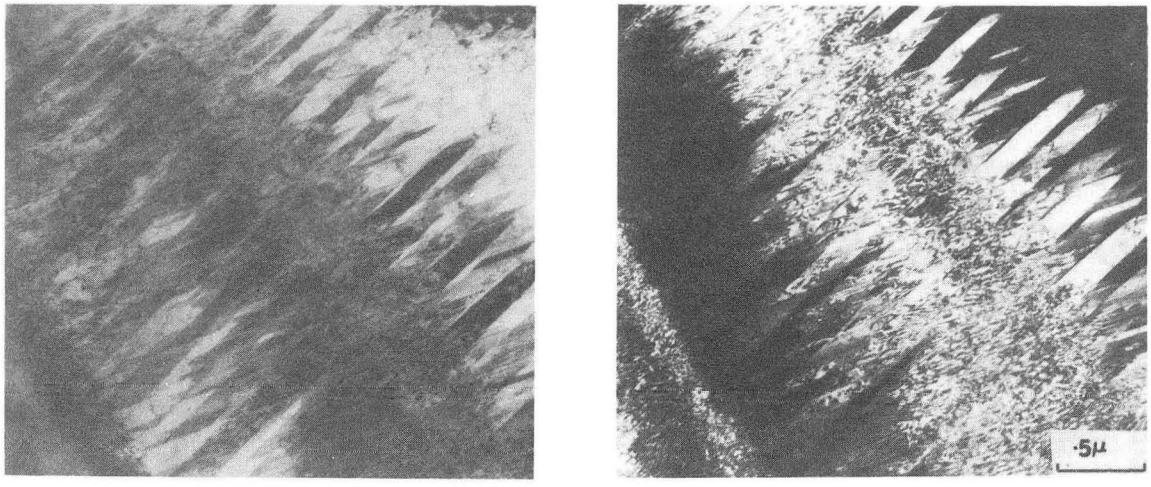

(A) (B)

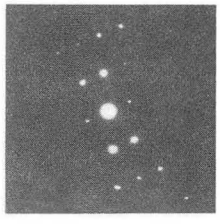

(C)

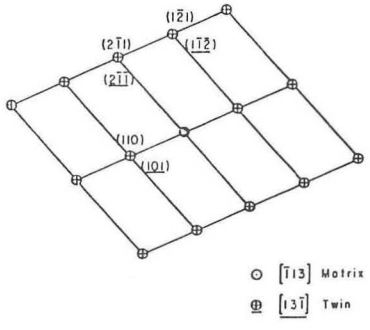

(D) XBB 722-754

Fig. 13 Alloy T as-quenched, (A) showing the bright field image of the twins in the martensite plates which reverse contrast in the dark field image. (B) The plate had a ($\bar{1}$13) orientation as shown in (C) and the indexing is shown in (D).

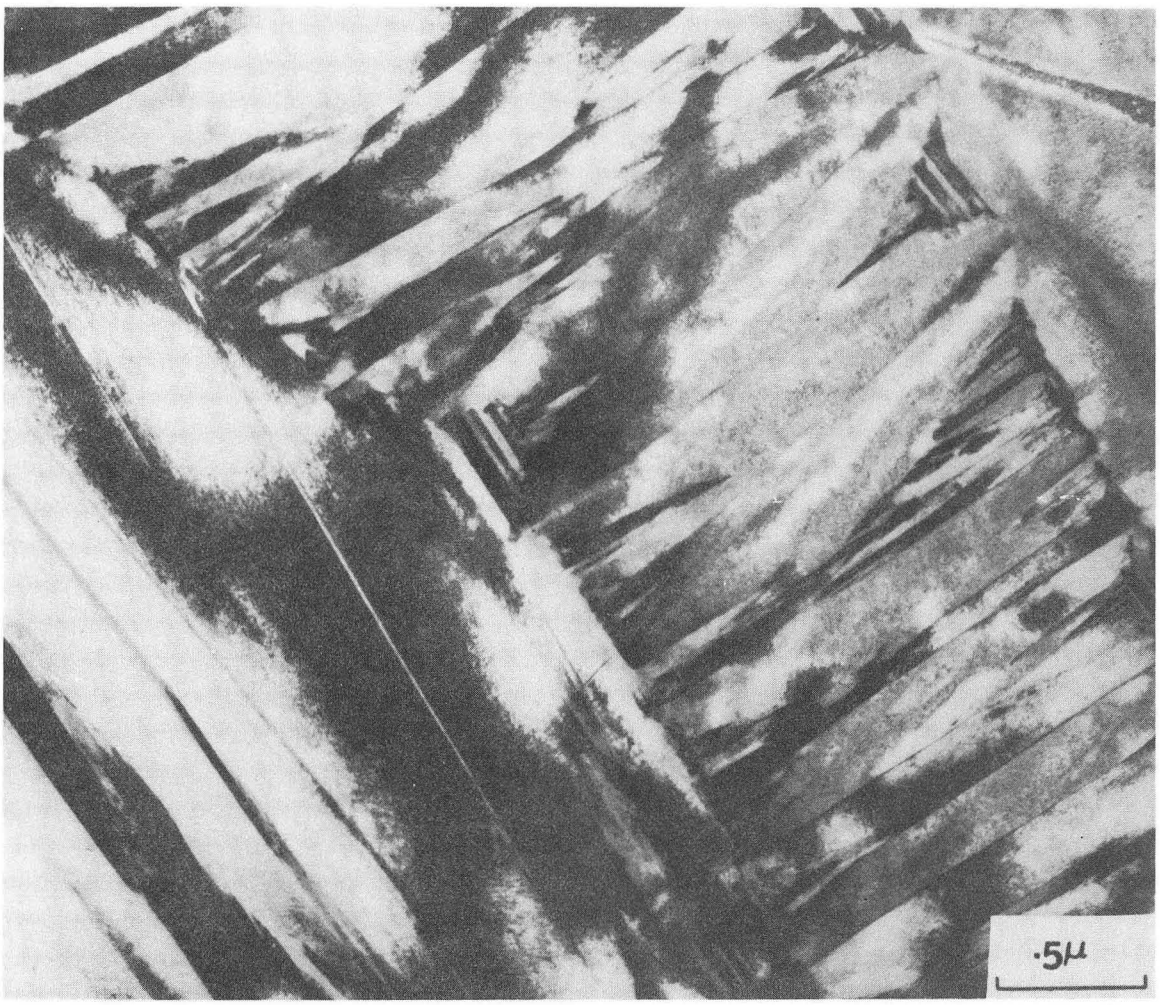

XBB 722-763

Fig. 14. Alloy T as-quenched, bright field image showing untwinned plates.

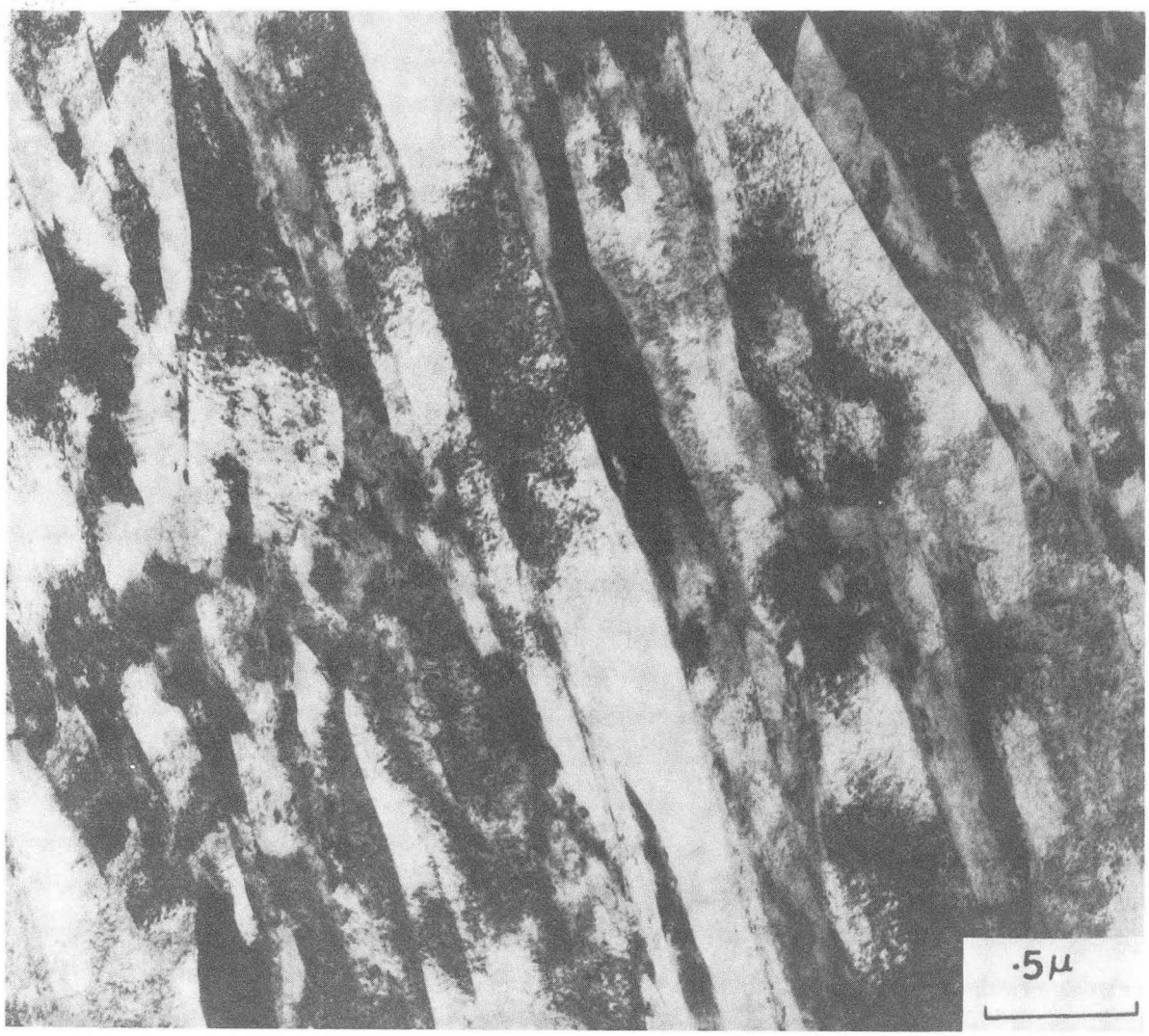

XBB 722-768

Fig. 15 Alloy U as-quenched, bright field micrograph showing martensite laths.

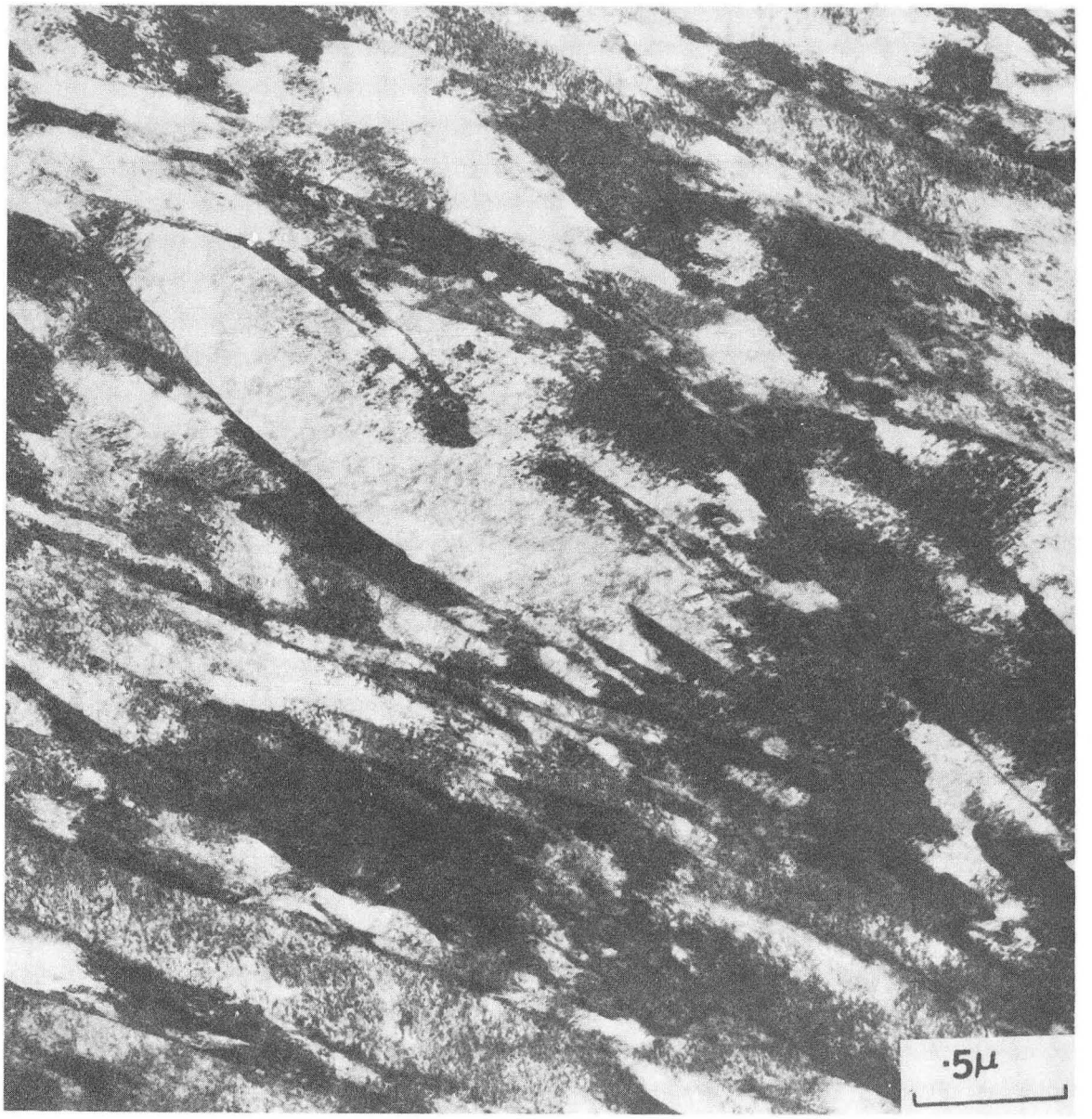

XBB 722-762

Fig. 16 Steel UC as-quenched, bright field micrograph representing the martensitic lath structure.

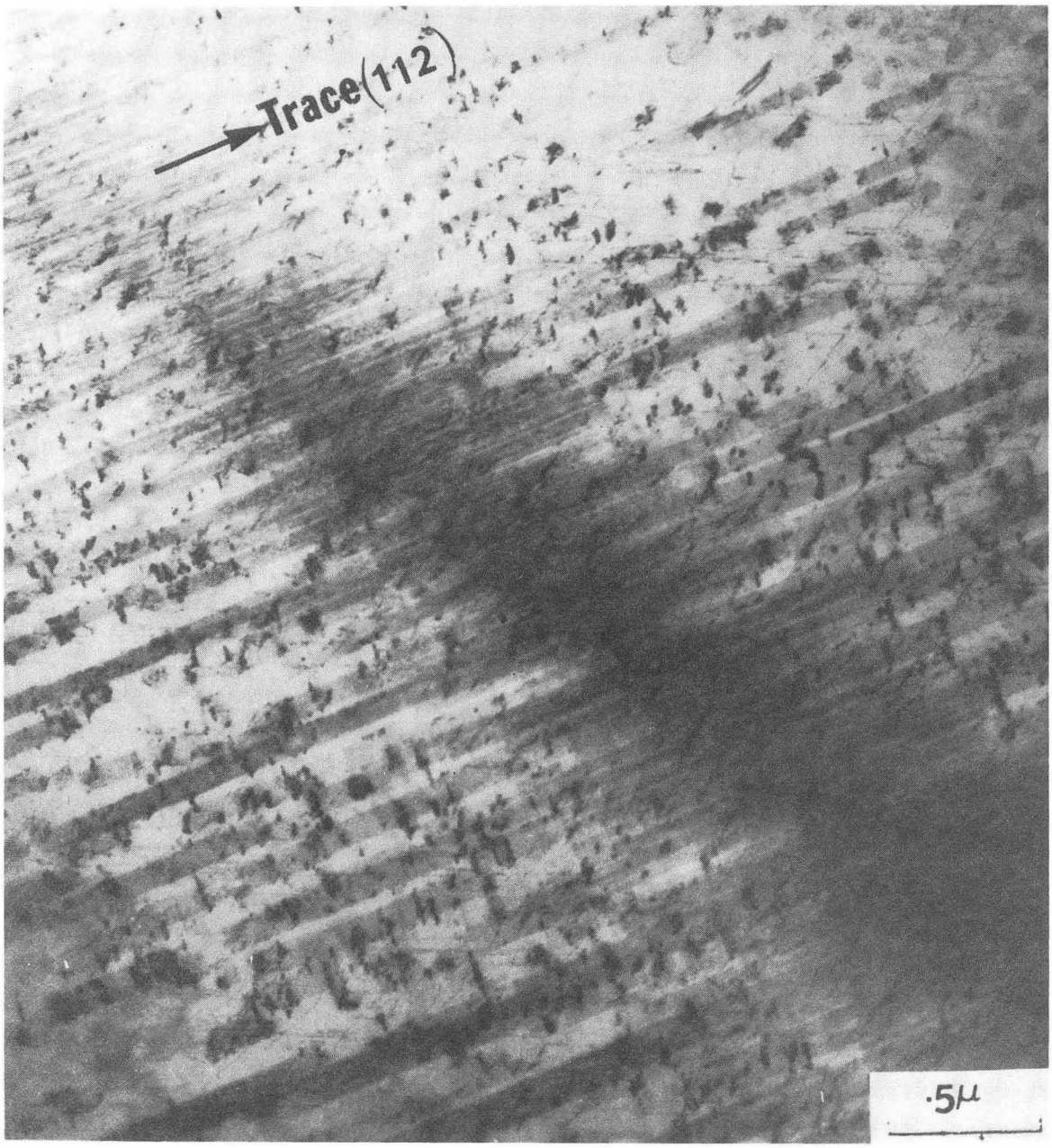

XBB 722-766

Fig. 17 Steel TC quenched and tempered at 200°C, showing nucleation of carbide (cementite) at the twins. The twin traces are faintly visible and are identified as (112) Traces.

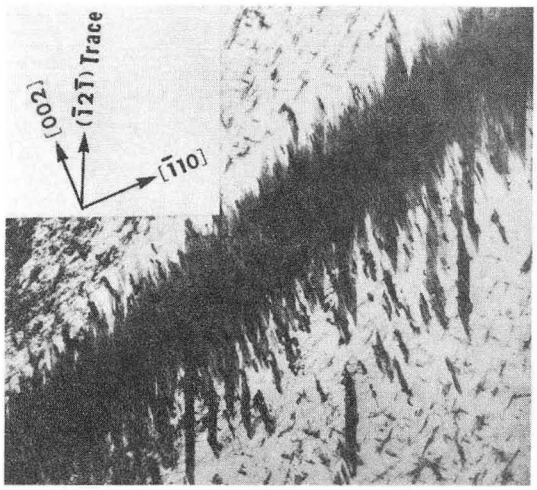

(A)

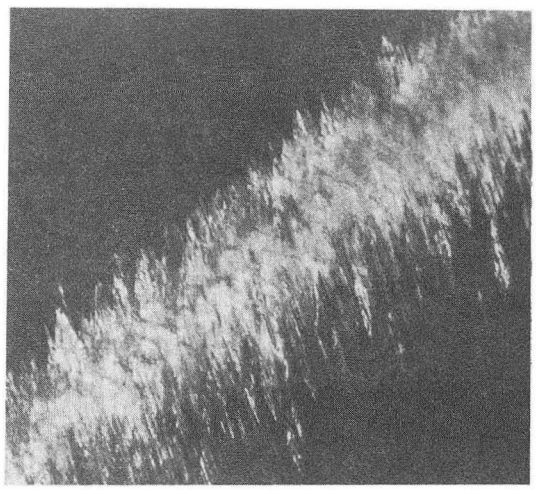

(B)

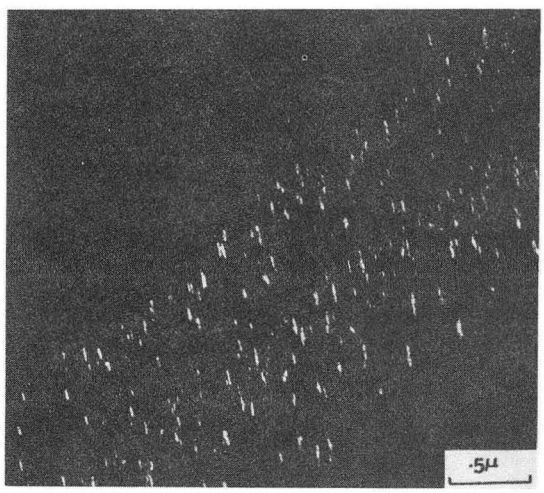

(C) XBB 722-755

Fig. 18 Steel TC quenched and tempered at 200°C, (A) bright field image indicating nucleation of carbides along the twin-matrix interface. A twin spot reverses contrast of the twins in the dark field image (B). (C) represents the dark field micrograph showing the reversal of contrast cementite that had preferentially nucleated along the twins. The foil was in a (110) orientation.

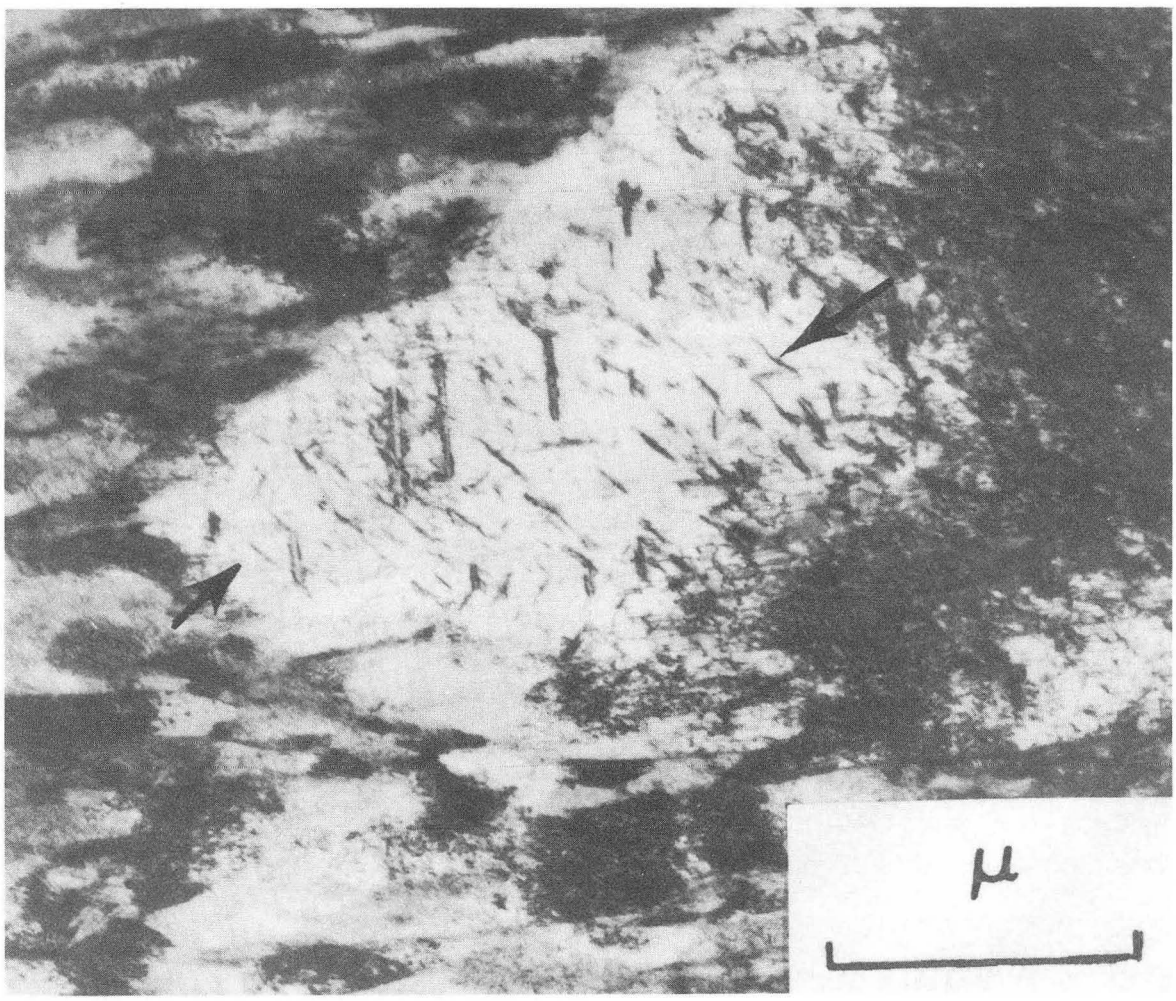

XBB 722-764

Fig. 19 Steel UC quenched and tempered at 200°C, bright field image showing the precipitation of cementite and ε-carbide (indicated by arrows).

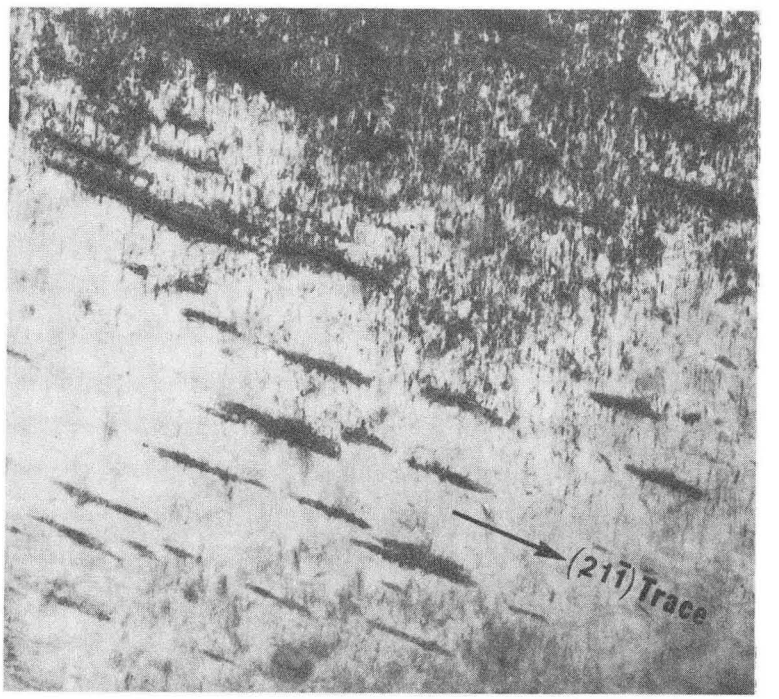

(A)

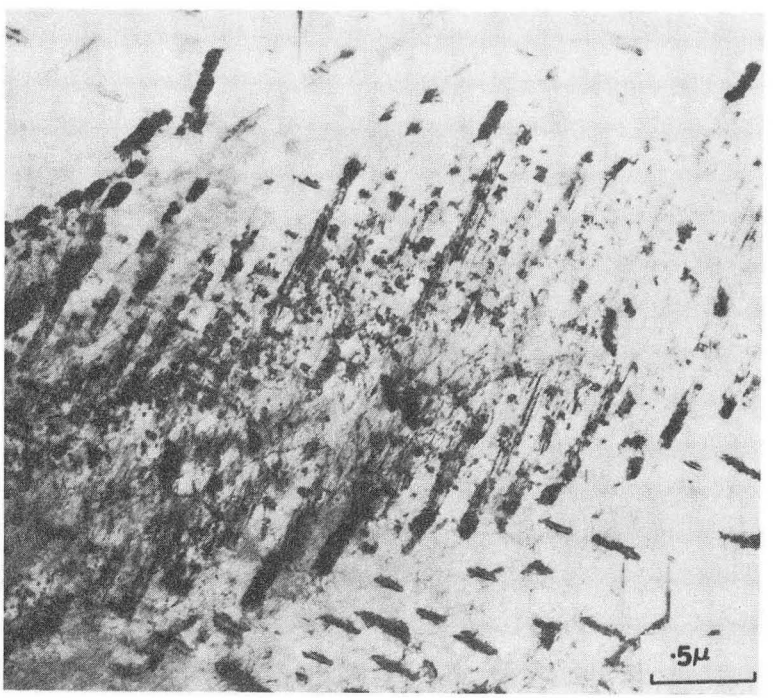

(B) XBB 722-761

Fig. 20 Steel TC quenched and tempered at 300°C, (A) bright field image showing carbide precipitation along the twins. The twins are not in contrast but trace analysis unambiguously revealed the traces to belong to $(21\bar{1})$ plane. (B) shows bright field micrograph indicating change in the precipitation mode at the twinned and twin-free regions of the plate.

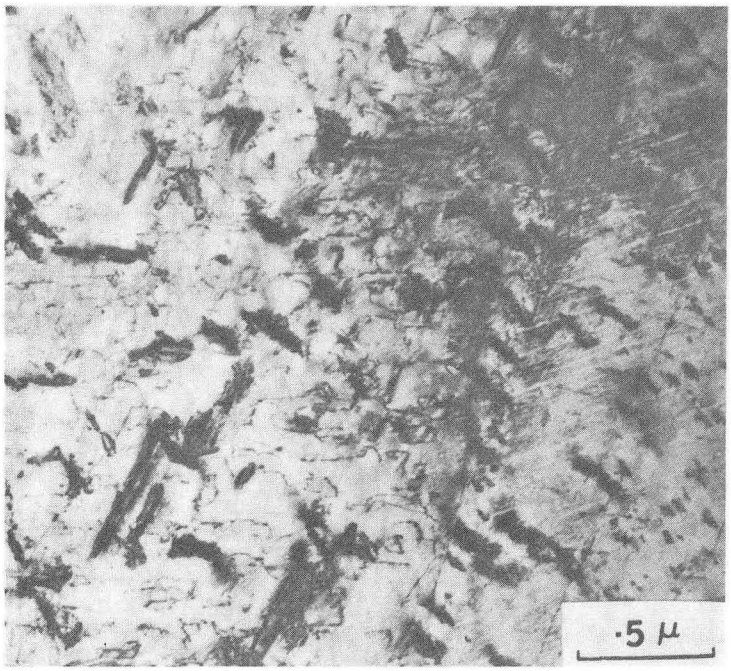

(A)

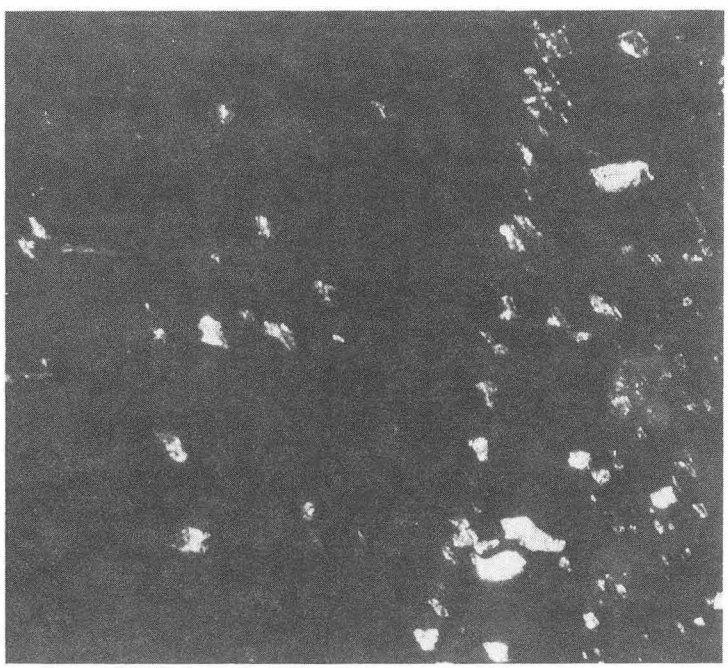

(B) XBB 722-753

Fig. 21 Steel TC quenched and tempered at 300°C. (A) Bright field image showing precipitation of carbides along plate and twin boundaries which reverse contrast in the dark field image(B).

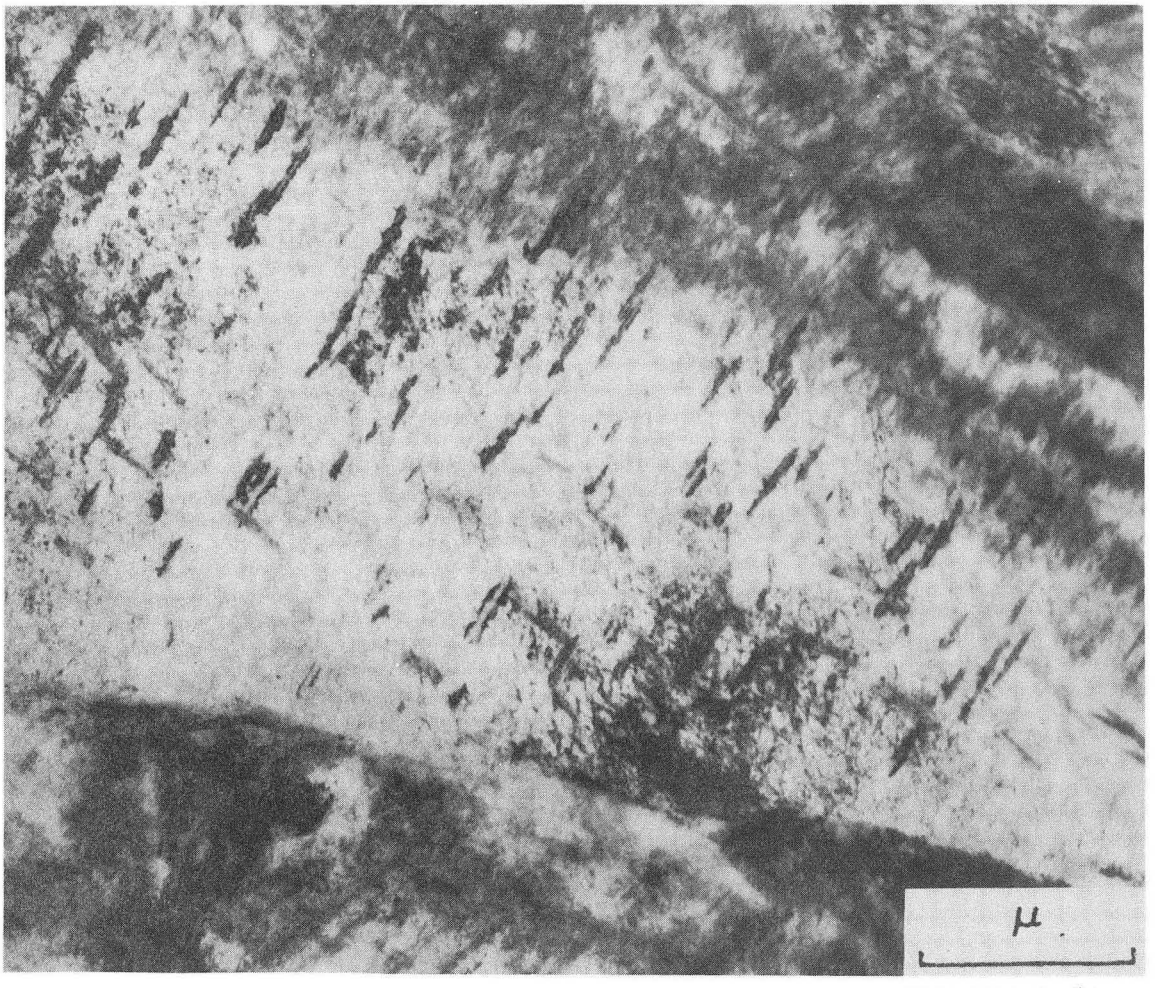

XBB 723-1265

Fig. 22 Steel UC, quenched and tempered at 300°C, bright field image showing Widmanstatten cementite precipitation.

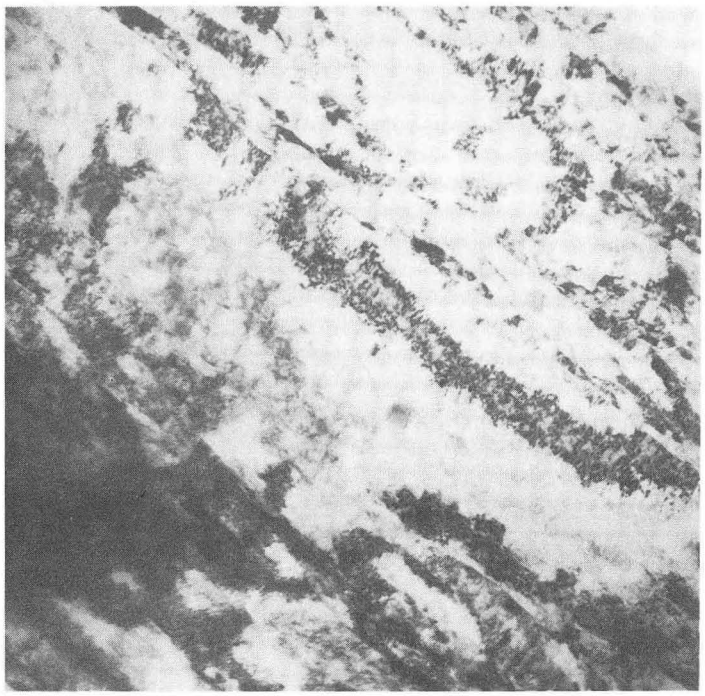

(A)

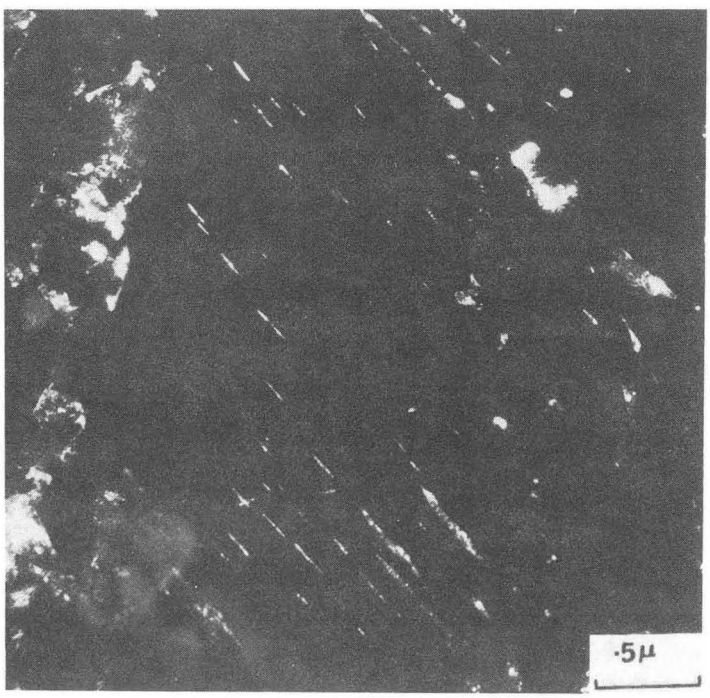

(B) XBB 722-760

Fig. 23 Steel UC quenched and tempered at 300°C, (A) bright field micrograph revealing no preferential precipitation of carbides along the lath boundaries while the dark field image (B) uniquely demonstrates preferential precipitation along the lath boundaries.

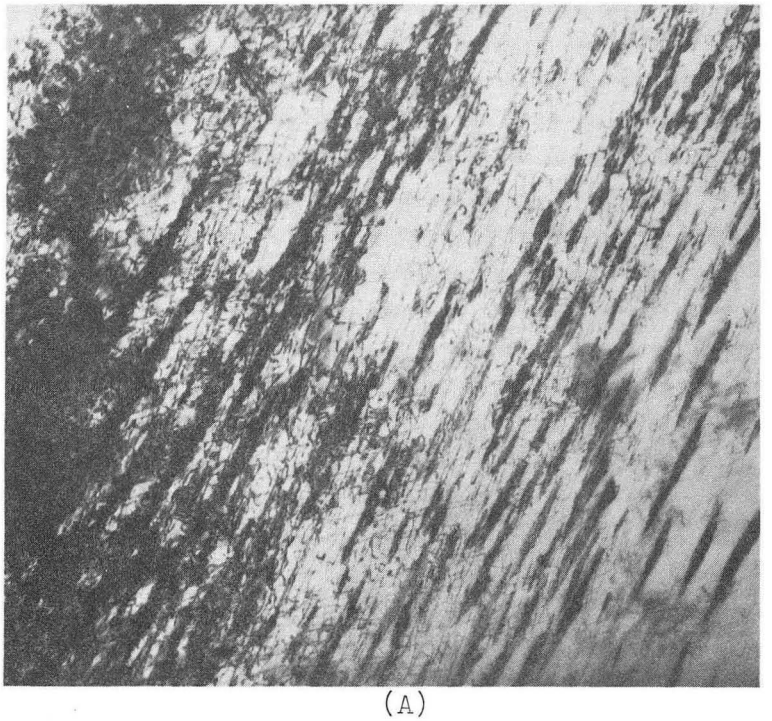

(A)

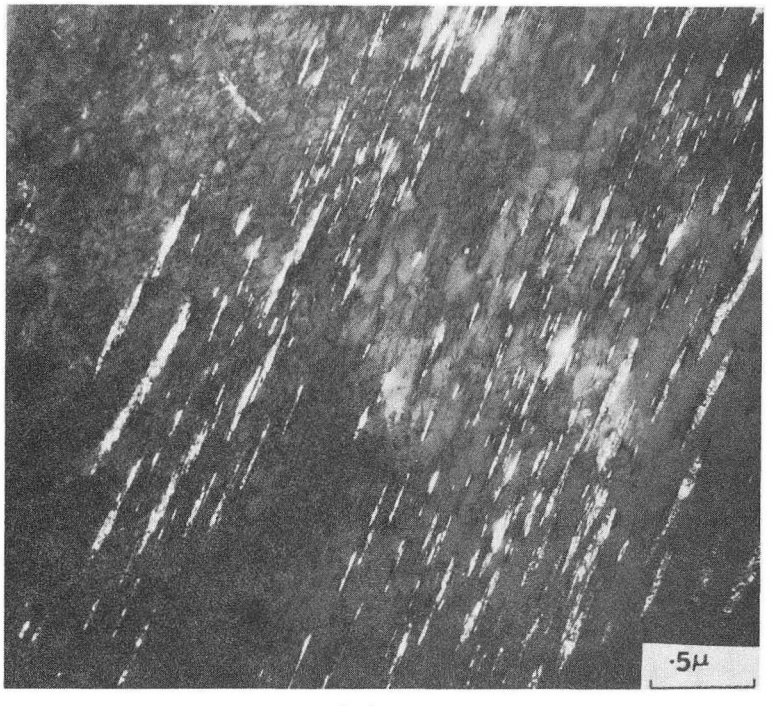

(B) XBB 722-759

Fig. 24 Steel TC quenched and tempered at 400°C, bright field image (A) showing extensive carbide precipitation at the twins which reverse contrast in the dark field image of a carbide reflection (B).

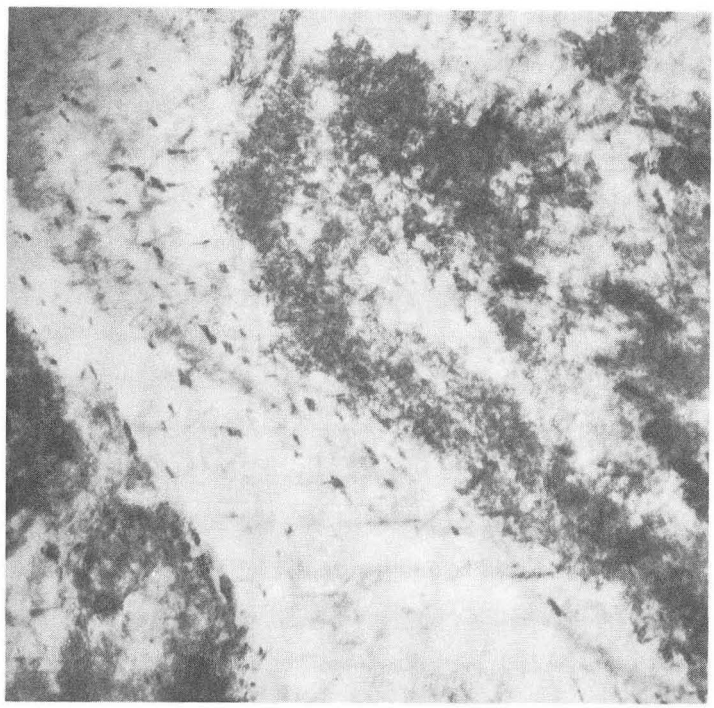

(A)

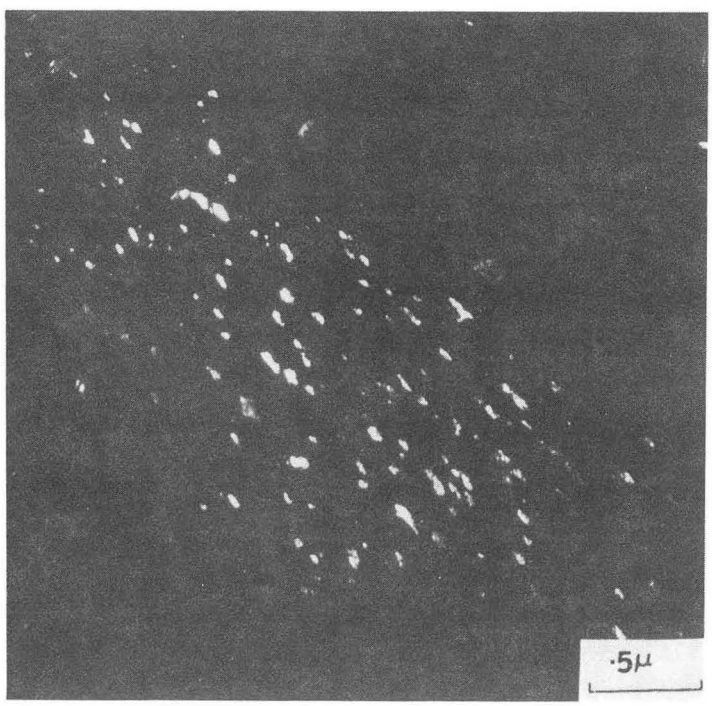

(B) XBB 722-756

Fig. 25 Steel UC quenched and tempered at 400°C, (A) bright field micrograph showing partially spherodised carbides in the martensite plate and dark field image of a carbide spot reverses contrast of the carbides in (B).

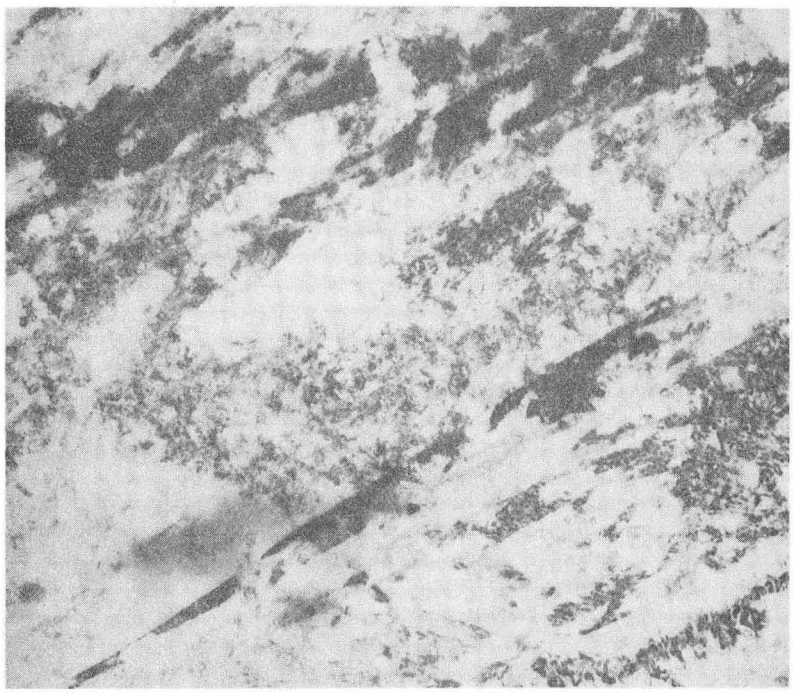

(A)

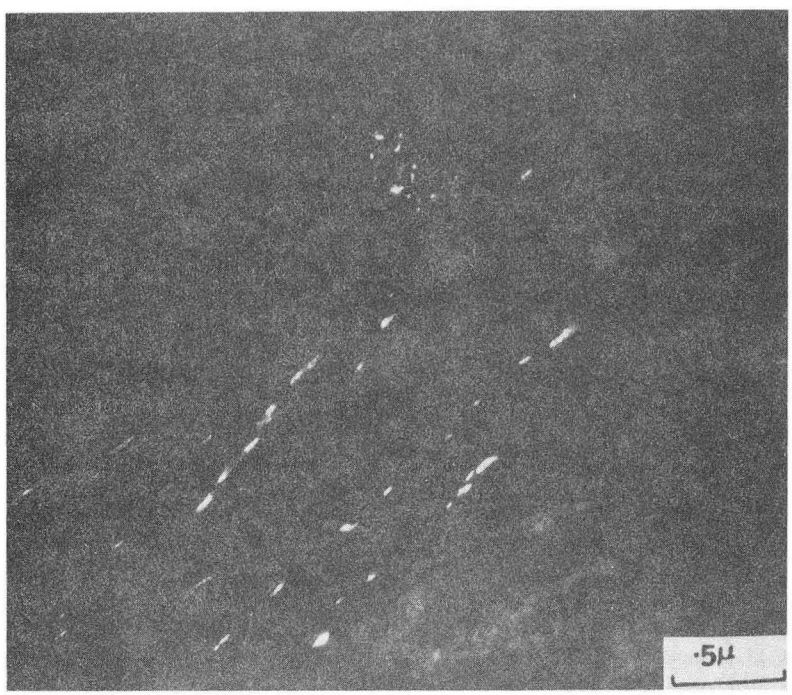

(B) XBB 722-758

Fig. 26 Steel UC quenched and tempered at 400°C, (A) bright field image indicating no preferential precipitation of carbides along the lath boundaries whereas the dark field image of a carbide reflection (B) shows adequate precipitation of carbides preferentially formed along the lath boundaries.

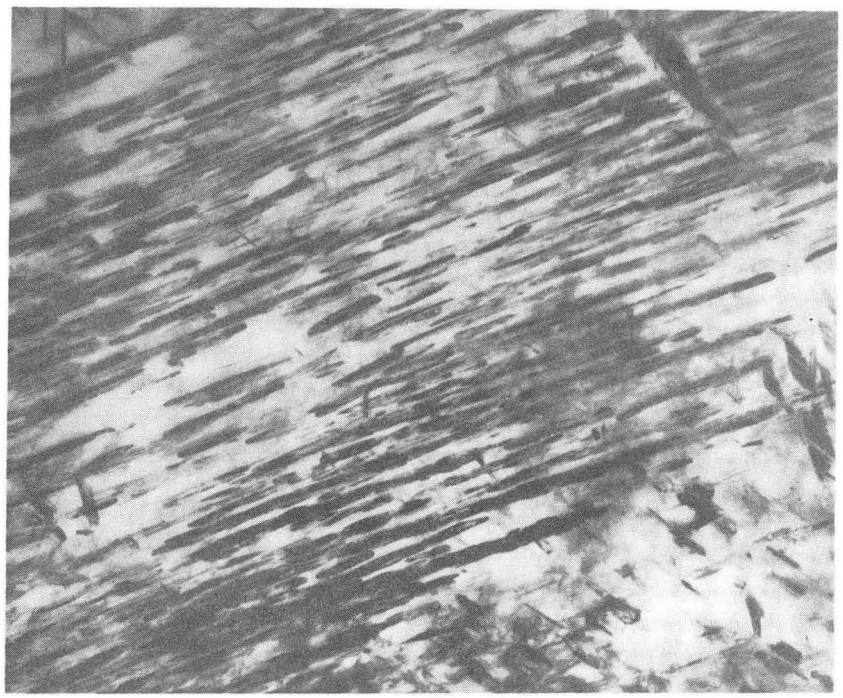

(A)

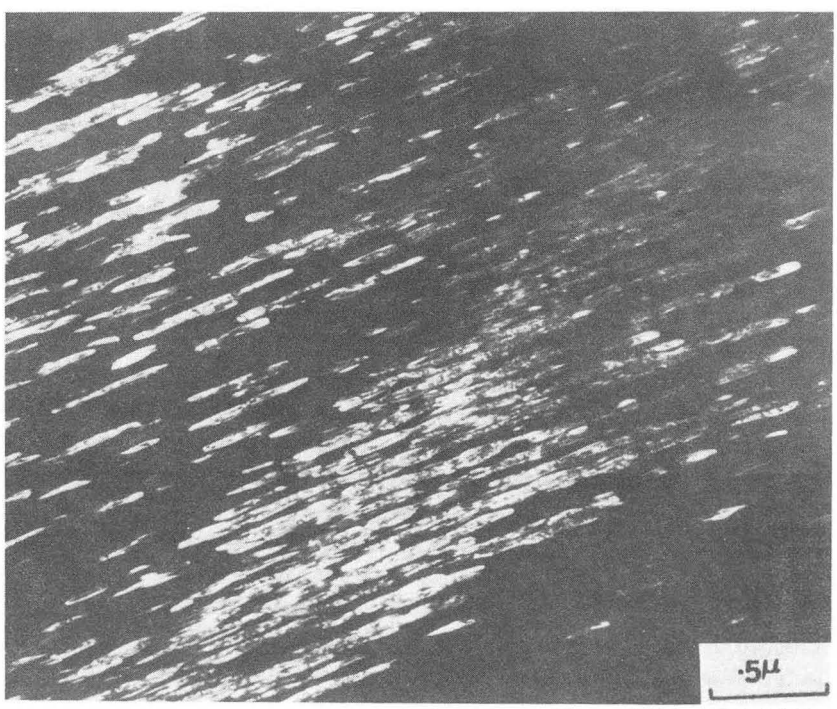

(B) XBB 722-757

Fig. 27 Steel TC quenched and tempered at 500°C, showing almost continuous precipitation of carbides along the twins in the bright field image (A) and a dark field image of a carbide reflection (B) reverses the contrast of these twin boundary carbides.

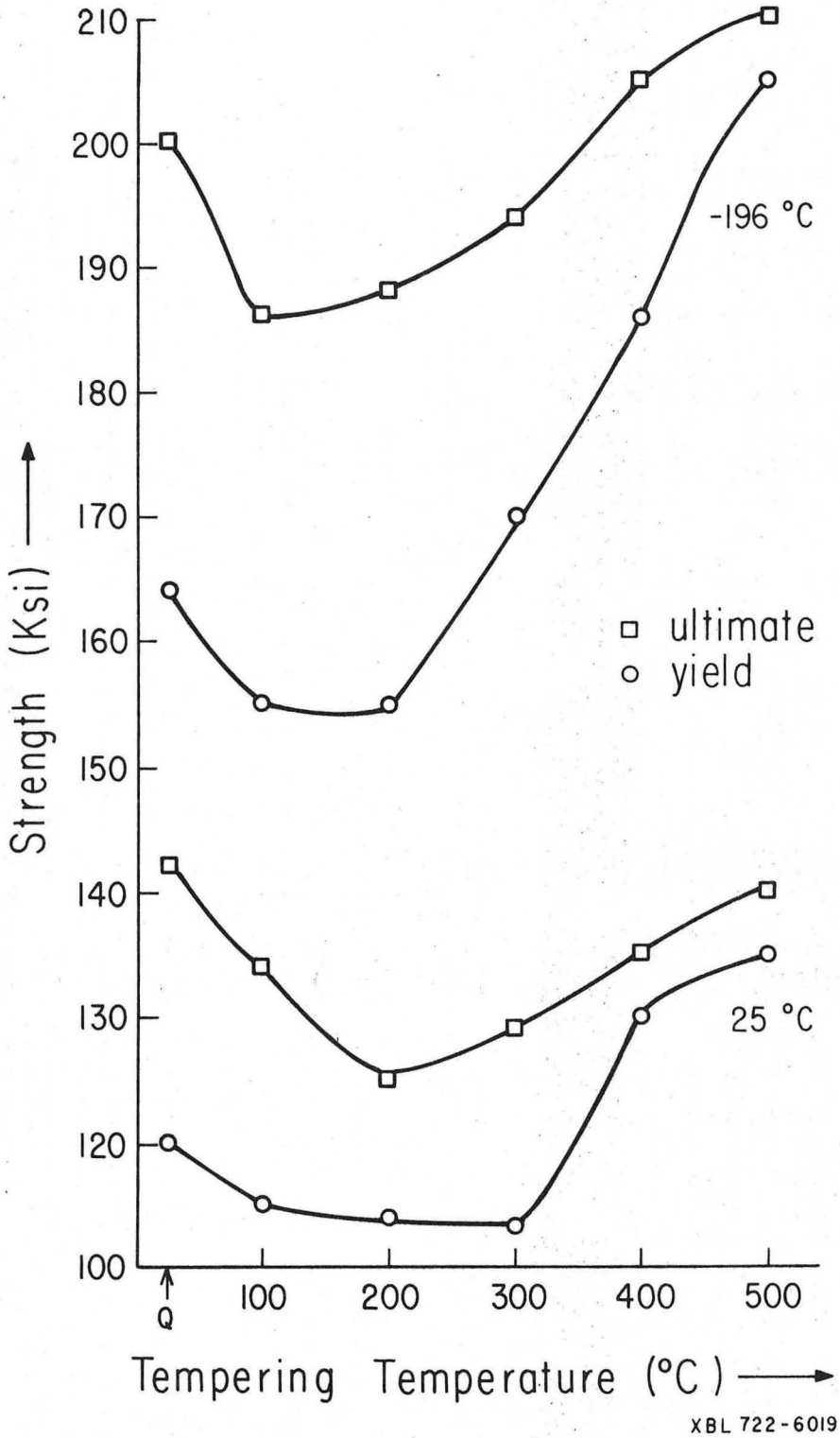

Fig. 28 Effect of tempering on the strength of steel TC at -196°C and 25°C.

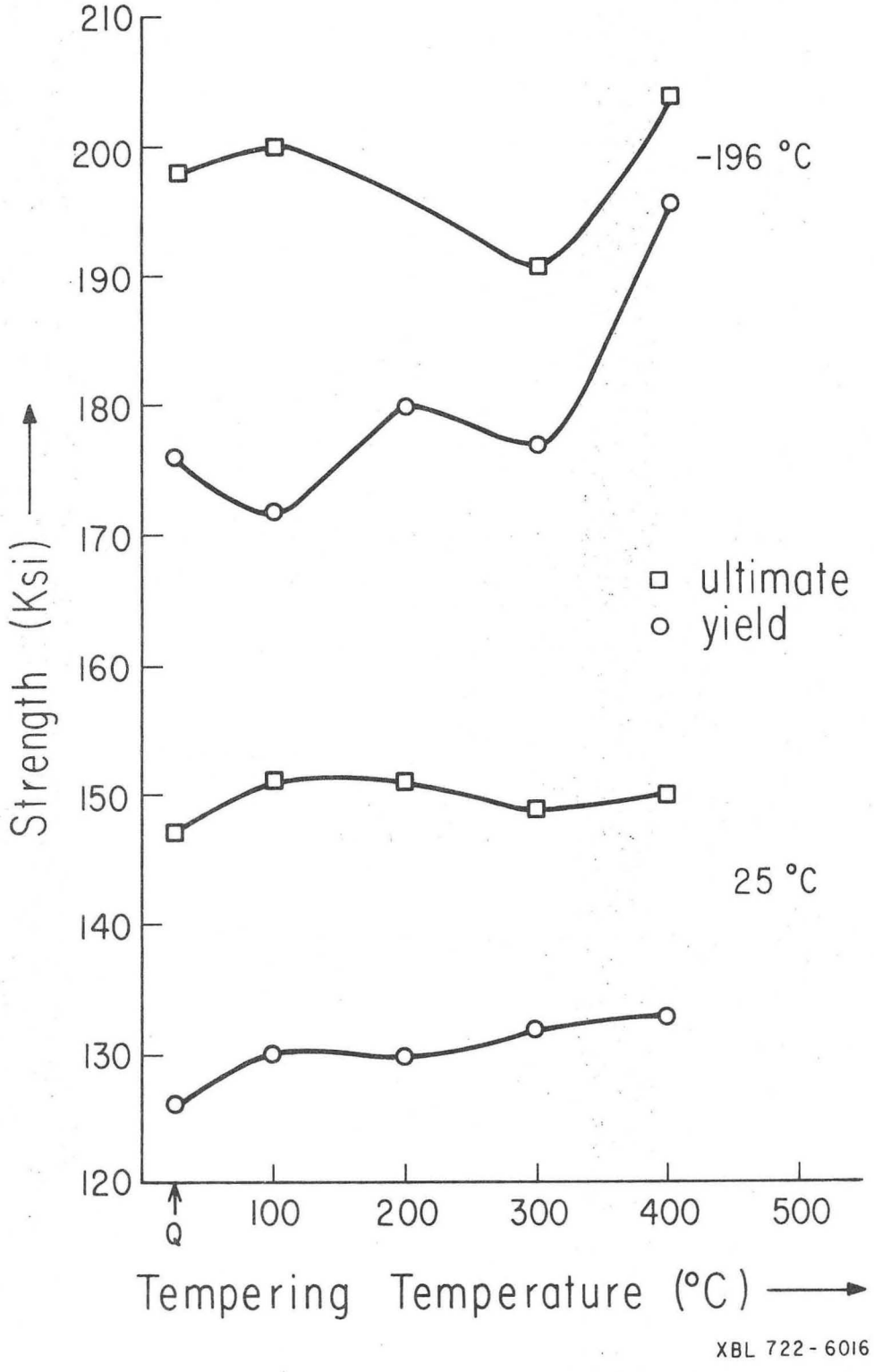

Fig. 29 Effect of tempering on the strength of steel UC at -196°C and 25°C.

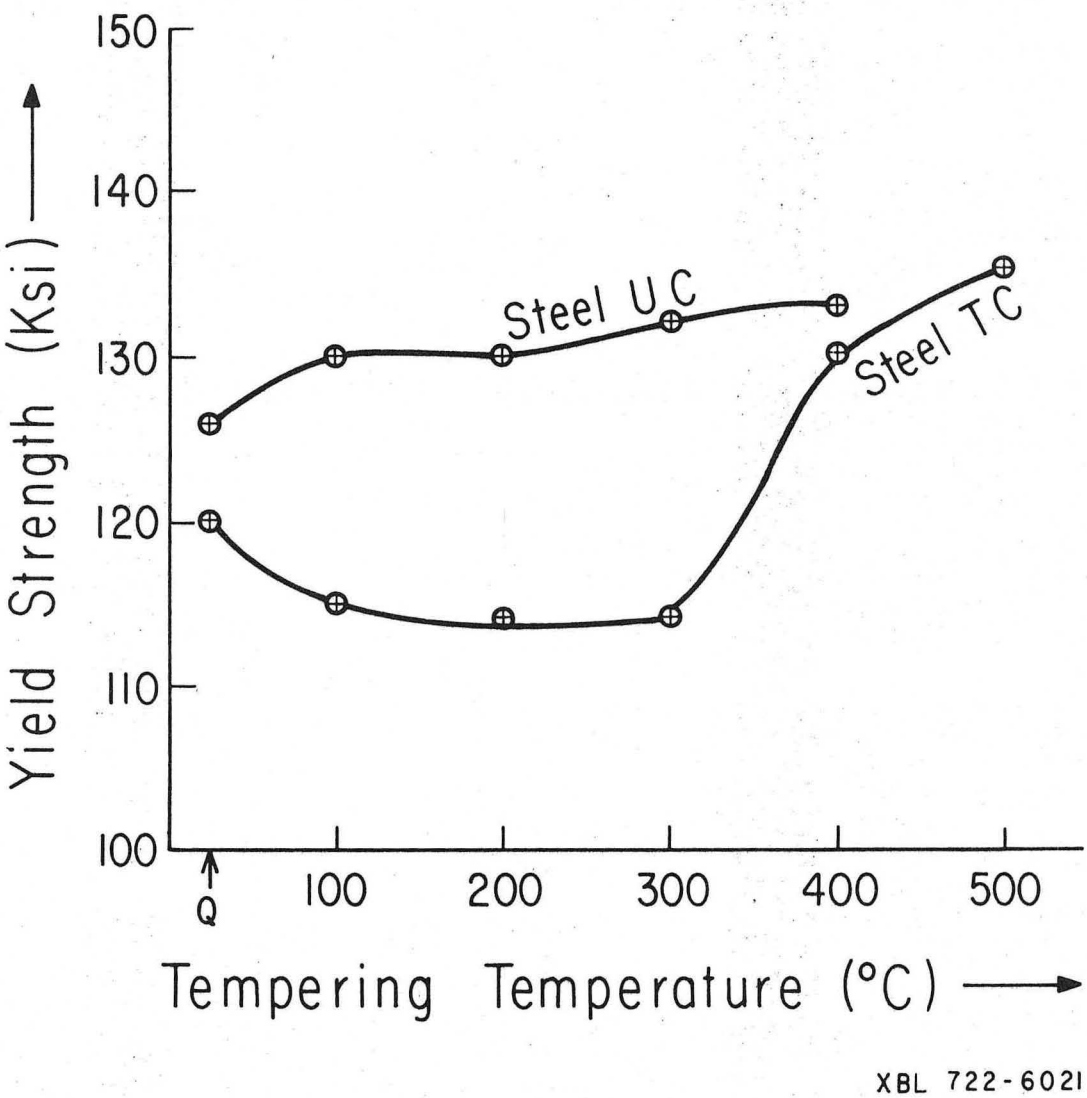

Fig. 30 Effect of tempering on the yield strength of steels TC and UC at 25°C.

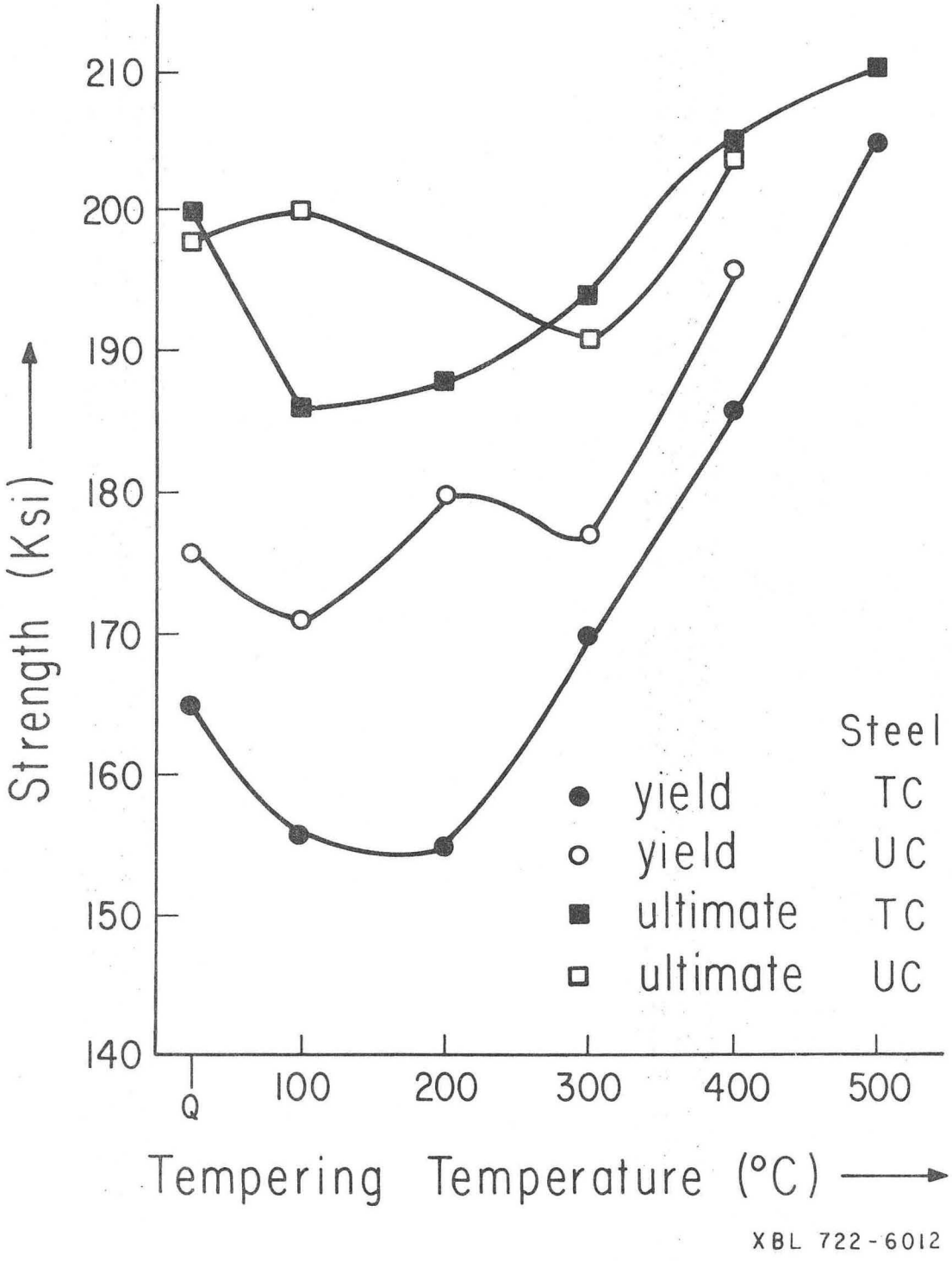

Fig. 31 Effect of tempering on the strength of steels TC and UC at -196°C

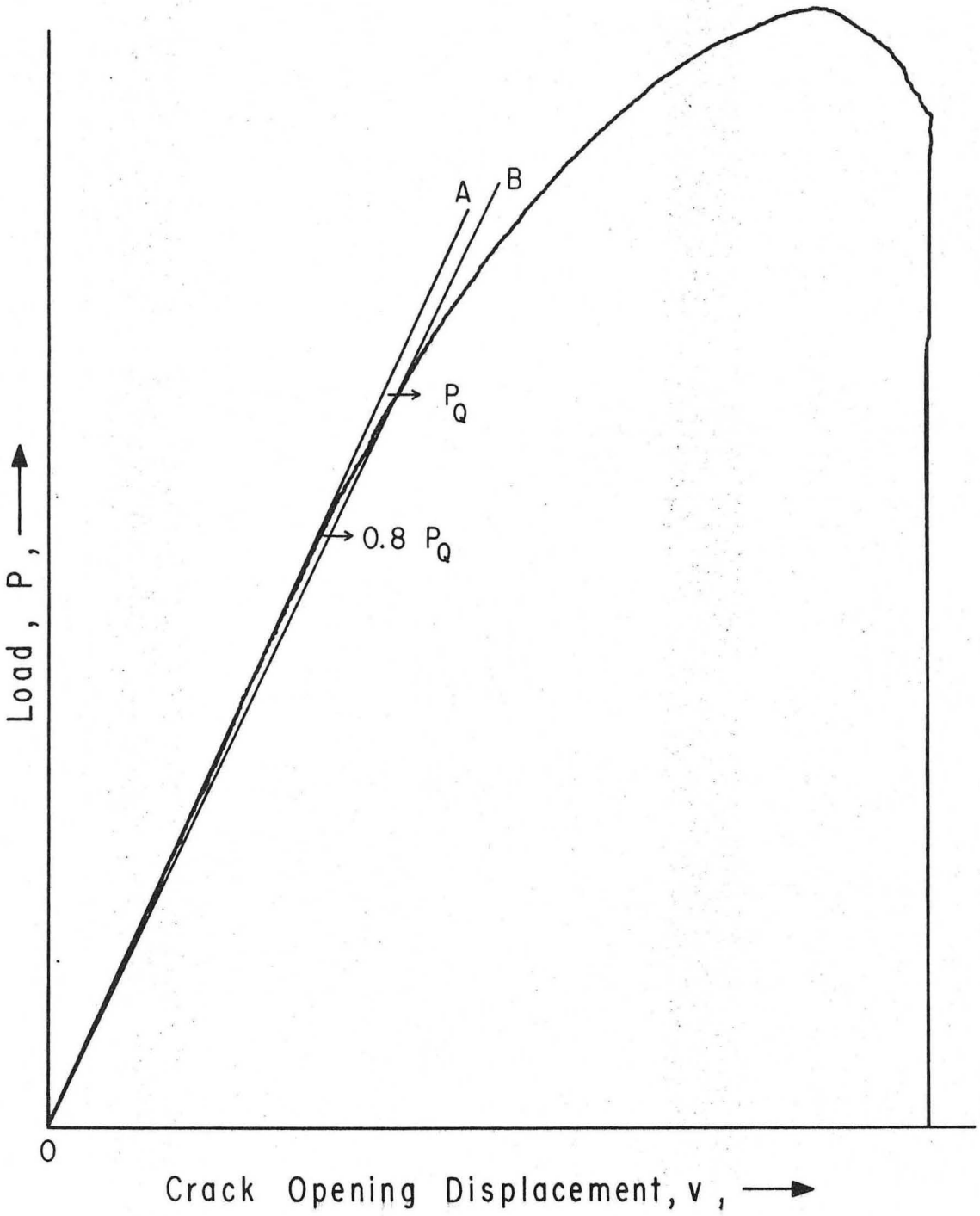

XBL 722- 6028

Fig. 32A Load vs. COD curve obtained during the fracture toughness test of the carbonless alloys. The tangent line OA and secant line OB along with the apparent critical load P_Q and $0.8P_Q$ are indicated. The test is an invalid plane strain fracture toughness test.

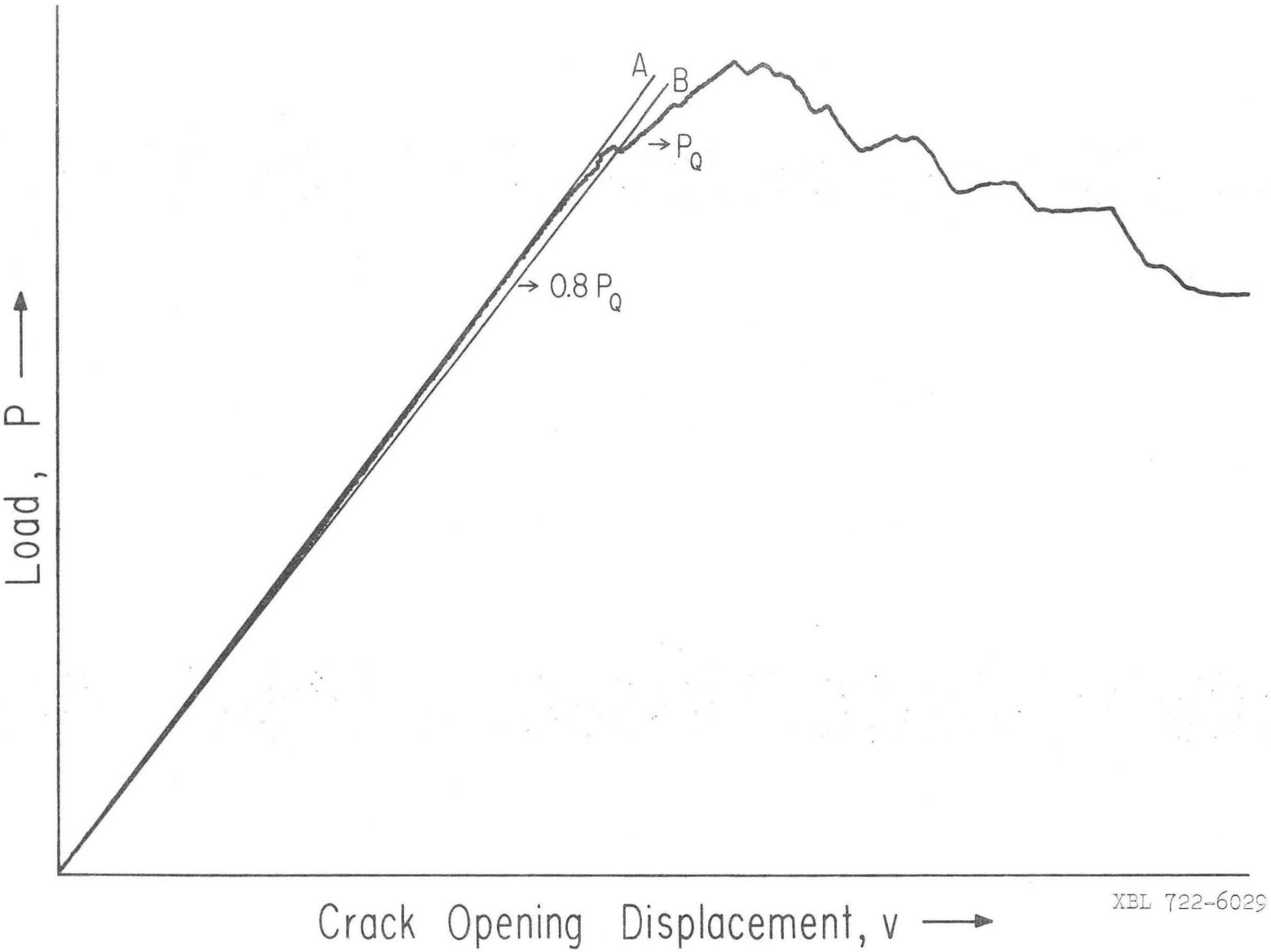

Fig. 32B Load vs. COD curve obtained during the fracture toughness test of the carbon steels. The tangent line OA and the secant line OB along with the critical load P_Q and $0.8P_Q$ are indicated. The curve shows some slow crack growth before the "pop-in" and is a valid plane strain fracture toughness test.

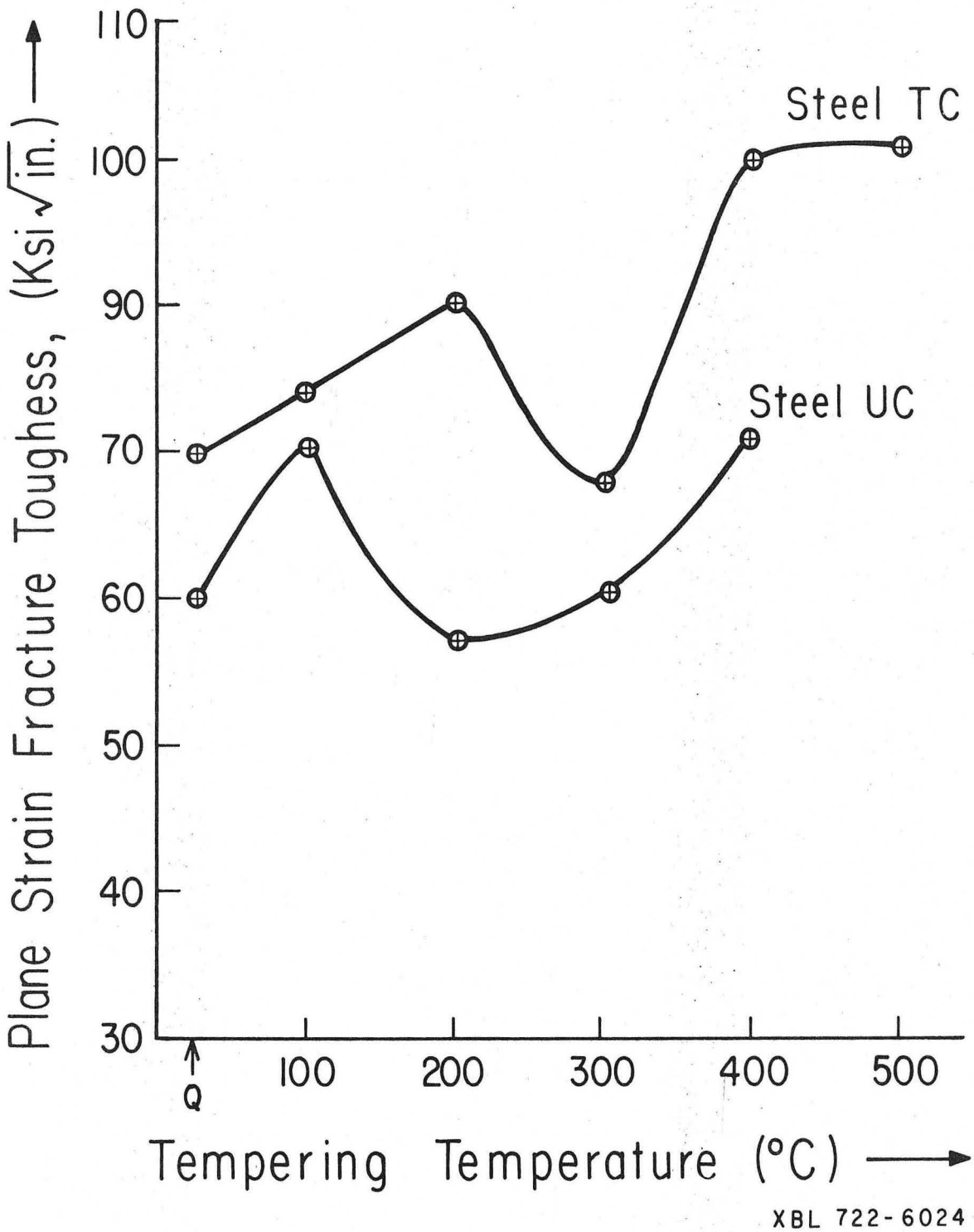

Fig. 33 Effect of tempering on the plane strain fracture toughness value of steels TC and UC.

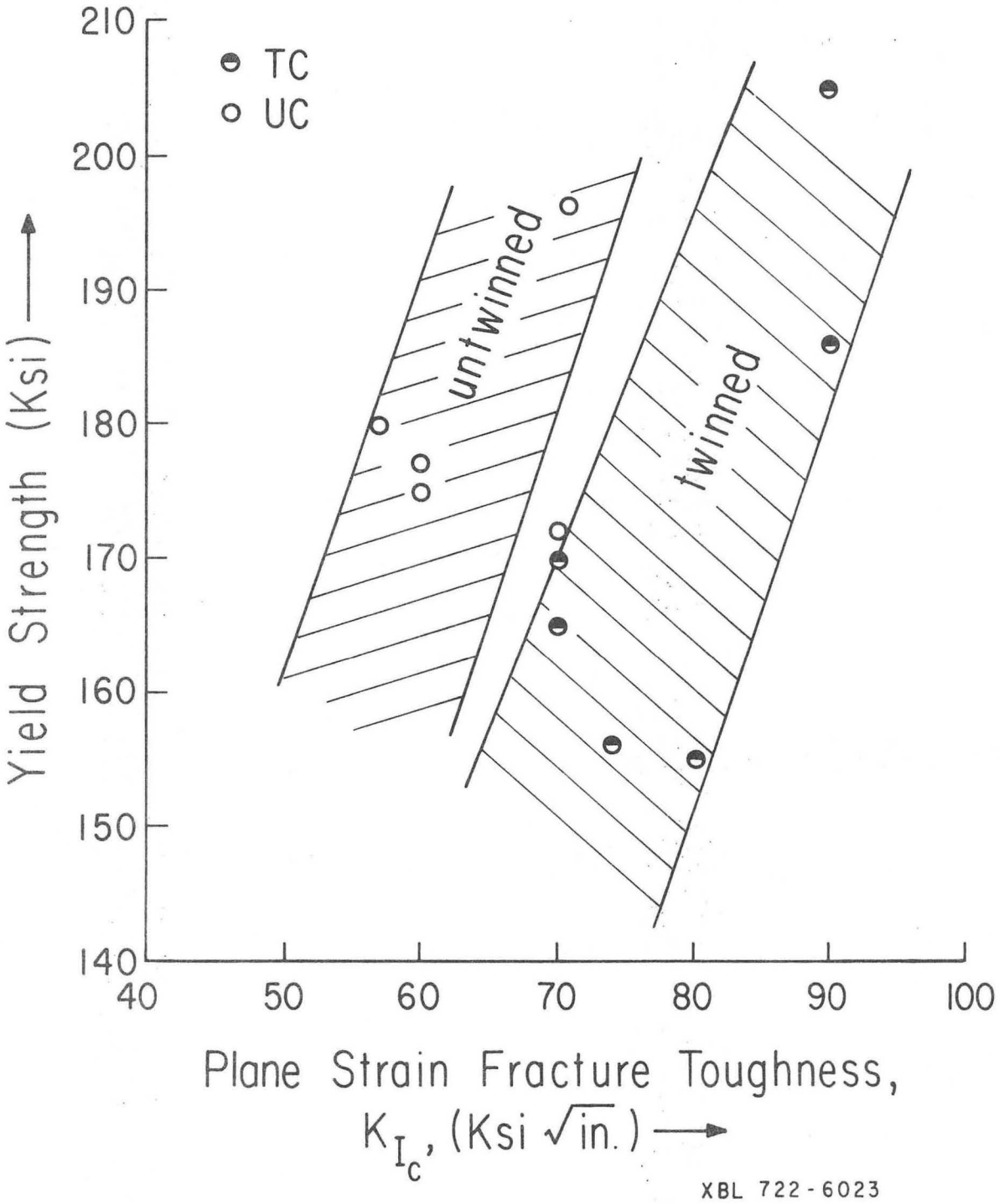

Fig. 34 Yield strength vs. fracture toughness plots of all the heat treatments of steels TC and UC.

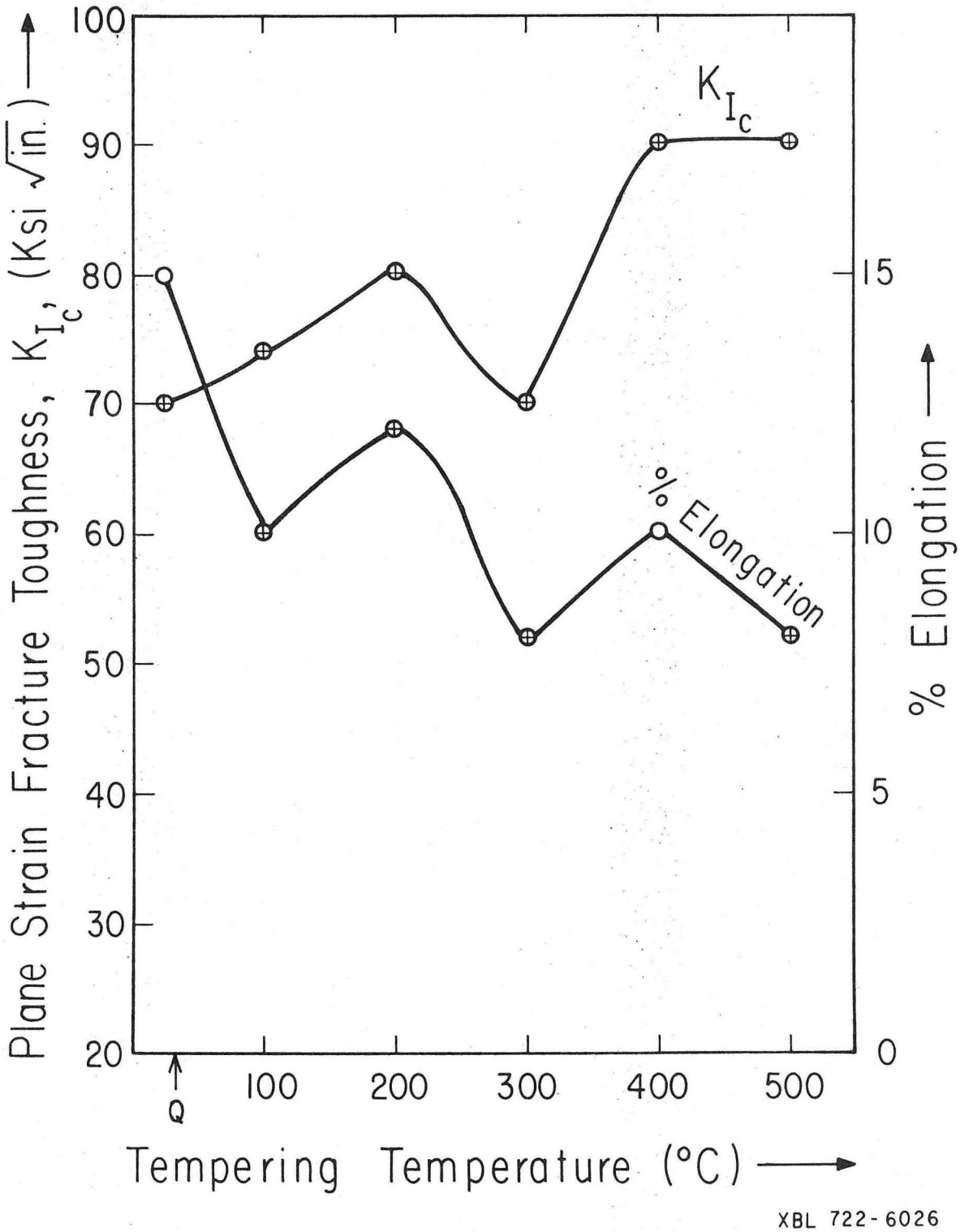

Fig. 35 Variation of fracture toughness values and % elongation of steel TC with Tempering.

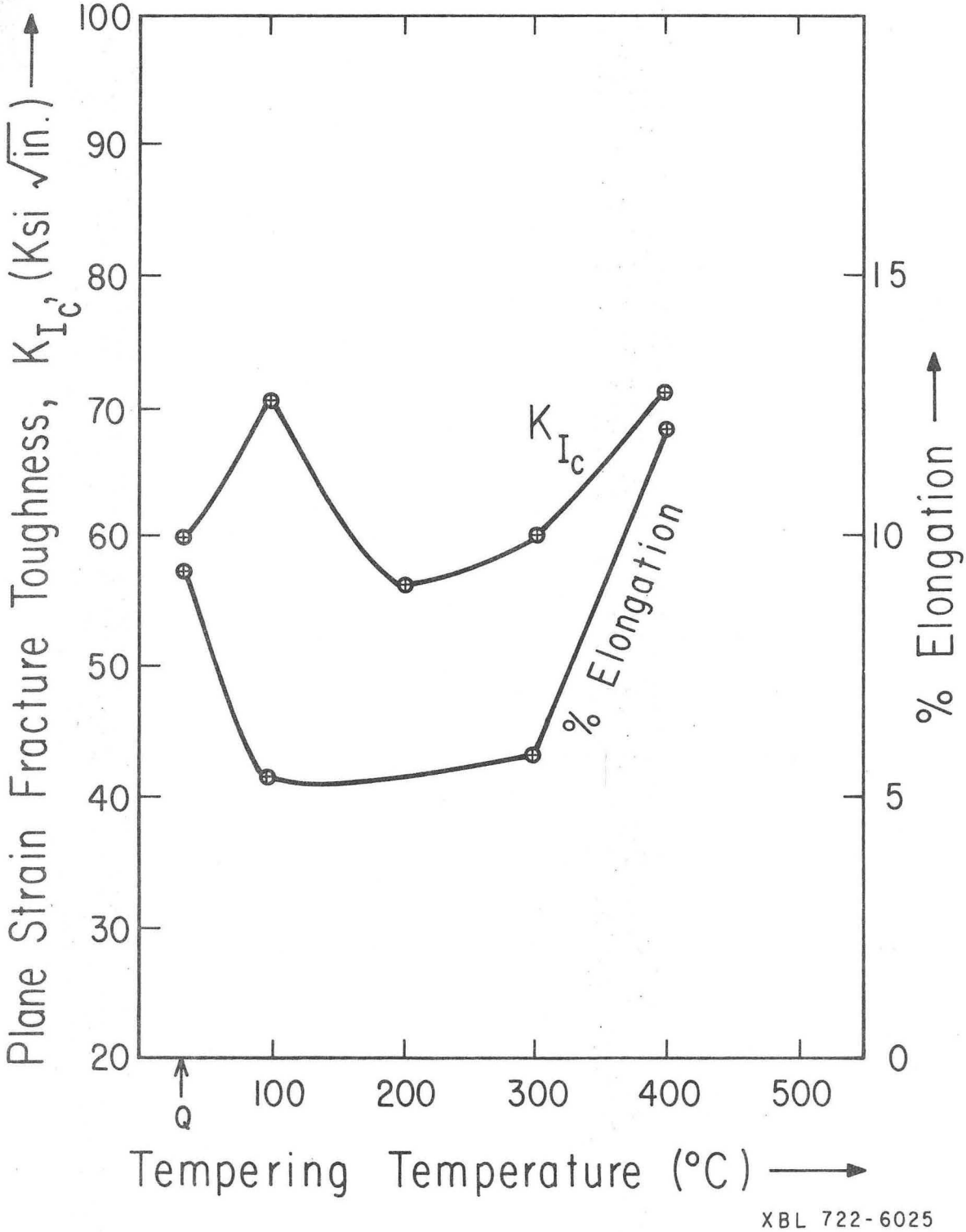

Fig. 36 Variation of fracture toughness values and % elongation of steels UC with tempering.

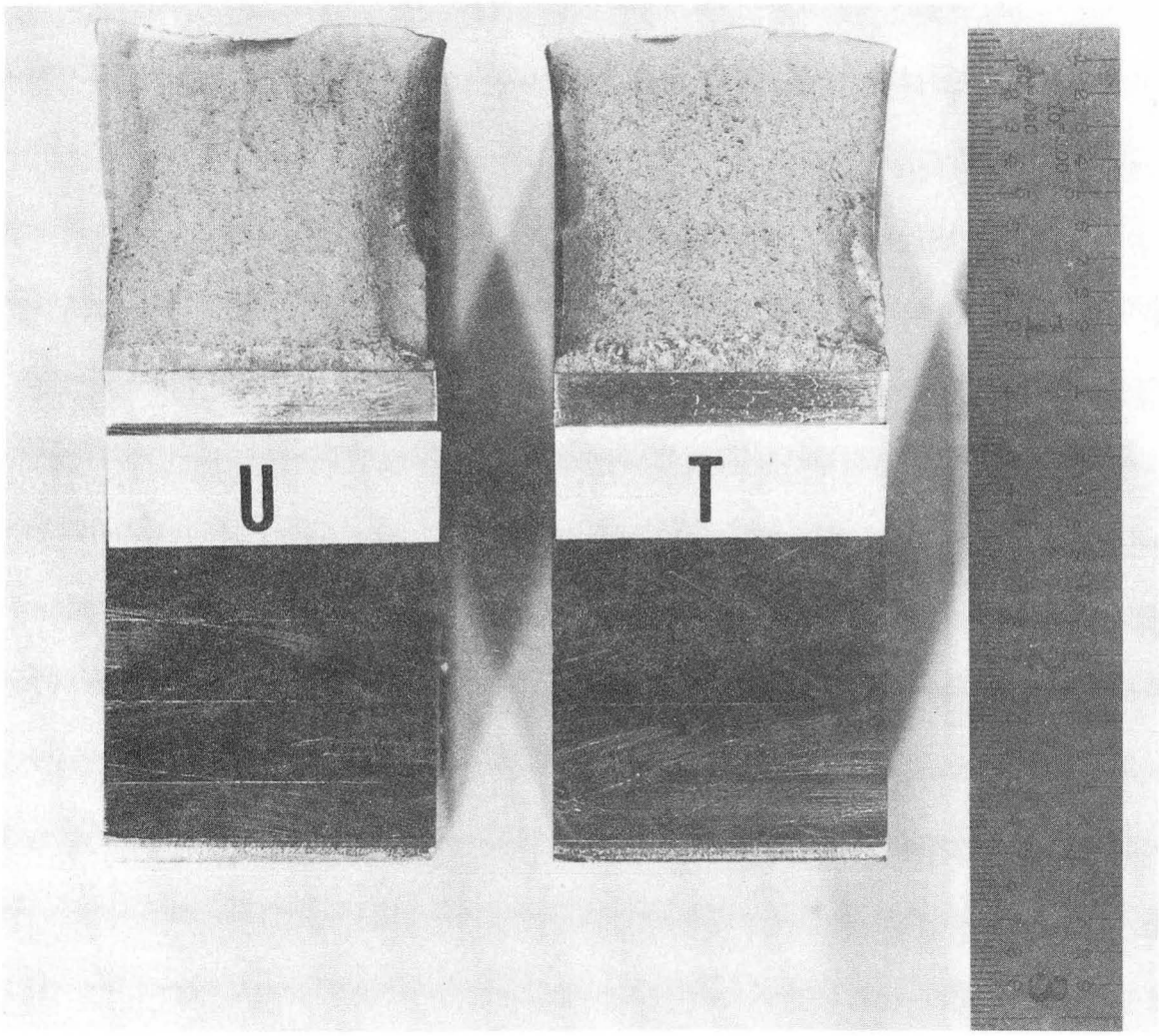

XBB 721-380

Fig. 37 Optical macrofractograph of the fracture specimens of alloys T and U.

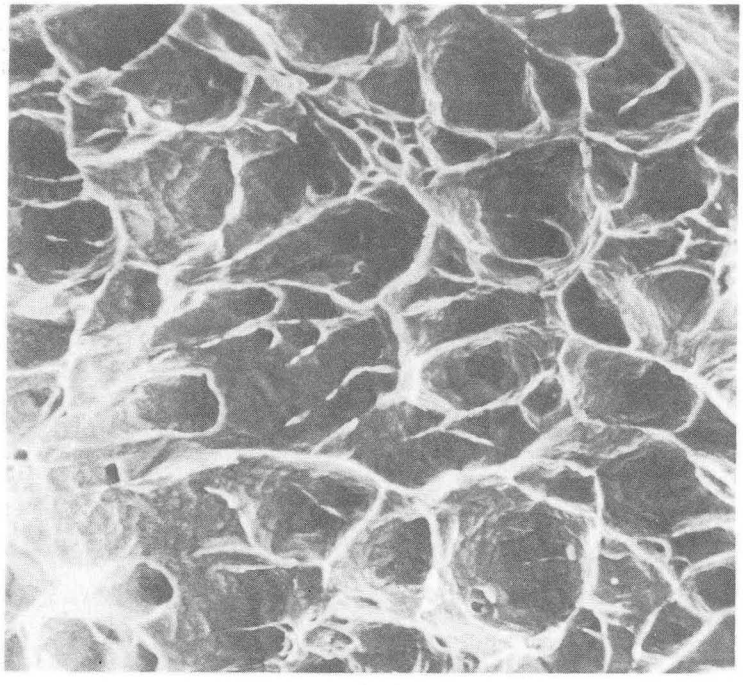

(A)

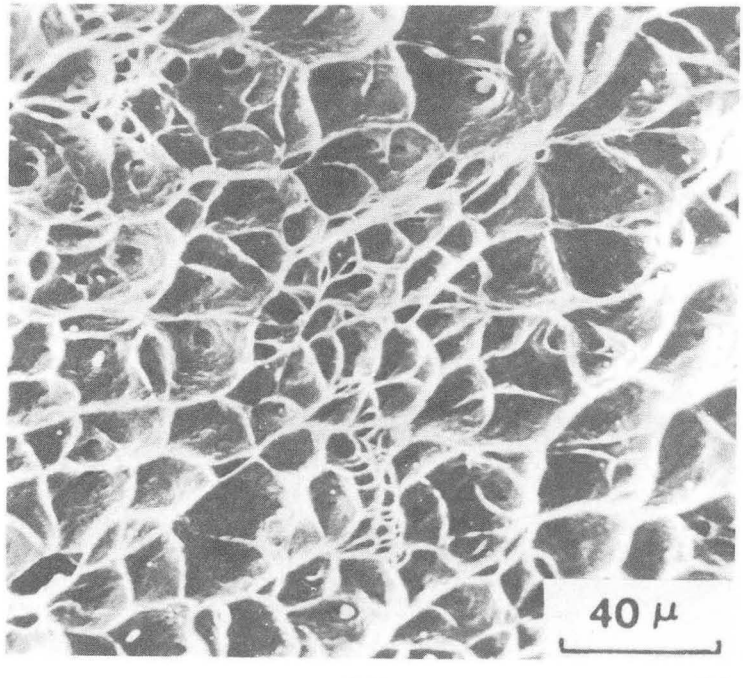

(B) XBB 721-386

Fig. 38 Scanning fractographs of the fracture specimens of alloys (A) T and (B) U.

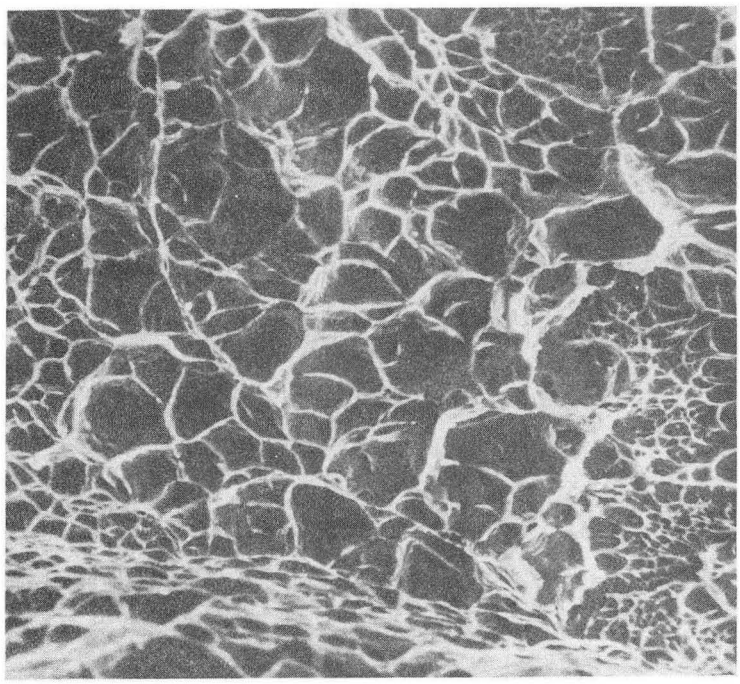

(A)

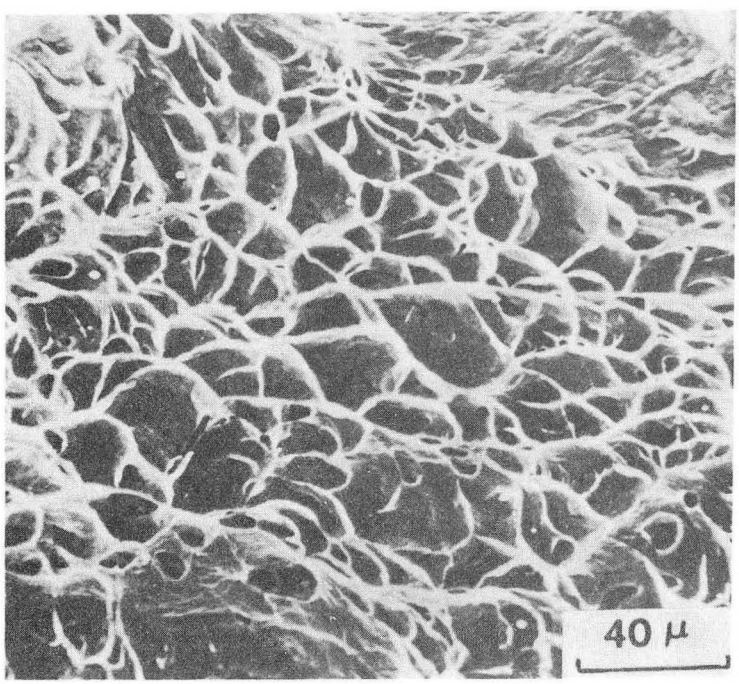

(B) XBB 721-388

Fig. 39 Scanning fractographs of the Charpy impact specimens of alloys (A) T and (B) U.

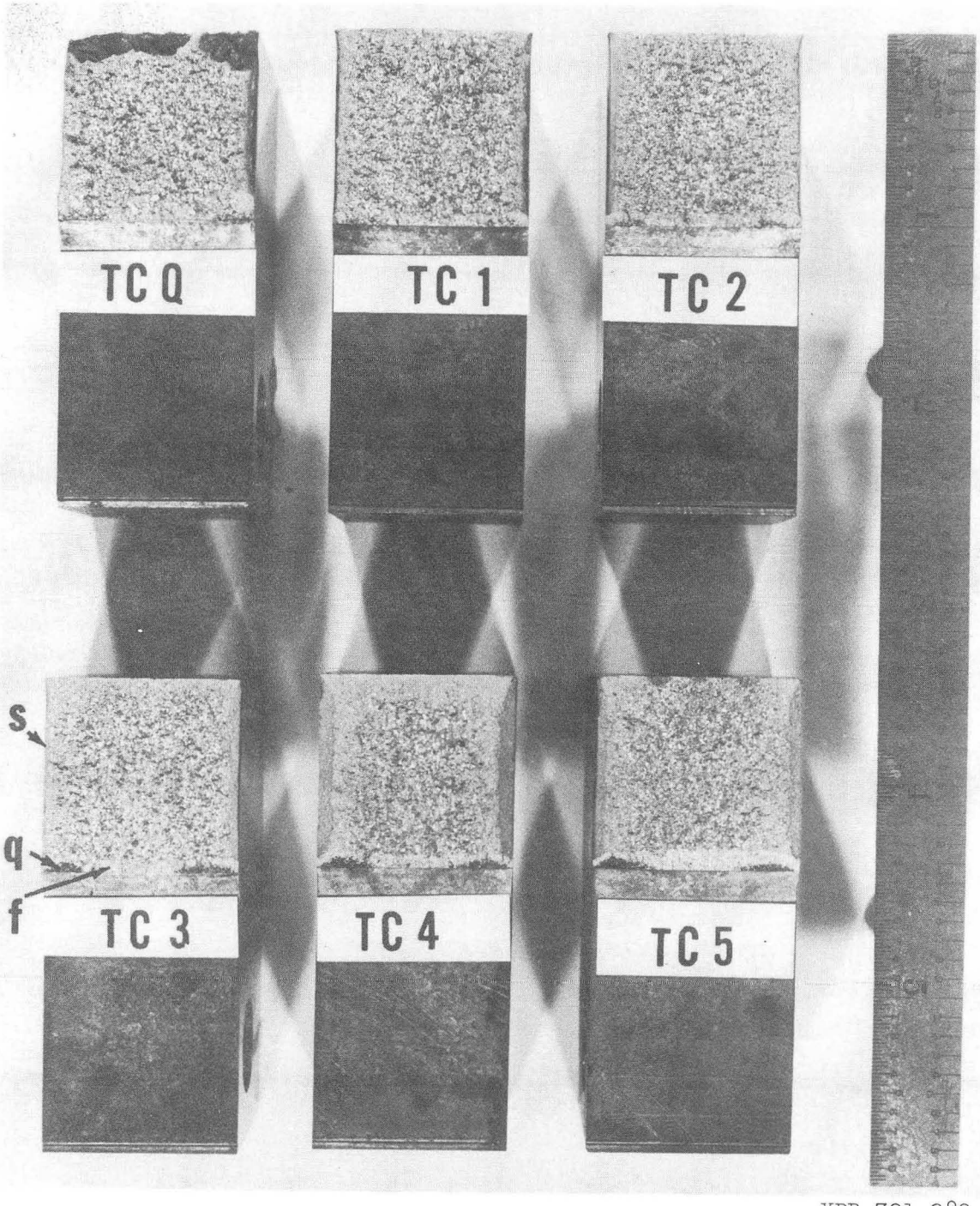

XBB 721-382

Fig. 40 Optical macrofractograph of the fracture specimens of steel TC. The shear lip (s), quench-crack (q) and the fatigue crack (f) are indicated.

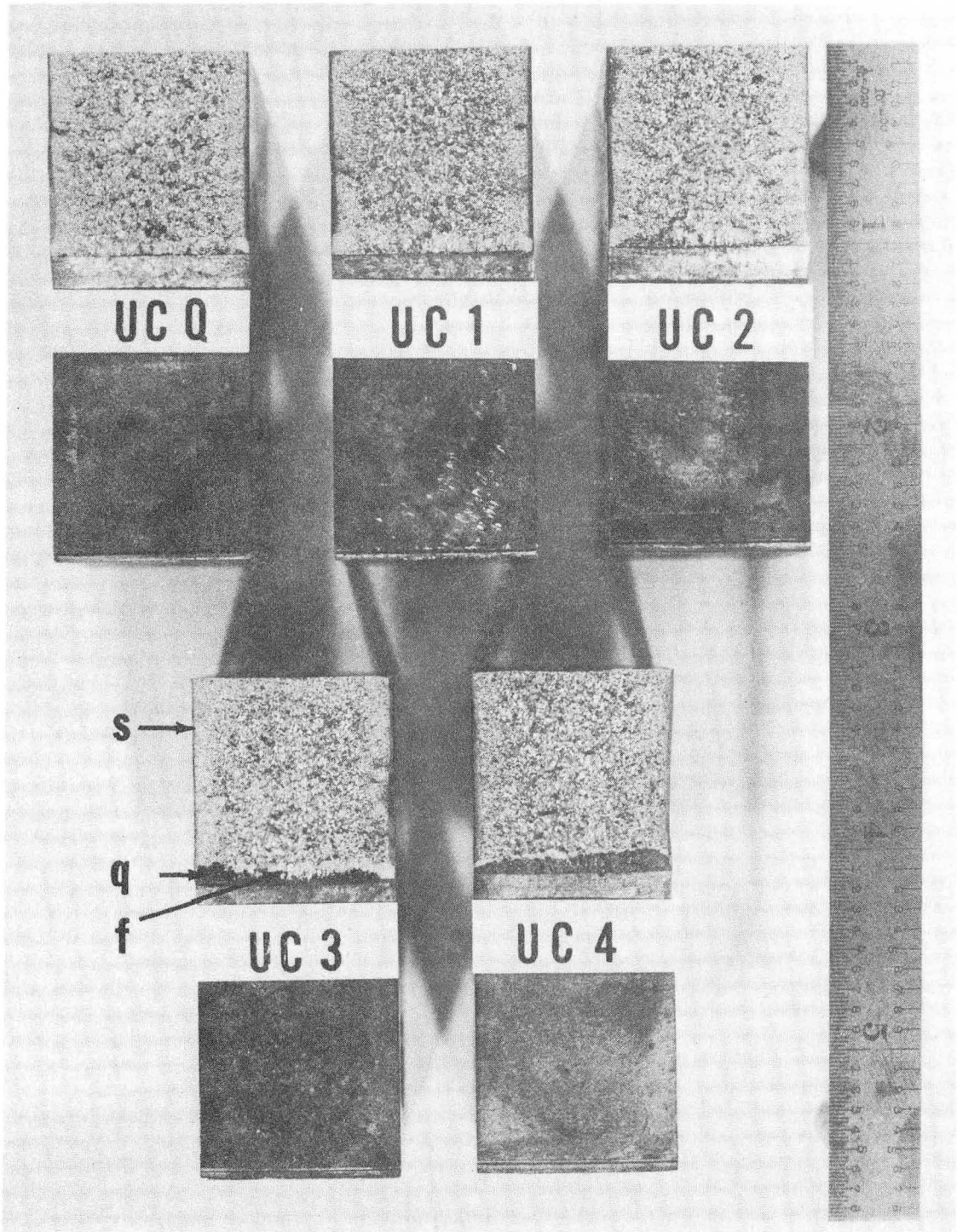

XBB 721-381

Fig. 41 Optical macrofractograph of the fracture specimens of steel UC. The shear lip (s), quench-crack (q) and fatigue crack (f) are indicated.

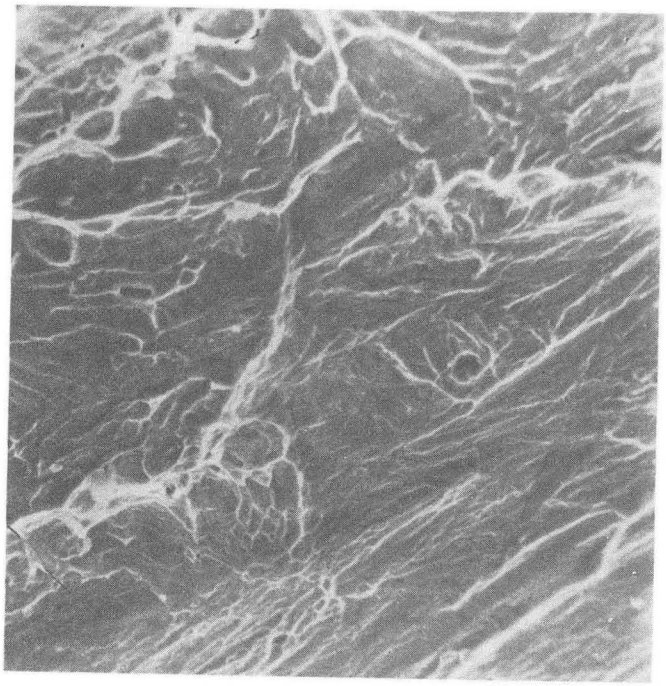

(A)

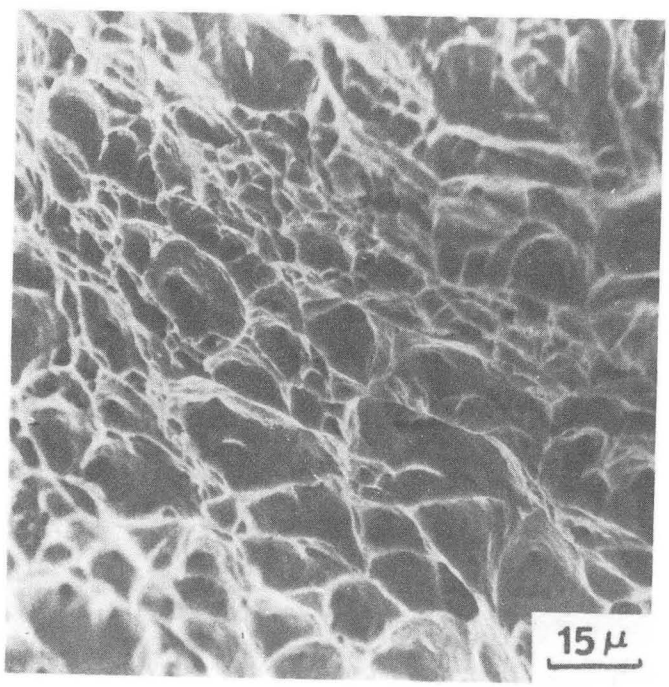

(B) XBB 721-385

Fig. 42 Fractographs of the fracture specimens of steel TC as-quenched showing (A) quasi-cleavage and (B) dimpled rupture.

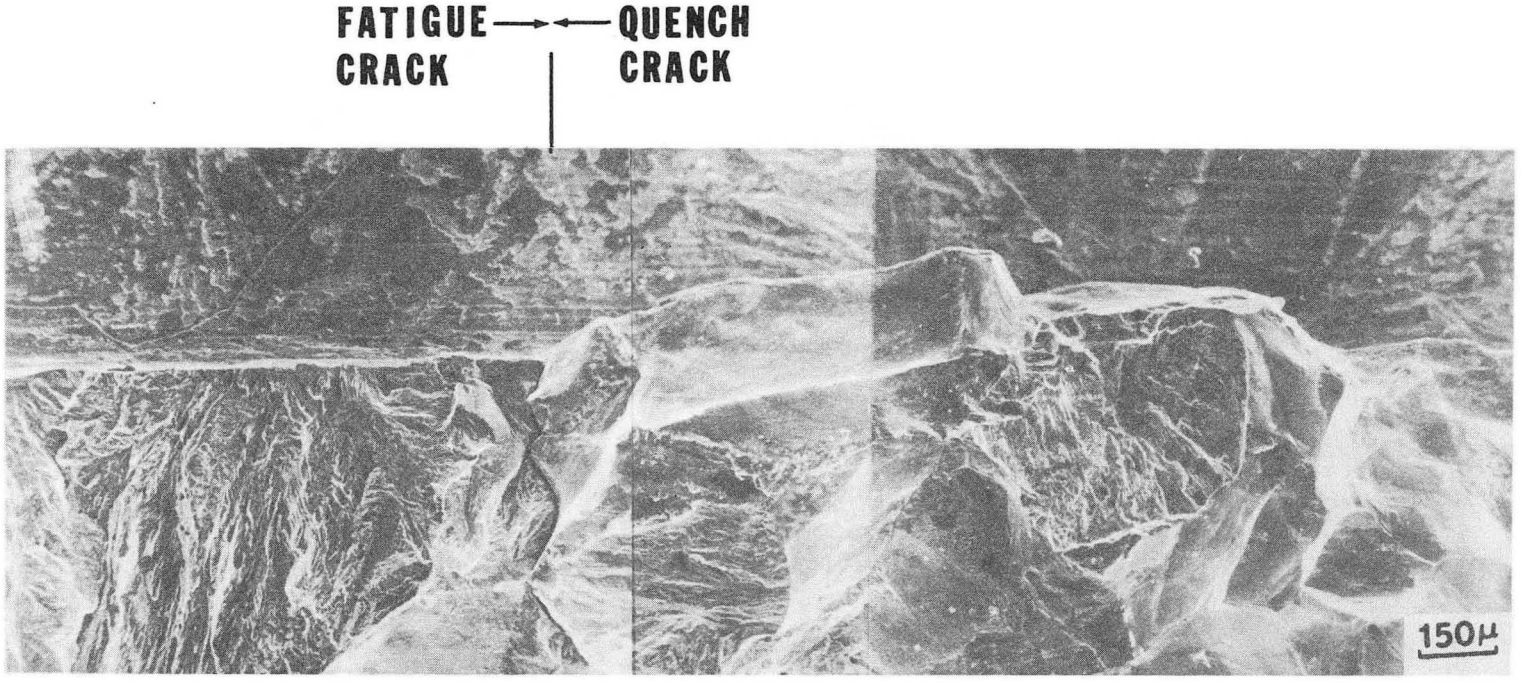

XBB 721-390

Fig. 43 Scanning fractograph of the notch tip of the fracture specimen of steel TC showing the presence of quench crack besides the fatigue crack.

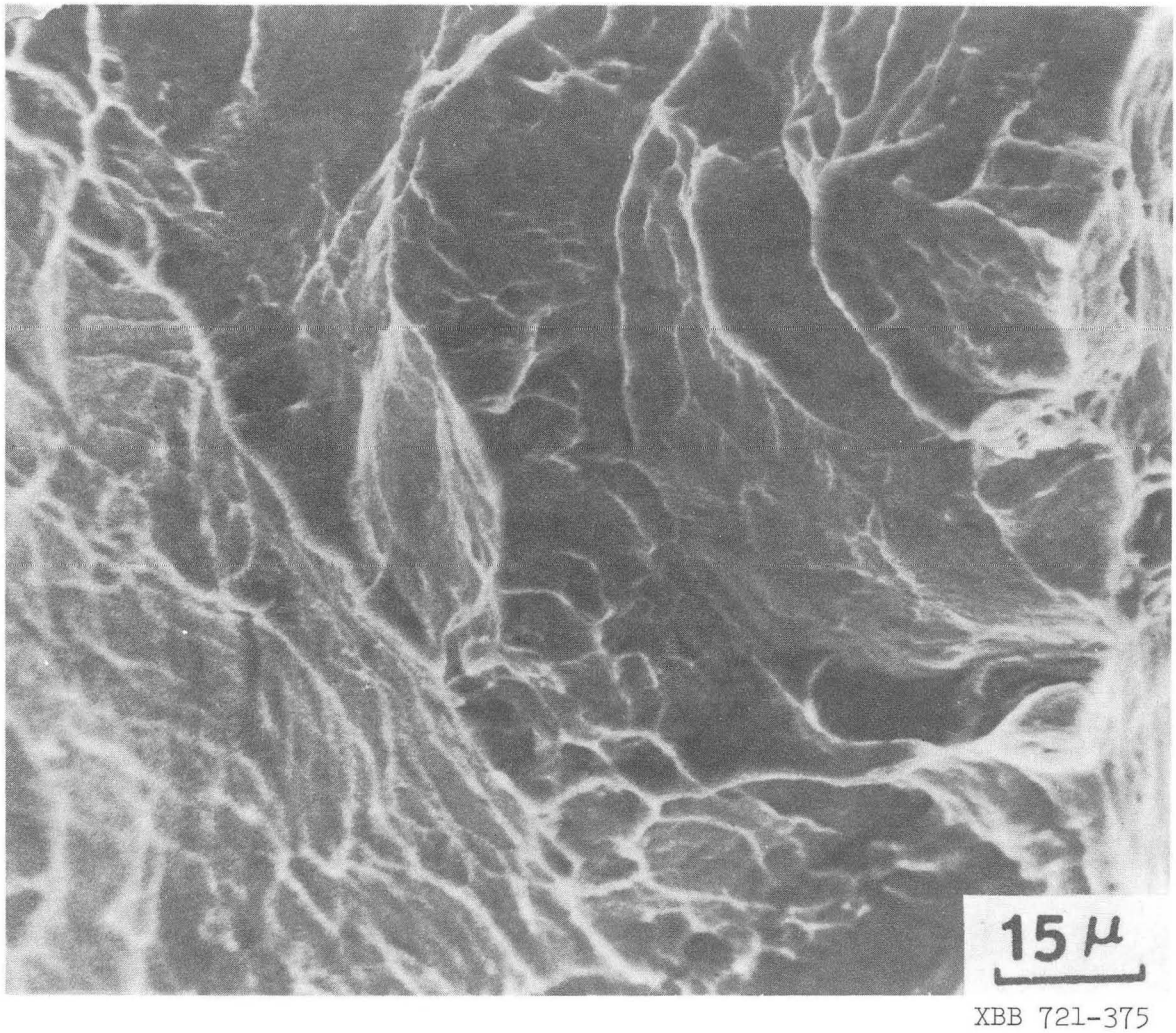

XBB 721-375

Fig. 44 Fractograph of steel TC quenched and tempered at 100°C indicating a mixture of quasi-cleavage and dimpled rupture.

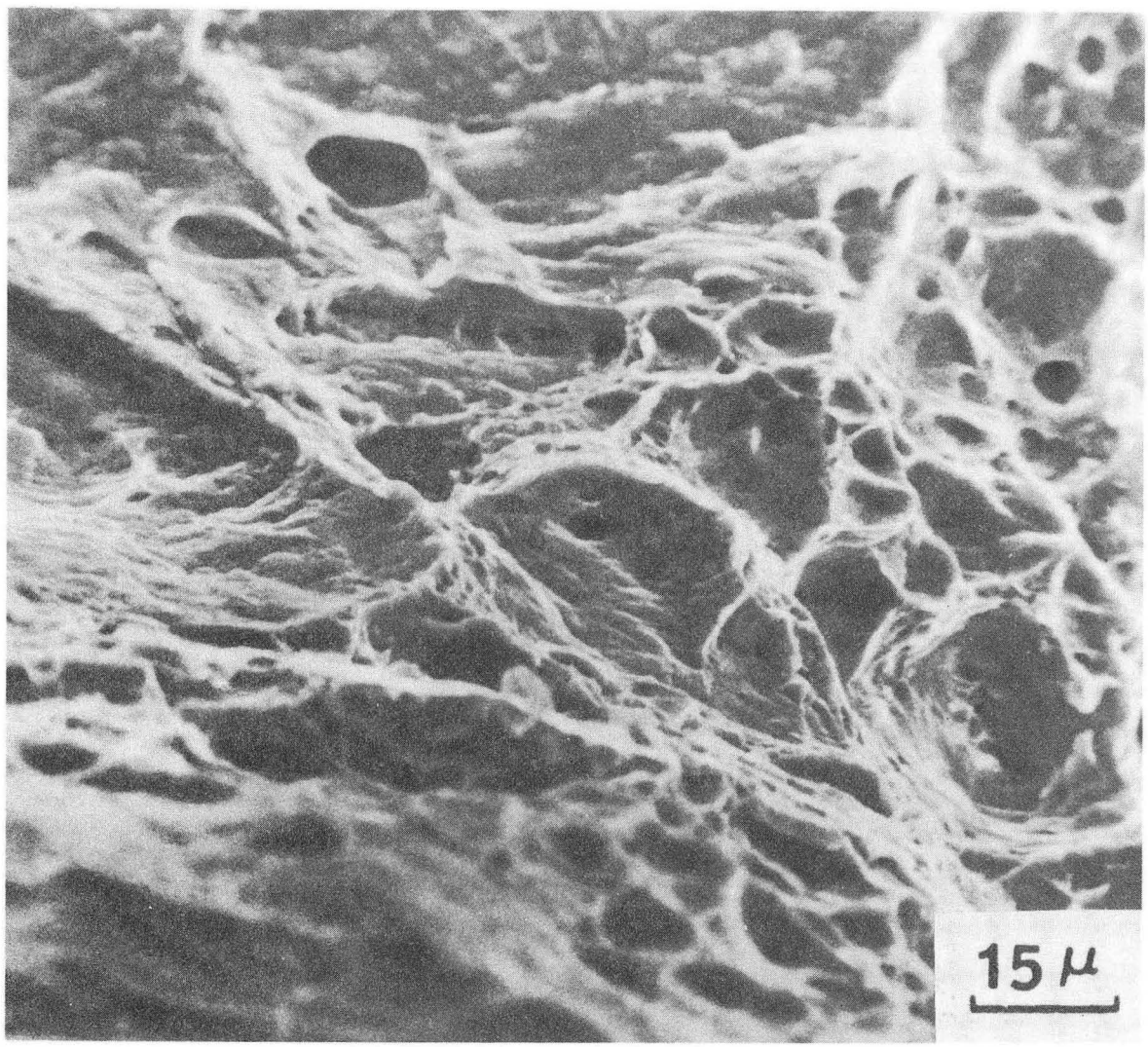

XBB 721-373

Fig. 45 Scanning fractograph of steel TC quenched and tempered at 200°C showing regions of dimpled rupture.

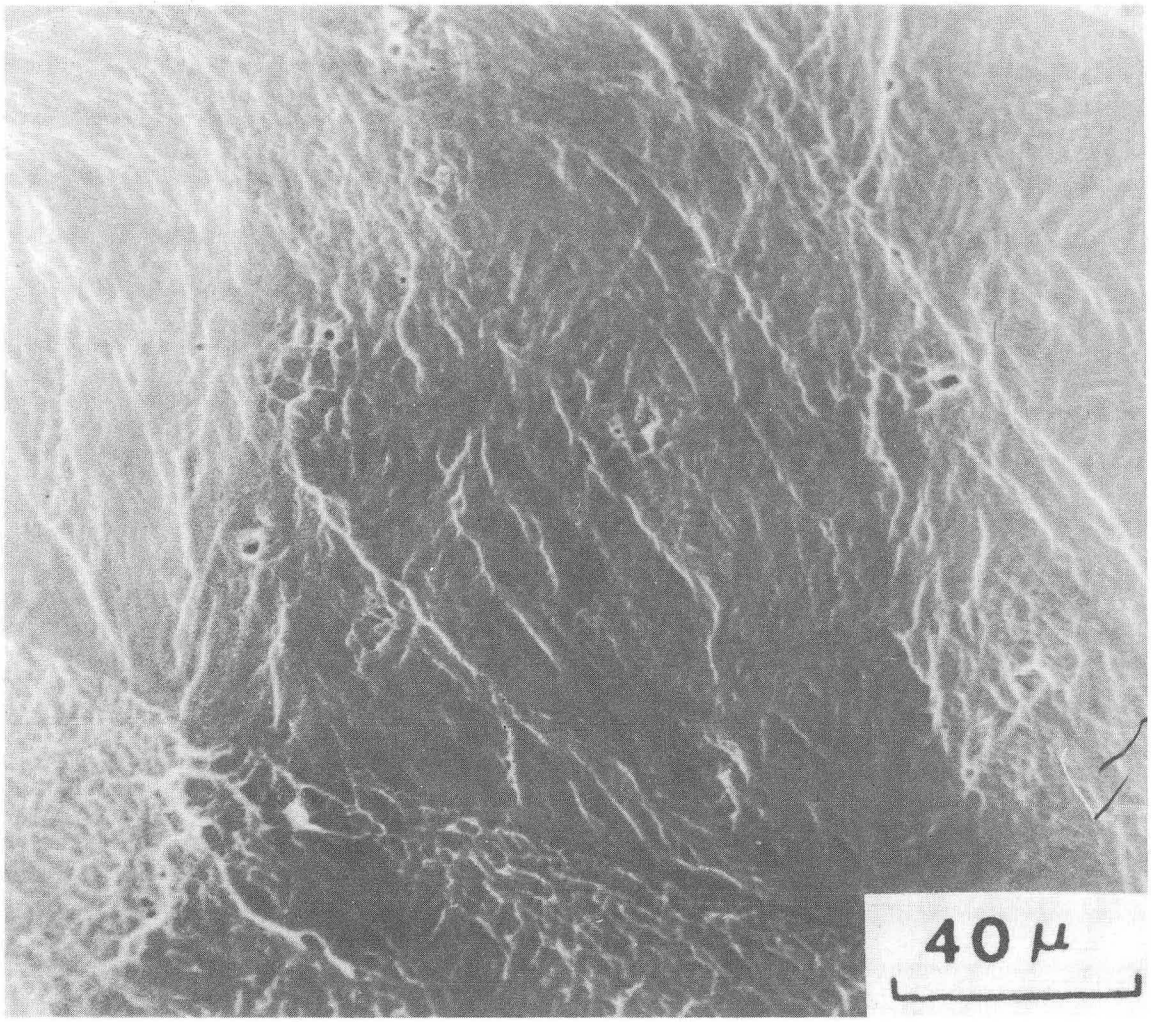

XBB 721-371

Fig. 46 Scanning fractograph of steel TC quenched and tempered at 300° showing extensive quasi-cleavage rupture.

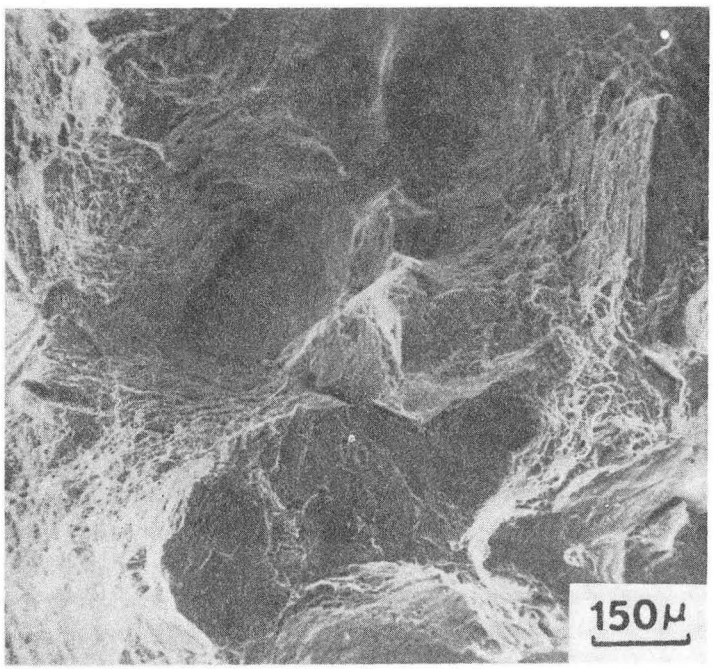

(A)

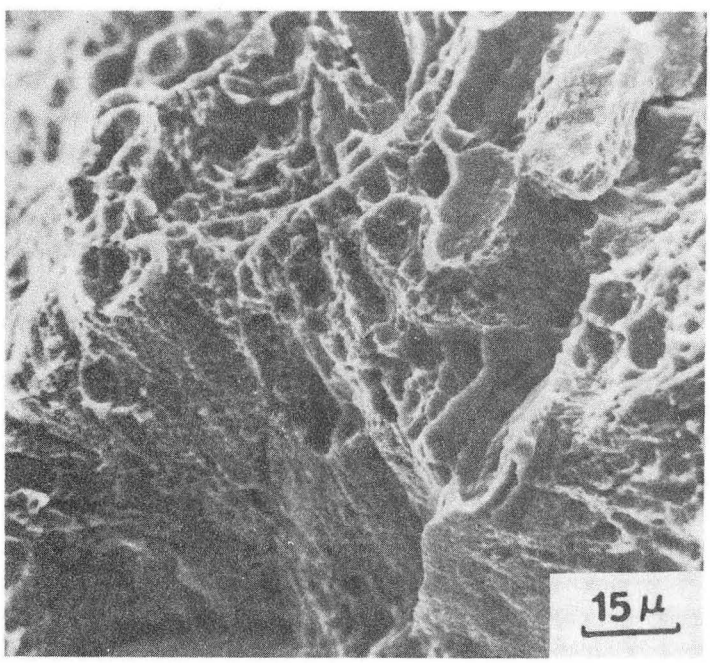

(B) XBB 721-387

Fig. 47 Scanning fractographs of steel TC, quenched and tempered at 400°C showing extensive dimpled rupture in (A) and in (B) an enlarged view of the dimples.

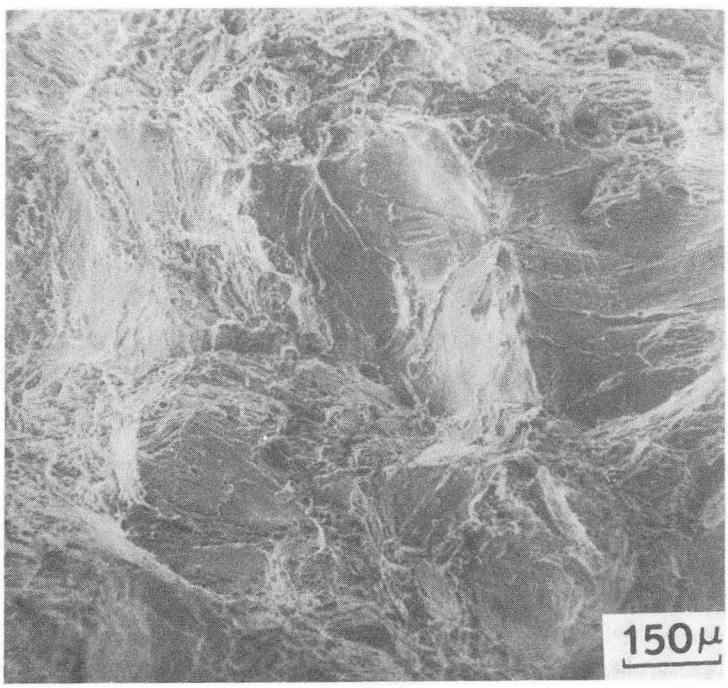

(A)

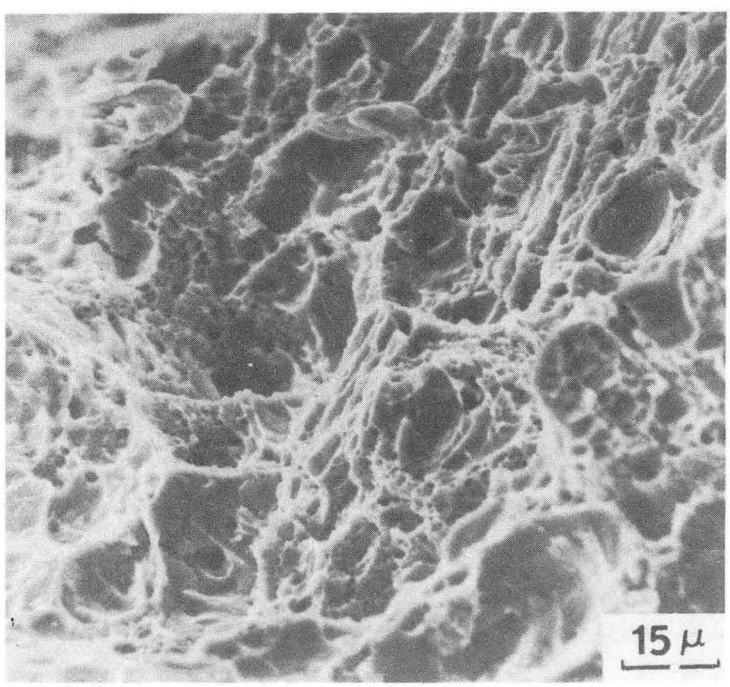

(B) XBB 721-383

Fig. 48 Scanning fractographs of steel TC quenched and tempered at 500°C showing (A) dimpled rupture and (B) a magnified view of the dimples.

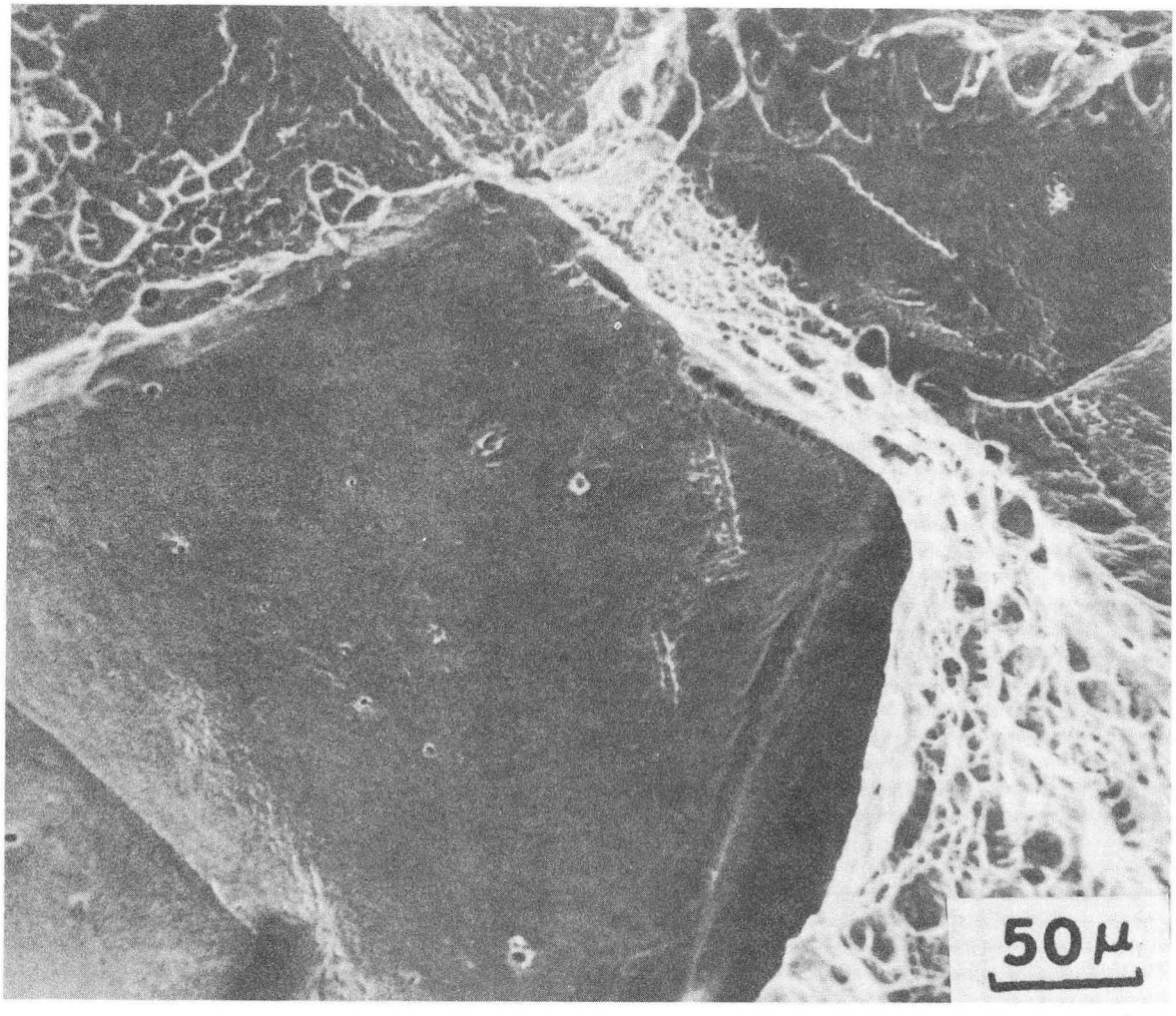

XBB721-374

Fig. 49 Scanning fractographs of steel UC as-quenched showing grain-boundary separation, cleavage and dimpled rupture.

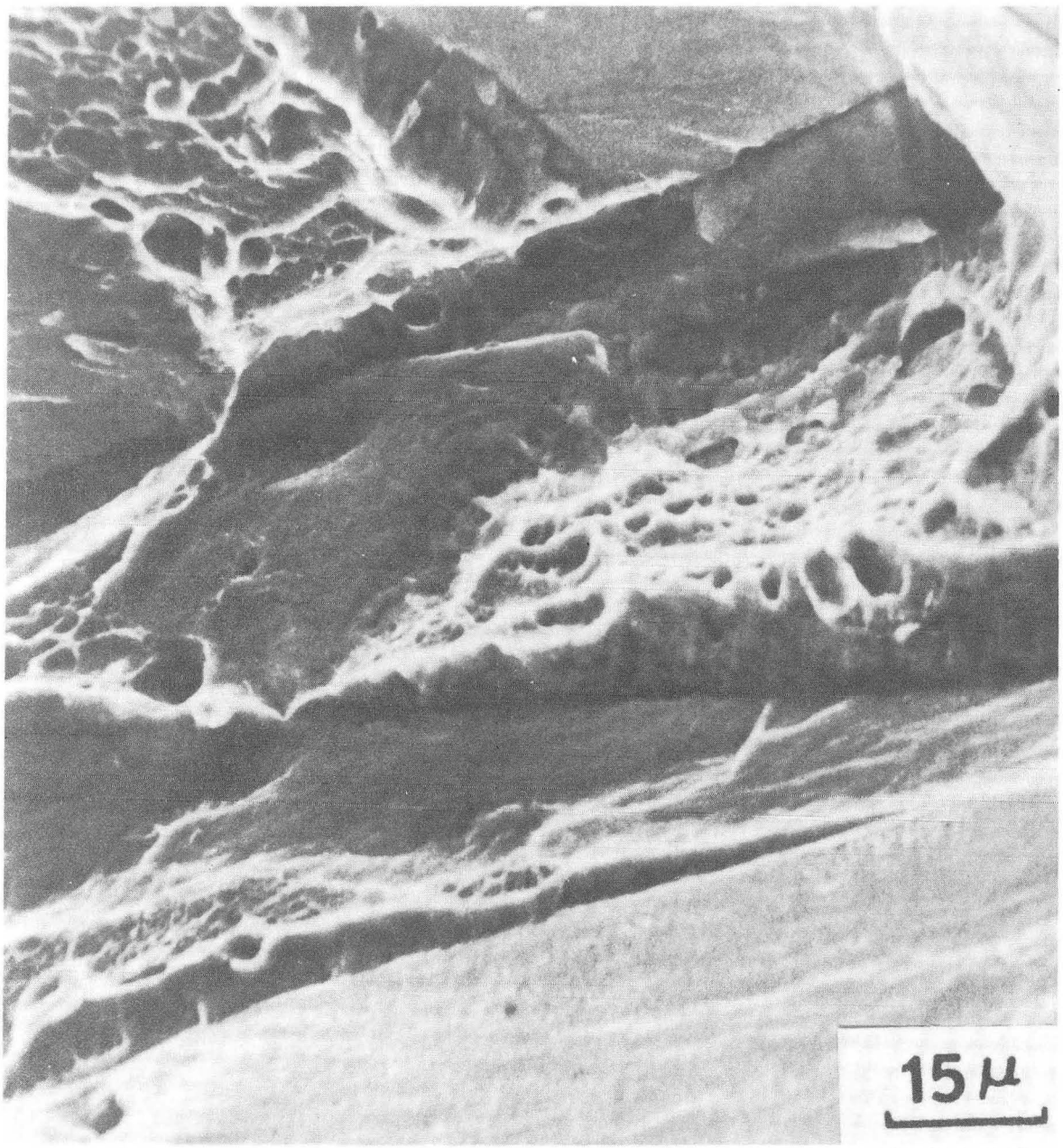

XBB721-378

Fig. 50. Scanning fractograph of fracture specimen of steel UC, quenched and tempered at 100°C showing regions of dimpled rupture and quasi-cleavage.

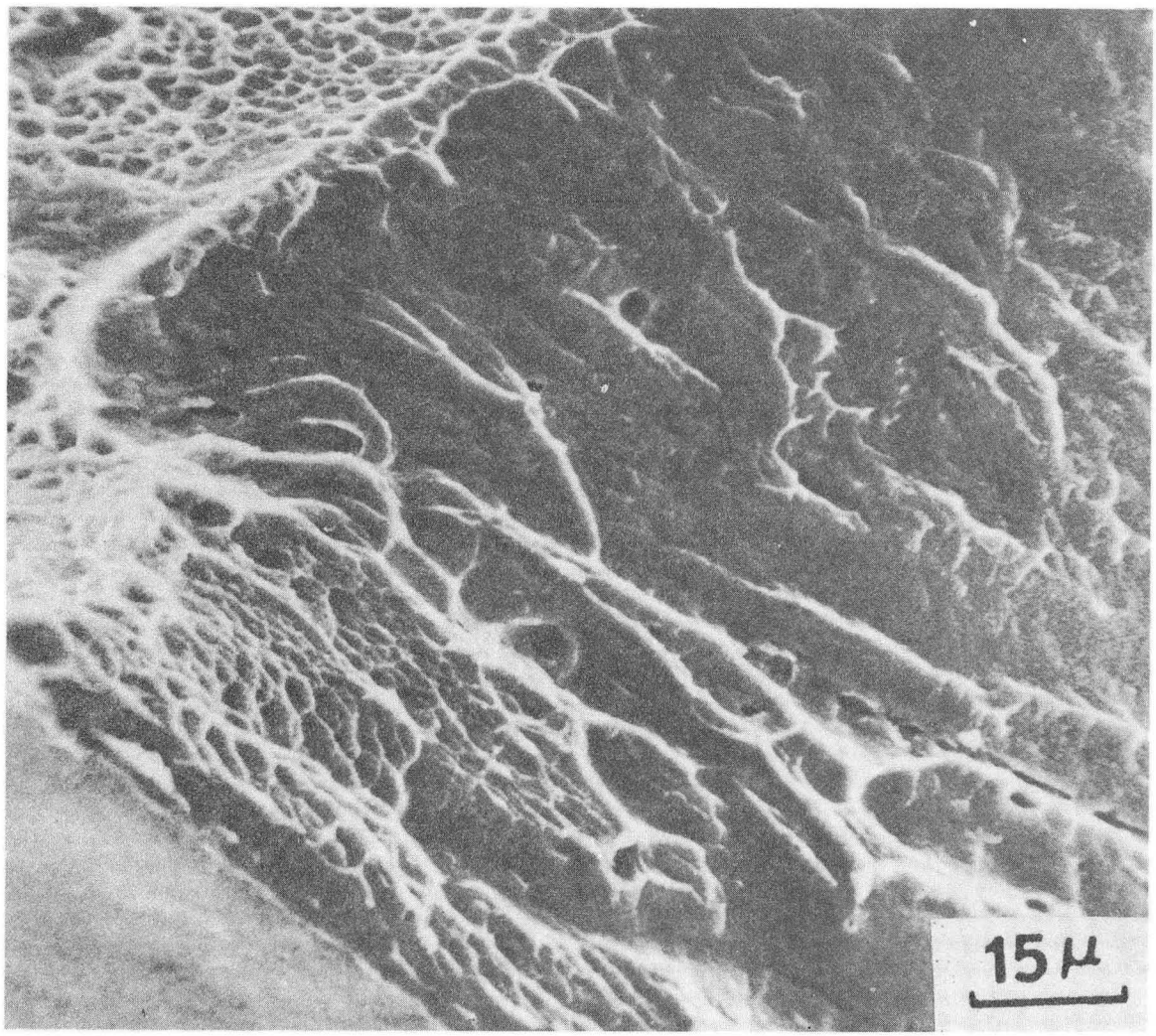

XBB 721-377

Fig. 51 Fracture morphology of steel UC, quenched and tempered at 200°C showing a mixture of quasi-cleavage and dimpled rupture.

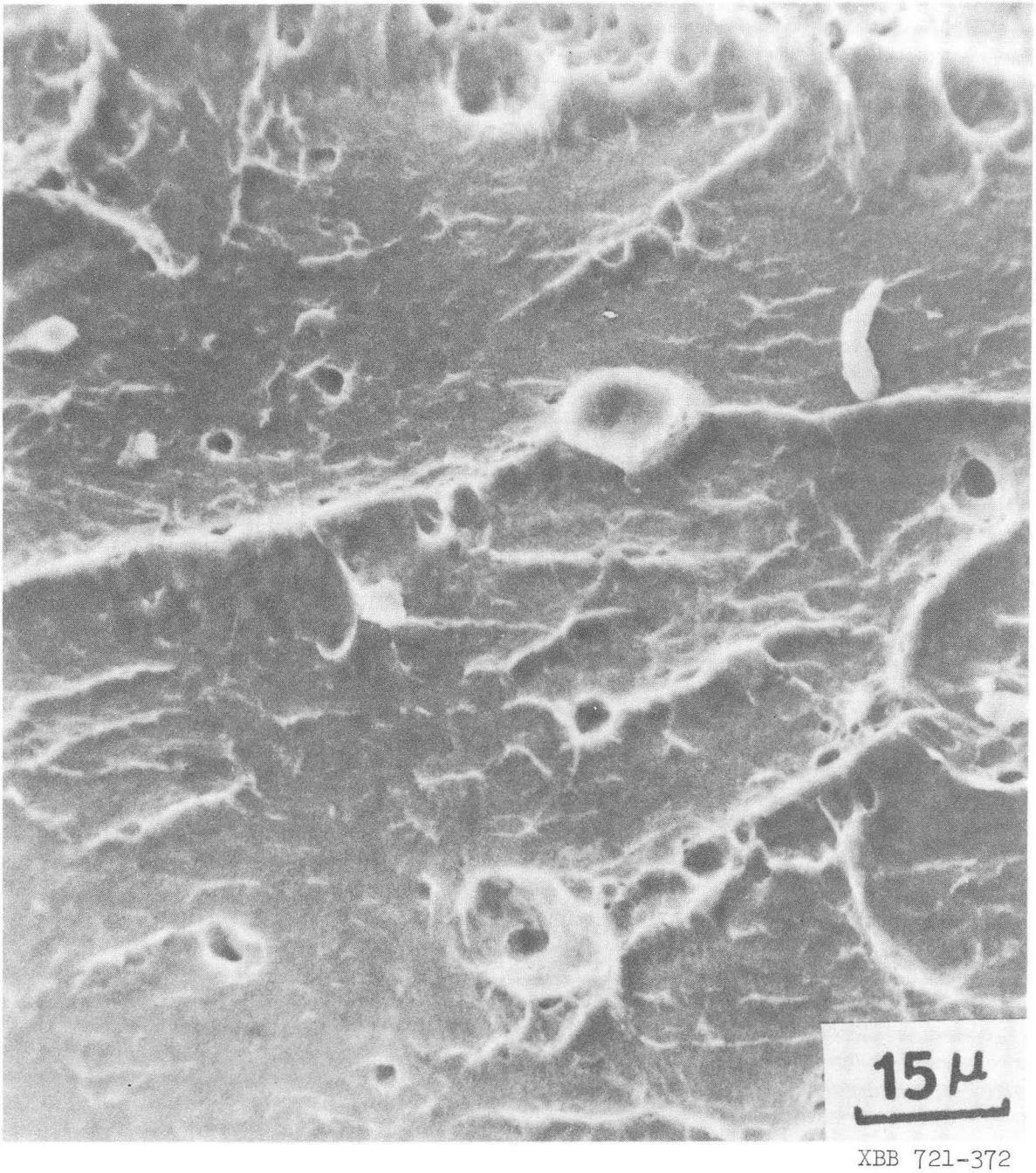

XBB 721-372

Fig. 52 Scanning fractograph of steel UC quenched and tempered at 300°C showing quasi-cleavage failure.

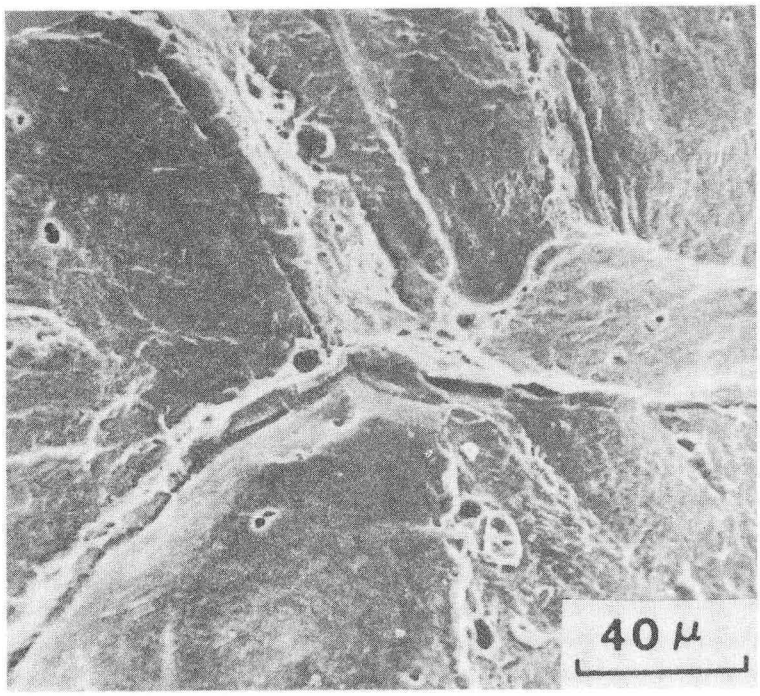

(A)

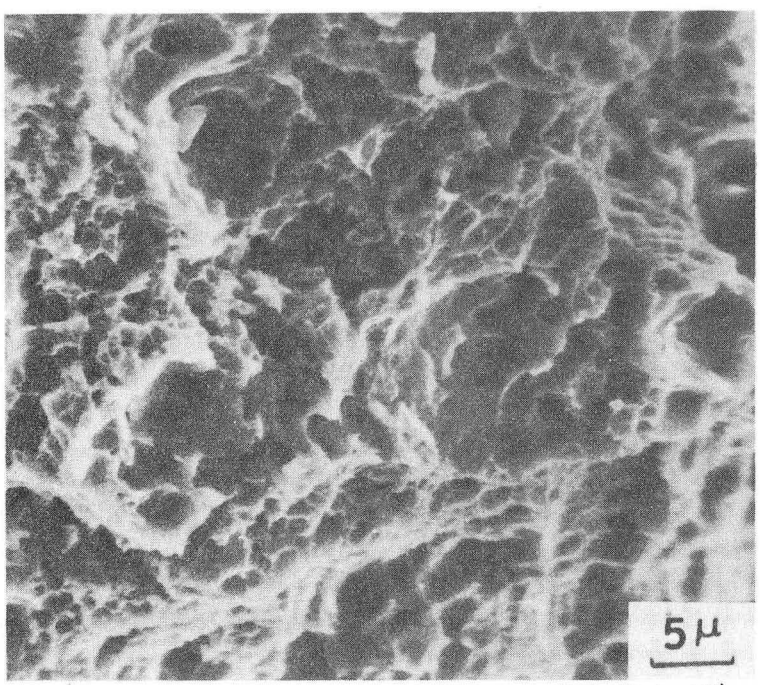

XBB 721-384

(B)

Fig. 53. Scanning fractograph of the fracture specimen of steel UC, quenched and tempered at 400°C showing (A) quasi-cleavage and (B) dimpled rupture.

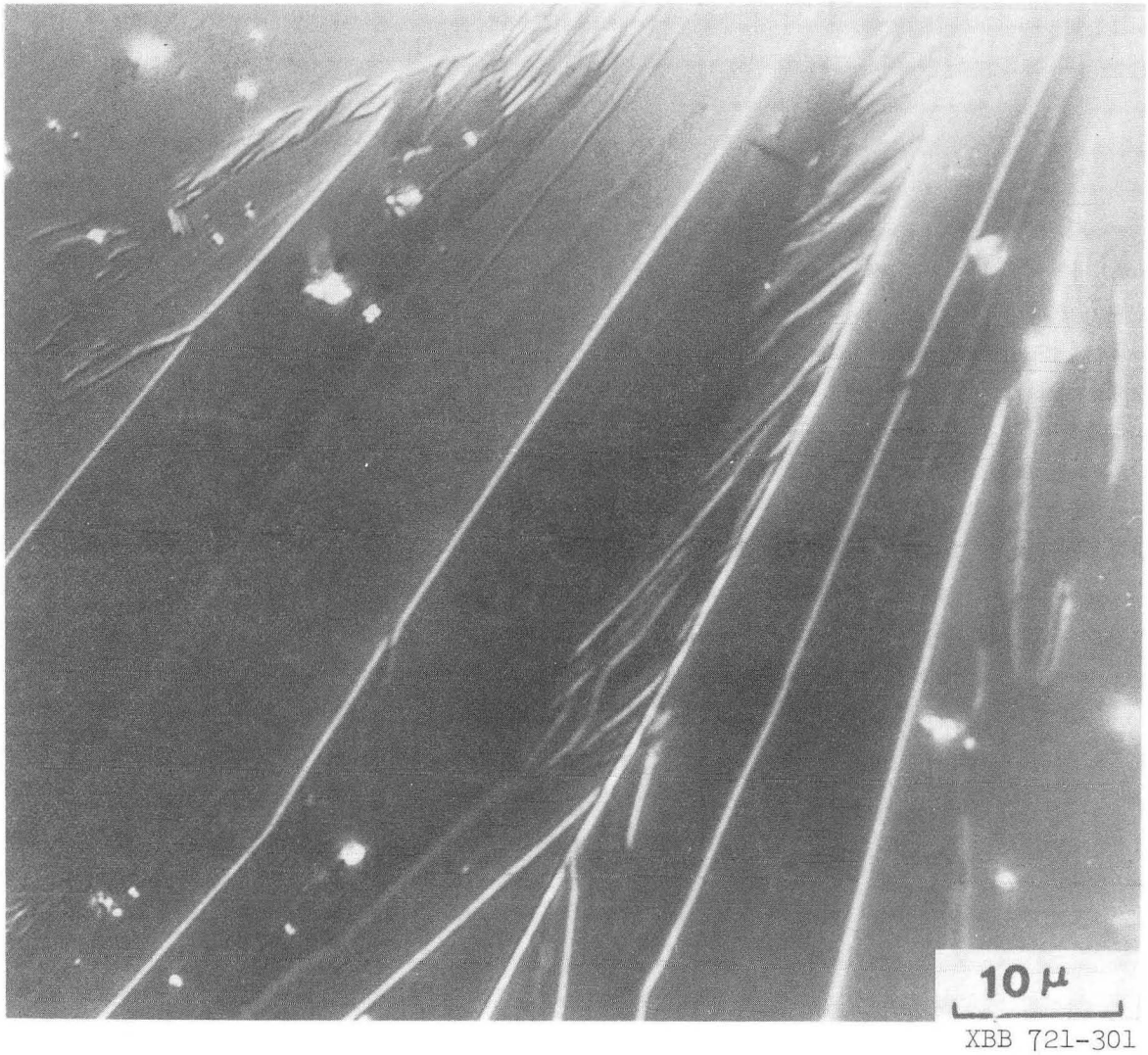

XBB 721-301

Fig. 54 Optical micrograph of alloy T in the as-quenched condition showing martensitic plates and mid-ribs under polarized light.

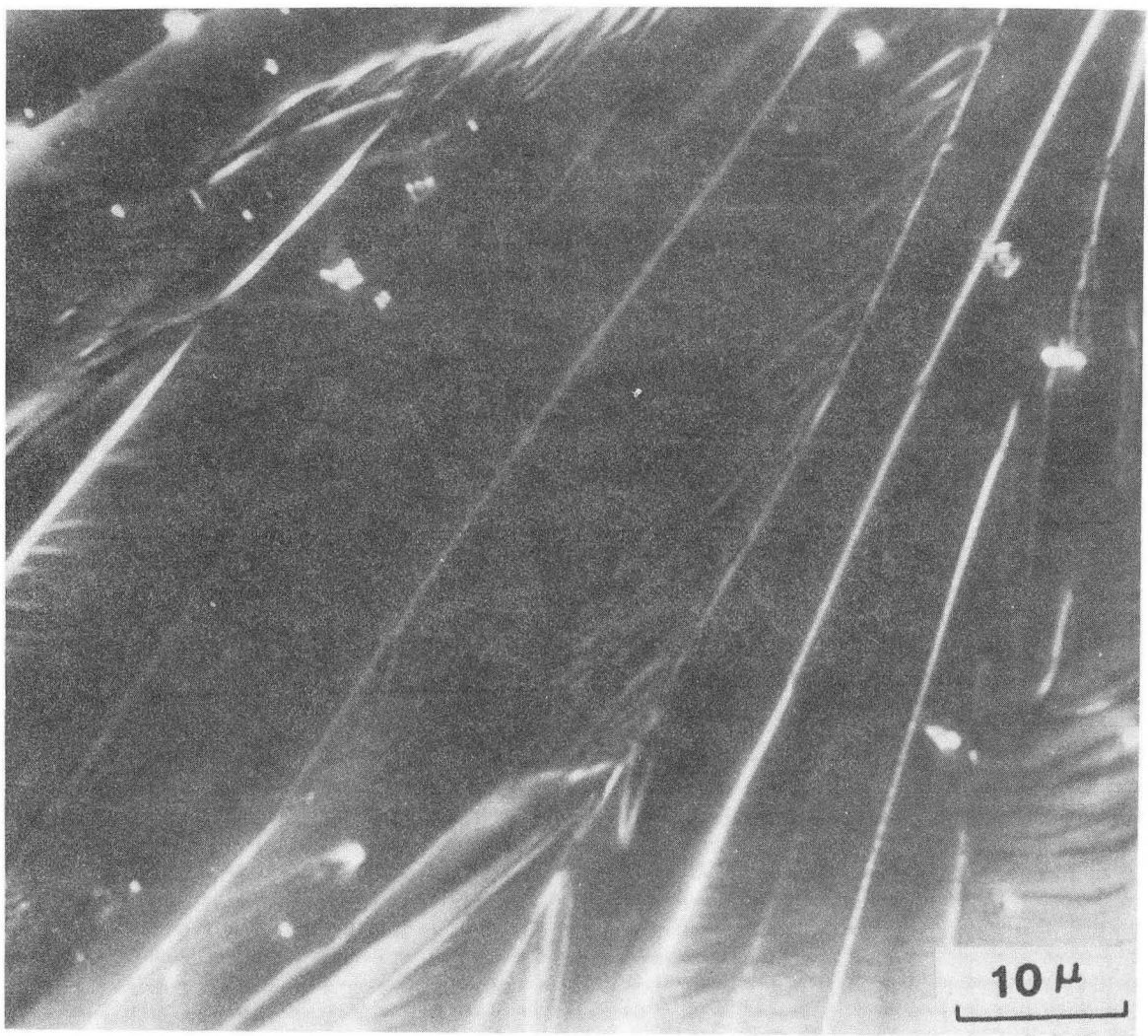

XBB 721-302

Fig. 55. Optical micrograph of steel T, quenched and deformed 5% in tension at -196°C. Note fine (slip) traces inside the martensitic plates. The micrograph was taken using a polarizer and an analyser to accentuate the contrast of the fine upheavals. (same area as Fig. 54)

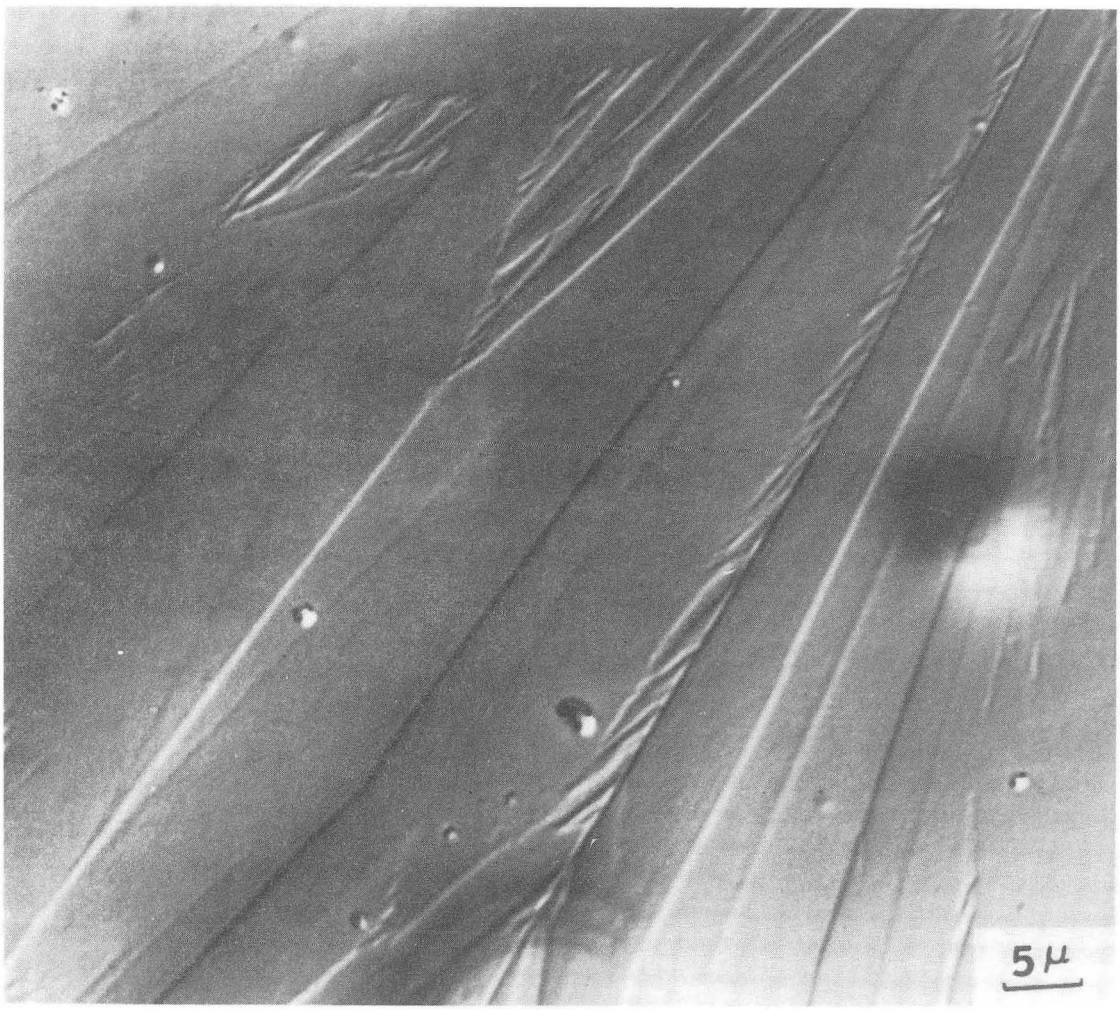

XBB 722-765

Fig. 56 Optical micrograph of steel T quenched, deformed 5% in tension at 196°C, and subsequently electropolished showing no traces. (same area as Fig. 54 and 55.)

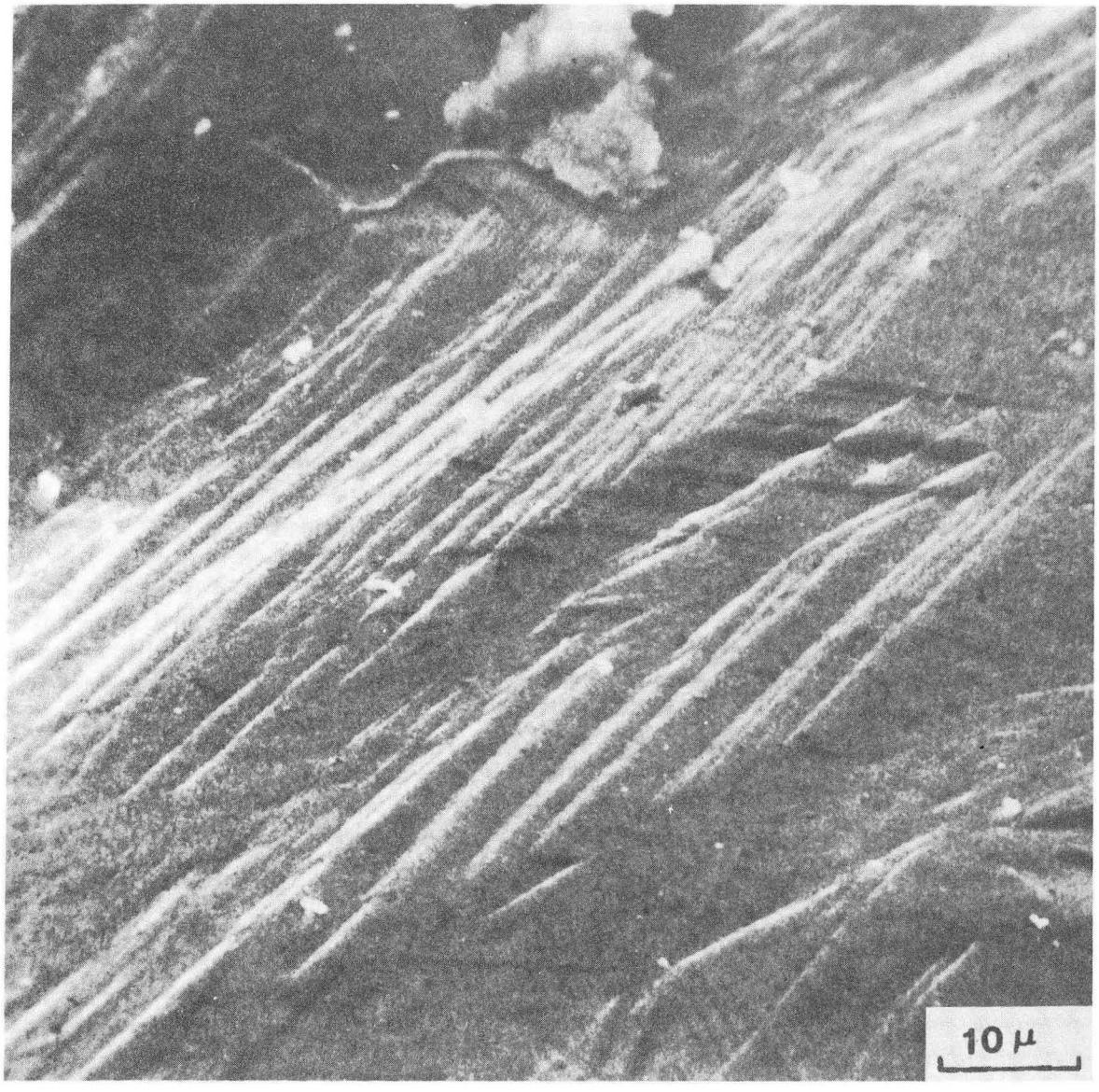

XBB 721-305

Fig. 57 Scanning micrograph of steel T quenched and deformed 5% in tension at -196°C showing traces. The wavy nature of the traces confirm that these traces are slip traces.

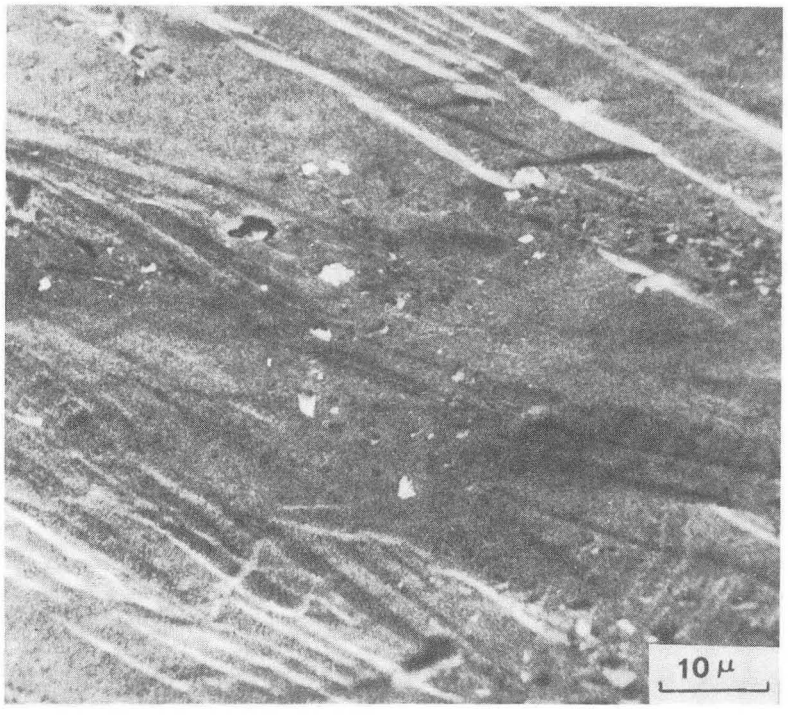

(A)

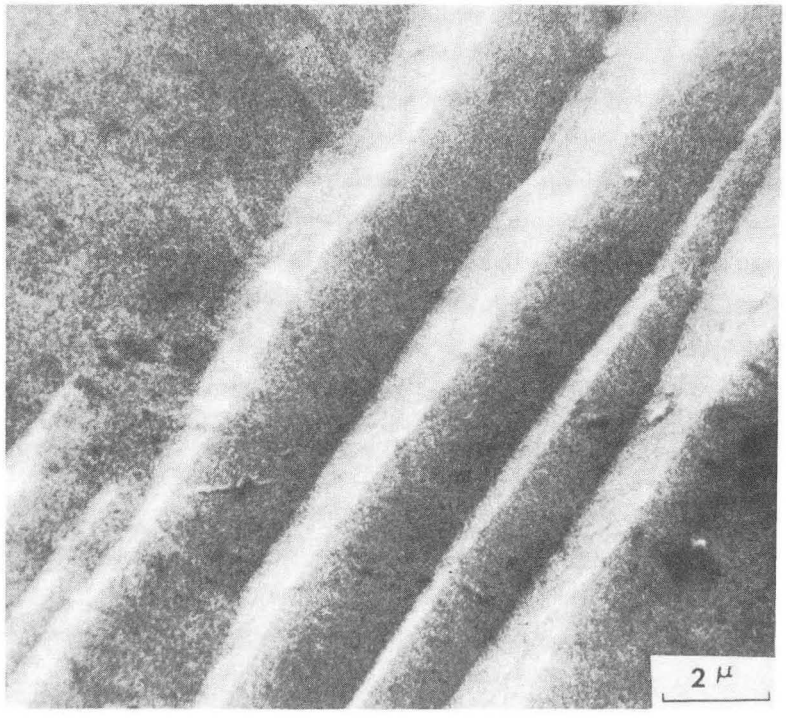

(B) XBB 721-299

Fig. 58 Scanning micrographs, of steel T, quenched and deformed 5% in tension at -196°C showing slip traces in (A) and (B) shows a magnified view of the slip traces.

TECHNICAL INFORMATION DIVISION
LAWRENCE BERKELEY LABORATORY
UNIVERSITY OF CALIFORNIA
BERKELEY, CALIFORNIA 94720